UNIVERSIDADE ESTADUAL DE CAMPINAS

FACULDADE DE ENGENHARIA MECÂNICA

DEPARTAMENTO DE MECÂNICA COMPUTACIONAL

TESE DE DOUTORADO

Ramiro Jose Chamorro Coneo

FSW process monitoring employing the spectrogram of the spindle forces and torque signal for AA-5052-H32 alloy

Monitoramento do processo FSW empregando espectrogramas para os sinais das forças e do torque da ferramenta para a liga AA-5052-H32

CAMPINAS
2017

Ramiro Jose Chamorro Coneo

FSW process monitoring employing the spectrogram of the spindle forces and torque signal for AA-5052-H32 alloy

Monitoramento do processo FSW empregando espectrogramas para os sinais das forças e do torque da ferramenta para a liga AA-5052-H32

Tese de Doutorado apresentada à Faculdade de Engenharia Mecânica da Universidade Estadual de Campinas como parte dos requisitos exigidos para obtenção do título de Doutor em Engenharia Mecânica, na Área de Mecânica dos Sólidos e Projeto Mecânico.

Orientador: Prof. Dr. Alberto Luiz Serpa
Coorientador: Prof. Dr. Antonio Jose Ramirez

ESTE EXEMPLAR CORRESPONDE À VERSÃO FINAL DA TESE DEFENDIDA PELO ALUNO Ramiro Jose Chamorro Coneo, E ORIENTADO PELO PROF. DR. Alberto Luiz Serpa.

.....
ASSINATURA DO ORIENTADOR

CAMPINAS
2017

Agência(s) de fomento e nº(s) de processo(s): Não se aplica.

Ficha catalográfica
Universidade Estadual de Campinas
Biblioteca da Área de Engenharia e Arquitetura
Luciana Pietrosanto Milla - CRB 8/8129

Chamorro Coneo, Ramiro Jose, 1983-
C357f FSW process monitoring employing the spectrogram of the spindle forces and torque signal for AA5052-H32 alloy / Ramiro Jose Chamorro Coneo. – Campinas, SP : [s.n.], 2017.

Orientador: Alberto Luiz Serpa.
Coorientador: Antonio Ramirez.
Tese (doutorado) – Universidade Estadual de Campinas, Faculdade de Engenharia Mecânica.

1. Soldagem. 2. Fourier, Transformada de. 3. Análise espectral. 4. Lógica fuzzy. 5. Soldadura por fricção. I. Serpa, Alberto Luiz, 1967-. II. Ramirez, Antonio. III. Universidade Estadual de Campinas. Faculdade de Engenharia Mecânica. IV. Título.

Informações para Biblioteca Digital

Título em outro idioma: Monitoramento do processo FSW empregando espectrogramas para os sinais das forças e do torque da ferramenta para a liga AA5052-H32
Palavras-chave em inglês:
Welding
Fourier transform
Spectral analysis
Fuzzy logic
Friction welding
Área de concentração: Mecânica dos Sólidos e Projeto Mecânico
Titulação: Doutor em Engenharia Mecânica
Banca examinadora:
Alberto Luiz Serpa [Orientador]
Alex Matos da Silva Costa
Auteliano Antunes dos Santos Junior
Guilmar Ferreira Batalha
Janito Vaqueiro Ferreira
Data de defesa: 29-11-2017
Programa de Pós-Graduação: Engenharia Mecânica

UNIVERSIDADE ESTADUAL DE CAMPINAS

FACULDADE DE ENGENHARIA MECÂNICA

COMISSÃO DE PÓS-GRADUAÇÃO EM ENGENHARIA MECÂNICA

DEPARTAMENTO DE MECÂNICA COMPUTACIONAL

TESE DE DOUTORADO

FSW process monitoring employing the spectrogram of the spindle forces and torque signal for AA-5052-H32 alloy

Monitoramento do processo FSW empregando espectrogramas para os sinais das forças e do torque da ferramenta para a liga AA-5052-H32

Autor: Ramiro Jose Chamorro Coneo
Orientador: Prof. Dr. Alberto Luiz Serpa
Coorientador: Prof. Dr. Antonio Jose Ramirez

A Banca Examinadora composta pelos membros abaixo aprovou esta Tese:

Prof. Dr. Alberto Luiz Serpa
DMC/FEM/UNICAMP

Prof. Dr. Alex Matos da Silva Costa
CPM/LNNANO/CNPEM

Prof. Dr. Auteliano Antunes dos Santos Junior
FEM/UNICAMP

Prof. Dr. Gilmar Ferreira Batalha
Escola Politécnica, USP

Prof. Dr. Janito Vaqueiro Ferreira
DMC/FEM/UNICAMP

A Ata da defesa com as respectivas assinaturas dos membros encontra-se no processo de vida acadêmica do aluno.

Campinas, 29 de novembro de 2017.

Dedicatória

A mi esposa, Suranny Jimenez Chacon, a mis padres Fredy Ramiro Chamorro Niebles y Damiana Judith Coneo Nuñez, a mis hermanos, Ana Maria Chamorro Coneo y Manuel Maria Chamorro Coneo, y a toda mi familia por su amor, suporte y apoyo incondicional.

Agradecimentos

A minha esposa Suranny e minha familia meus pais Fredy e Damiana, meus irmãos Ana e Manuel, e meu tio Wilmar por seu carinho, confiança e apoio fornecido.

Ao COLCIENCIAS - “Programa Nacional de Becas de Doctorado en el Exterior” do Departamento de Ciencias de Colômbia pelo apoio financeiro durante o desenvolvimento deste trabalho.

A meu orientador, Prof. Dr. Alberto Luiz Serpa, pela instrução e apoio durante o desenvolvimento deste trabalho.

Aos meus companheiros de trabalho e amigos da FEM, pela ajuda e discussões durante o desenvolvimento deste trabalho.

A toda equipe do CNPEM-LNNANO, Victor, Eduardo, Mateus, Joel e Julian pelo apoio durante esta a pesquisa.

À Faculdade de Engenharia Mecânica da UNICAMP, representada pelos professores e funcionários, que me concedeu a oportunidade de realizar este trabalho.

Resumo

CHAMORRO CONEO, Ramiro Jose. Monitoramento do processo FSW empregando espectrogramas para os sinais das forças e do torque da ferramenta para a liga AA-5052-H32. 2017. 148p. Tese (Doutorado). Faculdade de Engenharia Mecânica, Universidade Estadual de Campinas, Campinas.

Este trabalho procura identificar imperfeções durante um processo de soldagem por fricção (FSW) usando o espectrograma da Transformada de Fourier de Curto Tempo (STFT) dos sinais da forças da ferramenta e do torque da ferramenta. Esta técnica foi considerada também uma fonte de informação sobre a estabilidade da soldagem durante o processo, especialmente levando em consideração as forças transversais e laterais. Considerando a importância das forças da ferramenta e do torque da ferramenta, um experimento foi executado usando duas chapas AA5052-H32 de ligas alumínio em uma soldagem de topo. O experimento considerou a variação dos três parâmetros operacionais: velocidade de rotação, velocidade transversal e profundidade de penetração. As respostas foram analisadas utilizando os espectrogramas dos sinais e uma análise estatística que mostra os parâmetros operacionais de influência sobre as ocorrências de falhas usando a técnica STFT. O espectrograma foi capaz de reconhecer o instante em que as falhas ocorreram em uma janela de 2 segundos a 100 Hz da taxa de amostragem. Os resultados mostram que não só as forças laterais e transversais possuem informações relevantes no espectro, mas também a força axial e o torque podem contribuir para o reconhecimento de imperfeções. No entanto, analisando o espectro de um único sinal, as falhas podem não ser detectadas. Usando os padrão dos espectogramas, um sistema de lógica difusa foi projetado para indicar a maior probabilidade de falha.

Palavras-chave: Soldagem por Atrito, Transformada de Fourier de Tempo Curto, Espectrograma, Lógica Difusa, Imperfeições.

Abstract

CHAMORRO CONEO, Ramiro Jose. FSW process monitoring employing the spectrogram of the spindle forces and torque signal for AA-5052-H32 alloy. 2017. 128p. Thesis (Doctor in Engineering). School of Mechanical Engineering, University of Campinas - UNICAMP, Campinas, São Paulo, Brazil.

This research aims to detect voids and cavities defects during a friction stir welding process using the Short Time Fourier Transform (STFT) spectrogram of the tool forces and the spindle torque signals. This technique was considered also a source of information on the welding stability during the process, especially taking into account the traverse and lateral forces. Considering the importance of the tool forces and the spindle torque during the process, an experiment was run by welding two aluminum AA5052-H32 plates nearly in parallel position and not overlapped (butt welding). The experiment considered the variation of the three operational parameters: rotation speed, traverse speed, and penetration depth. The responses were analyzed using the spectrograms of the signals and a statistical analysis showing the influence of the operational parameters over the fault occurrences using the STFT. The spectrogram was able to recognize the instant when the discontinuities occurred in a window of 2 seconds at 100 Hz of the sample rate. The results show that not only the lateral and traverse forces have relevant information in the spectrum, but also the axial force and the spindle torque can contribute for the recognition of imperfections. However, analyzing the spectrum of one single signal, faults may be undetected. A fuzzy logic system was designed to show the major fault probability using the spectogram pattern.

Keywords: Friction Stir Welding, Short Time Fourier Transform, Spectrogram, Fuzzy logic, Voids, Cavities.

List of Tables

List of Figures

List of symbols, Abbreviations, and Acronym

As abreviaturas e siglas usada neste trabalho são:

- t: Time (also indicates time domain)
- f: Frequency (also indicates frequency domain)
- k: Sample point time
- $x(t)$: Input function signal
- $x[k]$: Discrete input signal;
- $X(f)$: Fourier Transform;
- j: Imaginary unit $j = \sqrt{-1}$;
- $h[k]$: Window function;
- l: Discrete delay time;
- τ: Delay time;
- N: Size of sample (also training data);
- Δf: Frequency resolution;
- f_s: Sample frequency;
- L: Window size;
- φ: Activation function;
- w_i: Synaptic weights;
- b: Bias;
- y: Process output;
- $\widehat{y}$: Output model;
- $\varepsilon(\mathbf{W})$: Mean square error;

- $\mathbf{X}$: Input vector;
- $\mathbf{W}$: Synaptic vector;
- $\mathbf{W}^*$: Optimal synaptic vector;
- $\mathbf{g_k}$: Gradient vector;
- n: Iteration number;
- $\mathbf{I}$: Identity Matrix;
- η: Learning rate;
- $\mathbf{J_n}$: Jacobian Matrix;
- $\mathbf{H_n}$: Hessian Matrix;
- $\mathbf{e_n}$: Error vector between process output and model output;
- λ: Regularization factor;
- α: Regularization factor (Bayesian regularization);
- β: Regularization factor (Bayesian regularization);
- γ: Effective number of parameters;
- M: Total number of weights;
- E_W: Sum of square of the weights;
- E_D: Error sum square;
- F: Nonlinear function;
- dl: Number of backward time-shifts;
- $\mu(x)$: Membership function;
- a, b, c, d: Geometric parameters of the membership functions;
- σ: Width of gauss membership function;
- F_x: Traversing force;

- F_y: Side force;
- F_z: Down force;
- ω: Tool rotating speed;
- ν: Traversing speed;
- d_p: Depth penetration;
- ANN: Artificial Neural Network;
- DAQ: Data acquisition system;
- FSW: Friction Stir Welding;
- NARX: Non-linear Autoregressive with External Input;
- STFT: Shot-time Fourier Transform;
- MF: Membership Function;
- ANOVA: Analysis of Variance;
- PLC: Programmable Logic Controller;

TABLE OF CONTENTS

1 Introduction

1.1 Motivation

The Friction Stir Welding (FSW) process is one of the most promising joining techniques of materials because of its high efficiency and the excellent mechanical properties of the resulting joint. Since its invention in the 90's (THOMAS ET AL.; THOMAS ET AL., 1995; 1999), this technology has been widely used in innumerable applications such as the shipbuilding industry, the aerospace industry and recently the automotive manufacturing sector (KALLEE ET AL., 2002).

This joining process is performed in a solid-state condition without liquid phase. The joining process is accomplished using a tool that has a shoulder and a probe, whose geometry varies depending on the workpiece material (RAI ET AL., 2011).

During the FSW process, lower temperatures are generated when compared to conventional welding processes. This can be a great advantage because avoids the generation of the undesirable phase transformation and the absence of deformation due to solidification. In addition, the severe process of plastic deformation produces a finer grain structure, which improves the mechanical properties of the joint (MISHRA AND MA, 2005).

The control of the process is one of the challenges in the FSW process. Normally, the FSW machine parameters control involves the tool rotation speed, the traversing speed, the penetration depth, the tool forces (the down force, traversing force, and side force), the spindle torque and the tool temperature, which constitute the welding parameters. However, the control of these parameters may be a challenge and can not assure a good joint. If the process uses the wrong parameters, the joint will have defects, most of them produced by the fluctuations during the process.

One aspect that is strongly related to imperfection formation is the flow of material around the tool during the process (NANDAN ET AL., 2008). The flow of material is related to the welding parameters of the process and it is difficult to measure (NANDAN ET AL., 2008). Usually, the welding parameters are configured empirically in the machine by trials and errors, and it is uncertain whether the joint has or not some imperfection. Thus, the FSW joint needs to be inspected, increasing the cost of the process. On the other hand, some operational parameters interact during the process, including the material flow around the FSW tool, changing the mechanical properties of the welded material (GIBSON ET AL., 2014), what makes this a dynamic nonlinear process, which is difficult to model.

As mentioned earlier, the material flow is an important parameter to be considered for

the defect formation in the welding. In recent research (BOLDSAIKHAN ET AL., 2011a), the authors related the material flow to the tool's forces, especially with the traverse force. This research suggests that there is an oscillatory response of the forces because of the transport of material from the advancing side to the retreating side produced by the tool. As a result, if there is a good weld, the forces will have a harmonic oscillation response. On the other hand, a bad weld implies a bad transport of material and this will show a different pattern of oscillation of the forces.

Taking into account this information, the frequency spectrum analyses of the forces (BOLDSAIKHAN ET AL., 2011b) as a way to determinate whether it was a good processing or not can be implemented. The frequency spectrum pattern can be identified using the Fast Fourier Transform (FFT). In both analyses the authors concluded that the low-frequency components of the frequency spectrum of forces increase when a discontinuity occurs, indicating an imperfection in the weld.

However, the models do not relate directly the input parameters to the response of these forces or to the frequency spectrum. These models have only the monitoring function for a possible post-processing of the workpiece.

In addition, the FSW models are in the vast majority focused on the steady state of the process and frequently involves finite elements or finite difference methods (ZAEH AND GEBHARD, 2010). This kind of numeric solution requires computational time and sophisticated equipment, especially when the model explores the dynamic effects.

Nevertheless, there are some researches have tried the nonlinear dynamic modeling involving the dynamic response of the FSW process, making the model more complex. The dynamic behavior of the down force was modeled in (XIN ET AL., 2007) and (OAKES AND LANDERS, 2009). The nonlinear relation between the inputs (tool rotation speed, traversing speed and penetration depth) and the down force was established experimentally on these researches for aluminum 6061-T6 and 6061-T4 plates. A steady-state logarithmic model was also developed, allowing the nonlinear model identification using the recursive least square method.

Davis et al. (2011) modeled the nonlinear dynamic behavior of the down force for FSW process in the AA7075 alloy. They used an experimental logarithmic model for the force in steady state condition and then a second order dynamic model was adjusted with a recursive least square method.

In general, the models are mainly focused only on the stable part of the welding process and not on the entrance of the tool at the beginning of the welding process. These dynamic models were used to design a nonlinear controller to control the axial force in the tool. Com-

mercially, the FSW process can be controlled through the position and force of the tool. Recently, the spindle torque control and the temperature in the joint control revealed good results (ROSS AND SORENSEN; ROSS AND SORENSEN, 2016a; 2016b).

FSW process control is really a difficult task. Even with the welding machine instrumented, the control variables are mainly focused on the welding machine structural integrity. This means that even when a control technique is present in the FSW machine by using the welding machine position control, force control or torque control, the process still remains manual because the operator has to verify the state of the process in order to preserve a good quality of the welding (NELSON ET AL., 2016).

Some authors (SILVA ET AL.; BACHMANN AND ZAEH, 2016; 2016) suggest that the temperature between the tool and the workpiece is the key parameter to control. Nevertheless, the temperature is difficult to measure or to estimate. In addition, the control of the temperature must be specified for the joint. The use of the tool forces maybe a better control variable, due to the relation with the formation of defects during the welding process.

In this thesis, a fuzzy logic monitoring system of the tool forces and spindle torque spectrum variation (the forces and torque frequency analysis) in a FSW process for aluminum 5052-H32, incorporating the detection of imperfection in the welding, was investigated. This model is evaluated in different process conditions including also the beginning of the welding process (plunge stage), using first an ANN dynamic model for time domain analysis and then using the Short-Time Fourier Transform (STFT) to analyze the frequency domain. During this thesis, the tool traversing force, that is already know as indicator of imperfection (BOLDSAIKHAN ET AL., 2011a) and other parameters like the down force (tool axial force) and the spindle torque, since they could add more information for an imperfection detection were analyzed.

1.2 Objectives

The general objective of this research is the determination of an imperfection pattern detection by using computational intelligent tools, such as fuzzy logic and artificial neural networks, for the FSW process for aluminum 5052-H32 plates.

The specific objectives of this research are:

- To identify imperfection patterns in the welding using the spectral analysis of the forces and torque signals during FSW of aluminum 5052-H32 plates.
- To develop an ANN model using experimental data of the down force, the torque and monitoring the tool temperature.

- To identify which welding parameter affects the most the generation of imperfections.
- To create a fuzzy logic based model using the spectrum that detects the imperfection occurrence.

1.3 Structure of this document

This document is organized as follows.

In Chapter 2, the main aspects of the Fast Fourier Transform, the Short-Time Fourier Transform (STFT), the artificial neural networks and fuzzy logic are presented.

In Chapter 3, the FSW process and the experimental setup used (welding machine, tool geometry, materials, etc.) are presented. The explanation on how to detect imperfection patterns using the traversing force and the Fast Fourier Transform (FFT) are also discussed.

In Chapter 4, the methodology followed during this research is described. It is also detailed the material, equipment, and operational parameters used during the experiments.

In Chapter 5, some of the results of the experiment are expressed, explaining the complexity of the identification of the FSW model. These specifications will be used for the Artificial Neural Network model. An analysis and validation of the response are conducted.

In Chapter 6, the conclusions and future research are presented.

2 Fast Fourier Transform, Artificial Neural Network, and Fuzzy Logic

For this thesis, some essentials about the Fast Fourier Transform (FFT), Artificial Neural Network (ANN), and Fuzzy logic should be pointed. The first is a faster version of the Discrete Fourier Transform (DFT), which is extremely important for spectrum analysis. These spectrum analyses will help to determine patterns of imperfections during the FSW process. The second is the artificial intelligent algorithms, which has a good performance in mapping and in pattern recognition. The third is generalization of the traditional logic and describes a knowledge-based system expressed in a linguistic form. This kind of system normally included nonlinear components and good behavior in uncertain systems. The basics aspects of these two vast topics will be discussed in this chapter.

2.1 Fourier Transform definitions

The Fourier transform, usually employed in signal processing, converts a time signal into its frequency representation, the so-called spectrum. Mathematically, the Continuous Fourier Transform is defined by

$$X(\omega) = \int_{-\infty}^{\infty} x(t) e^{-j\omega t} dt \tag{2.1}$$

where $X(f)$ is the Fourier transform of the function $x(t)$, t is time variable and f is the complex variable in the frequency domain (HSU, 1995). However, signals are normally acquired using discrete sampling which limits the use of the previous equation. Consequently, it is necessary to consider the Fourier Transform in a discrete form, i.e,

$$X(f) = \sum_{k=-\infty}^{\infty} x[k] e^{-j\omega k} \tag{2.2}$$

where k indicates the discrete time sample point of the signal, and $x[k]$ is the discrete signal (OPPENHEIM AND SCHAFER, 2010). This equation is applied for an infinity segment, but normally the segment analyzed has a finite data sample. The DFT for a finite set of data is

$$X(f) = \sum_{k=0}^{N-1} x[k] e^{-j\omega k} \tag{2.3}$$

where N is the size of the acquired signal. The resulting frequency components of the Fourier Transform represent a global analysis of the signal and are very useful when the frequency

components are not time variant. As a consequence, the Fourier Transform is not indicated for signals with time variation in the frequency components, like a disturbance signal or a fault signal. So it will not be possible to analyze a signal spectrum when a disturbance occurs without the time information. In some analyses, it is not even possible to say that there was some disturbance during this time using only the Fourier Transform. As an example, Figure 2.1 presents two different signals that will be analyzed using the Fourier Transform.

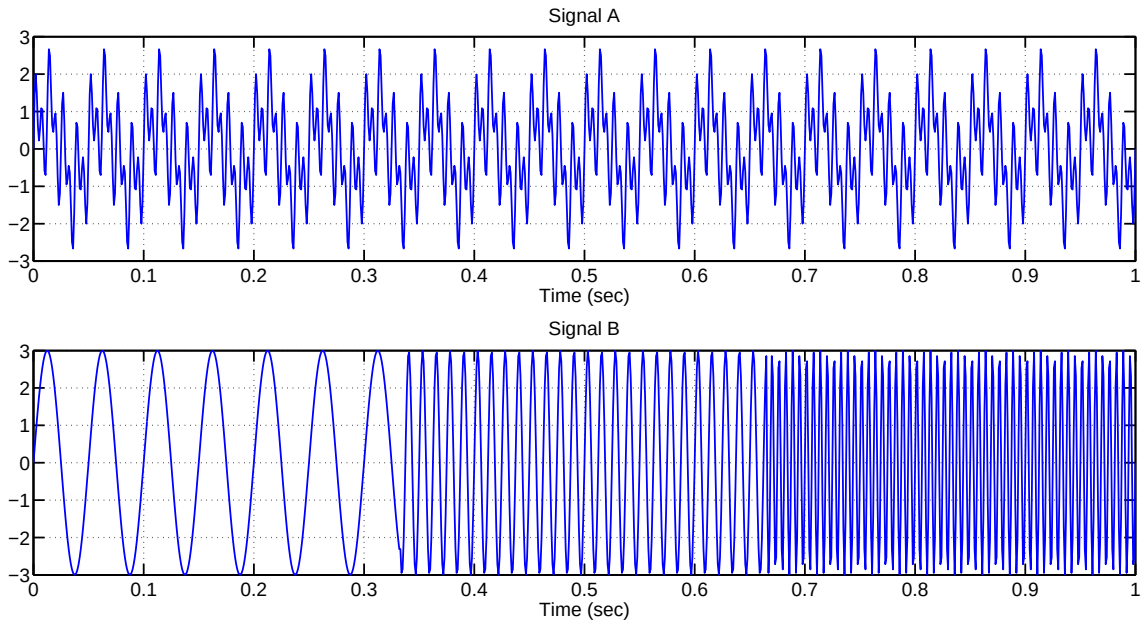

Figure 2.1: Example of signals: signal A and signal B sinusoidal based signals.

Both signals consist of three frequencies. The first, the signal A, is formed by superposing three sinusoidal waves, each one at a different frequency (20, 80 and 160 Hz). The second, the signal B, is formed by the same three frequencies, and the three sinusoidal waves have not been added but positioned next to each other. This means each third of the signal presents only one frequency, different from the other. The differences between these signals can be easily verified. Figure 2.2 shows the result of applying the Fourier Transform to these two signals and the frequencies that compose them. As previously stated, without the temporal information, the information given by the frequency analysis does not allow a clear distinction between the different signals.

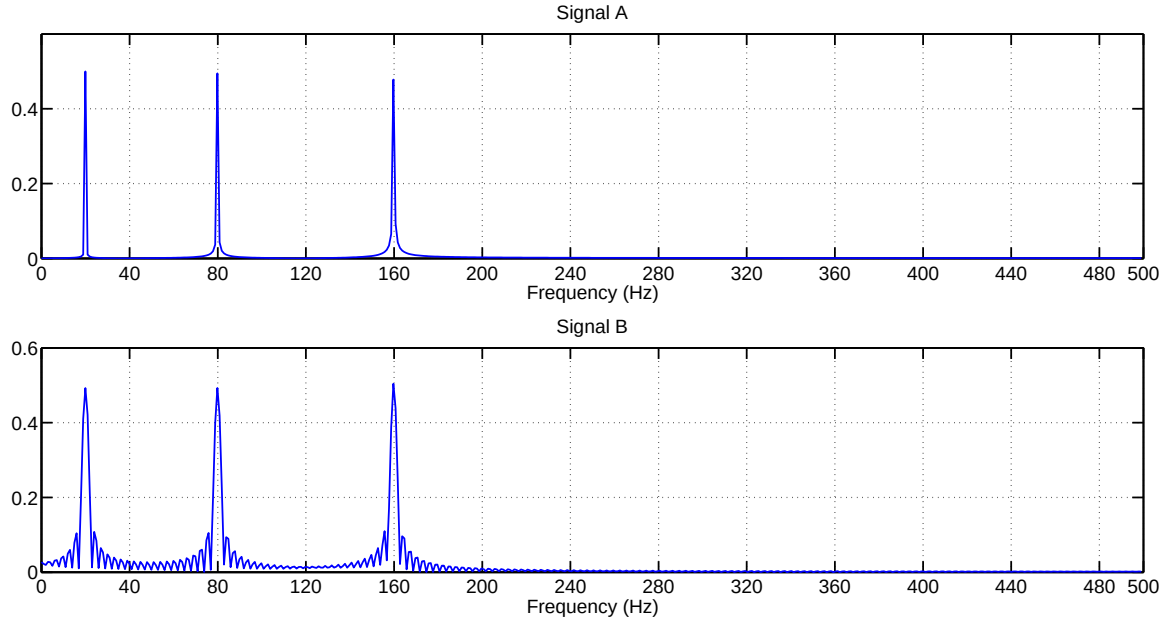

Figure 2.2: Fourier Transform response of signal A and B.

An alternative to consider the differences of these signals is the Short-Time Fourier Transform described in the next section.

2.2 The Short Time Fourier Transform and the Spectrogram

The Short-Time Fourier Transform (STFT) tries to analyze the signals not only in the time domain or in the frequency, but in both. According to (QUATIERI, 2002), it is not possible to characterize changes in the time-varying spectral content of a signal analysis using the Fourier Transform. However, the STFT consists of a separate Fourier Transform for every time. As a consequence, it is possible to determine the spectral variation of the signal in a time interval.

For the continuous STFT, the function to be transformed is multiplied by a non-zero window function for a short period of time. Thus, the Fourier Transform of the resulting signal is calculated as the window is moved along the time axis, resulting in a two-dimensional representation of the signal. Mathematically this process is given by

$$X(\tau, f) = \int_{-\infty}^{\infty} x(t)h(t-\tau)e^{-j\omega t}dt \tag{2.4}$$

where $h(t)$ is the window function and $x(t)$ is the signal to be transformed. The time index, τ, is normally considered to be "slow" time and usually not expressed in a high resolution compared to the time t (HLAWATSCH AND AUGER, 2008).

The Discrete STFT is more important in computational terms since the discrete signal to be transformed can be divided into different parts. To avoid problems with the boundaries (the ends) of the signals, these parts are superposed, creating an overlap. The overlap percentage must be set at the beginning of the process. According to (OPPENHEIM AND SCHAFER, 2010), the Discrete STFT equation is given by:

$$X(l, f) = \sum_{k=-\infty}^{\infty} x[k]h[k-l]e^{-j\omega k} \tag{2.5}$$

where $x[k]$ is the discrete signal and $h[k]$ is the window, l is the discrete "slow" time and usually is not expressed in a high resolution as discrete time k. After dividing the signal into several time intervals, the Fourier Transform is applied to each of these intervals as shown in Figure 2.3. A matrix is generated from these intervals and will be used to create a color map. Frequently, the vertical axis can be represented by time or space, the horizontal axis represents the frequencies and the colors show the intensities (the peaks) in each frequency.

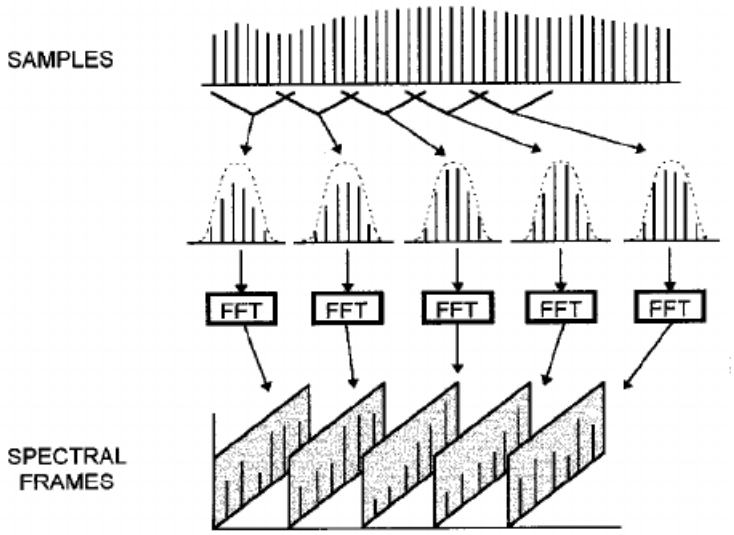

Figure 2.3: Overlap during a STFT (FISCHMAN, 1997).

Some parameters of the analysis should be considered for an adequate use of the STFT. As early stated, it should be defined the window function as well as the overlap percentage.

The window size must also be set and will not be modified until the analysis is done. This definition affects the time/frequency resolution of the STFT that must be a balance between the resolution of time and frequency. As a manner of fact, prioritizing one of them compromises the other. Frequency resolution of a spectrogram is connected to time window length and sampling frequency by following relation:

$$\Delta f = f_s/L \tag{2.6}$$

where Δf is the frequency resolution, f_s is the sample frequency and L is the length of window. If the signal is divided into very small windows, then the spectrum will have a good resolution in a time-varying analysis but reducing the frequency resolution and the spectrum amplitude. Thus, this can be more appropriate to see the changes in the spectrum during time. On the other hand, if the signal is divided into long windows, the frequency will have a better resolution, but decreasing the resolution in the time. This may not be appropriate for a spectrum varying during the time but better for detail frequency analysis (HLAWATSCH AND AUGER, 2008). This relation is shown in Figure 2.4.

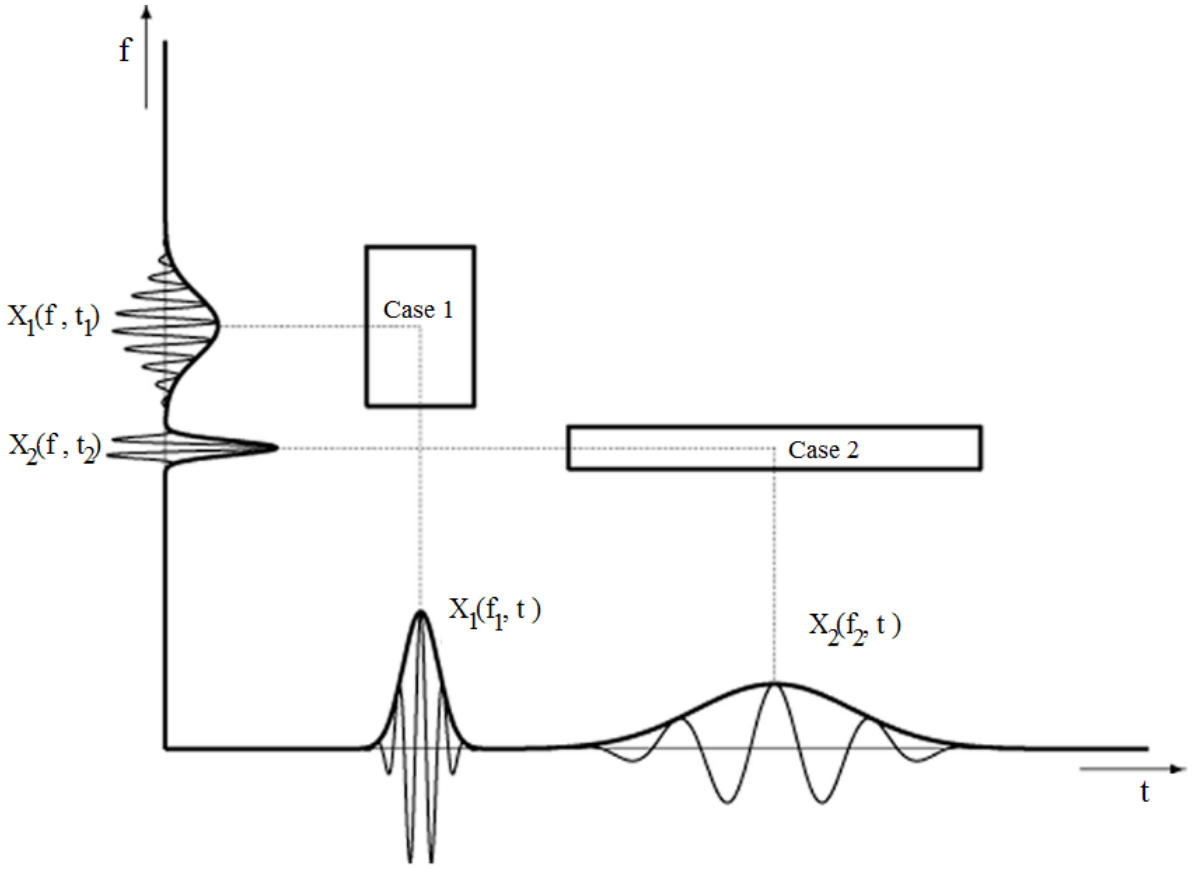

Figure 2.4: Frequency versus time resolutions: case 1-good time resolution, case 2-good frequency resolution.

Figure 2.4 illustrates the two types of the spectrogram analysis. X_1 represents the *wideband spectrogram*, which is the STFT of a signal with a short window function. This analysis permits a better temporal resolution and finding temporal variations in the spectrum, but at the same time degrades the spectrum amplitudes in the frequency domain. So the wideband spectrogram may be better to evaluate the spectrum at specific times with a better temporal resolution. On the other hand, X_2 is the STFT of a long window function, so-called a *narrowband spectrogram*, which represents a better spectral resolution in the frequency domain, but degrades the temporal resolution (QUATIERI, 2002). The narrowband spectrogram may be better to determinate the spectrum of a specific frequency with a better frequency resolution.

Taking as an example the signals shown in Figure 2.1, it is possible to demonstrate how the STFT works showing the frequency analysis and location (in time or space) of the changes occurred. Figure 2.5 shows the color map of both signals, where the horizontal axis

represents time and the vertical axis represents the frequencies of the signal portions. The colors show the changes in intensity in frequency values. The higher values are related to the red, while the lower values are related to the blue. The first signal, represented in Figure 2.5, has the frequencies of 20, 80 and 160 Hz throughout its length.

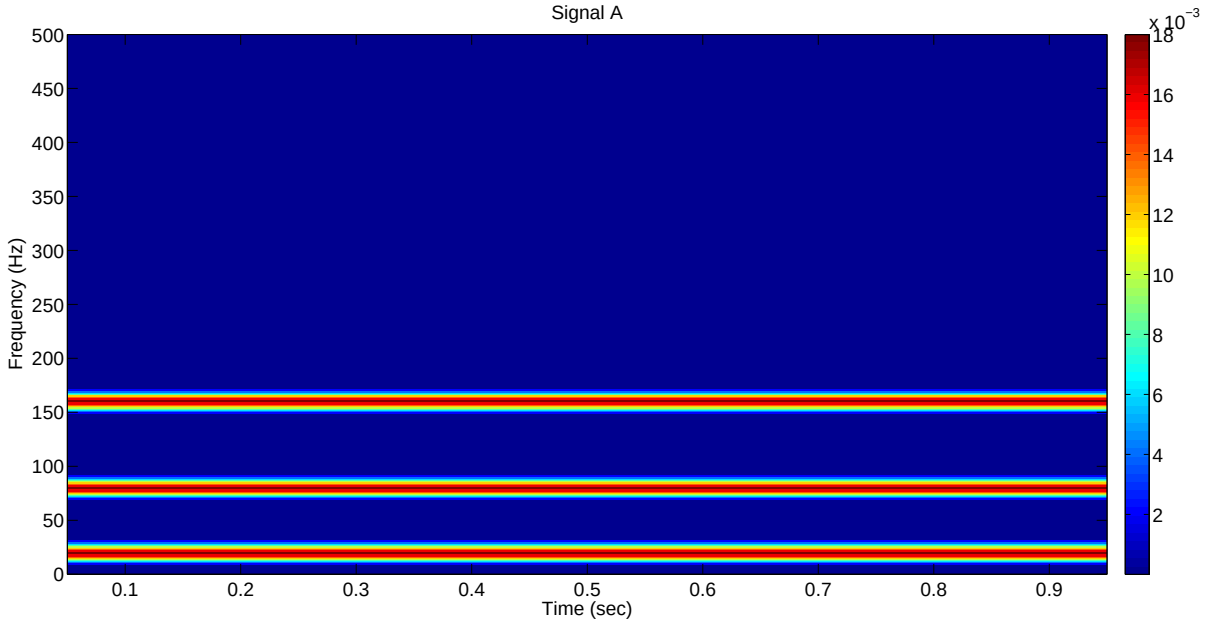

Figure 2.5: Spectrogram for Signal A.

The second signal illustrated in Figure 2.6, has only one frequency in each portion of the signal. The difference between the two signals is clearly seen in the analysis of their frequencies. It is important to note that the time axis allows the identification of the frequencies changes in the time domain.

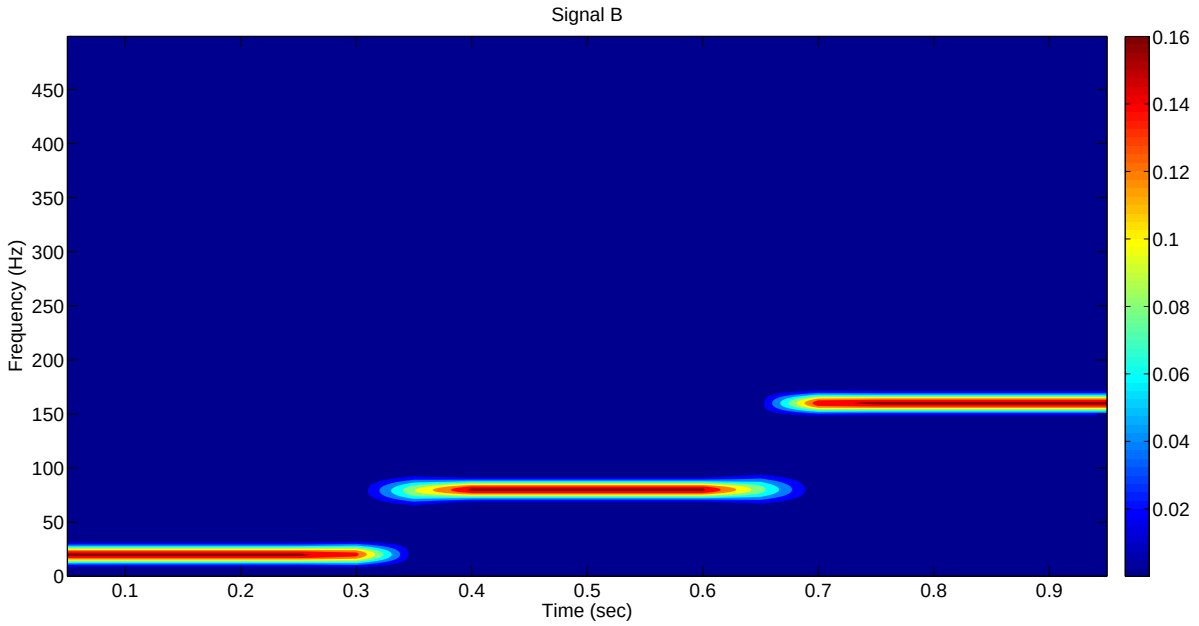

Figure 2.6: Spectrogram for Signal B.

This example shows the main utility of the STFT in the analysis of a frequency varying signal.

2.3 Artificial Neural Networks (ANN)

ANN are models that mimic the information in a similar way of biological neural networks present in nature (SUYKENS ET AL., 2012). ANN are composed by interconnected functional elements called *neurons*. A neuron is the basic unit of an ANN and its model is illustrated in Figure 2.7. The basic components are also shown in this figure. They are the synaptic weights, the summing junction and the activation function.

The neuron inputs are connected with a corresponding weight value. This means that an input x_i corresponds to a synapse m connected to neuron and consequently is multiplied by the *synaptic weight* w_i. The subscript m refers to the input. In an artificial neuron, synaptic weights can be found in a range that contains positive as well as negative values. Subsequently, the particular inputs signals weighted are added by the *summing junction*.

The output amplitude of the neuron is computed by a function known as the *activation function*. The activation function is also called the squashing function because it constrains the permissible amplitude range of the output signal to limit it in a range of finite value. The

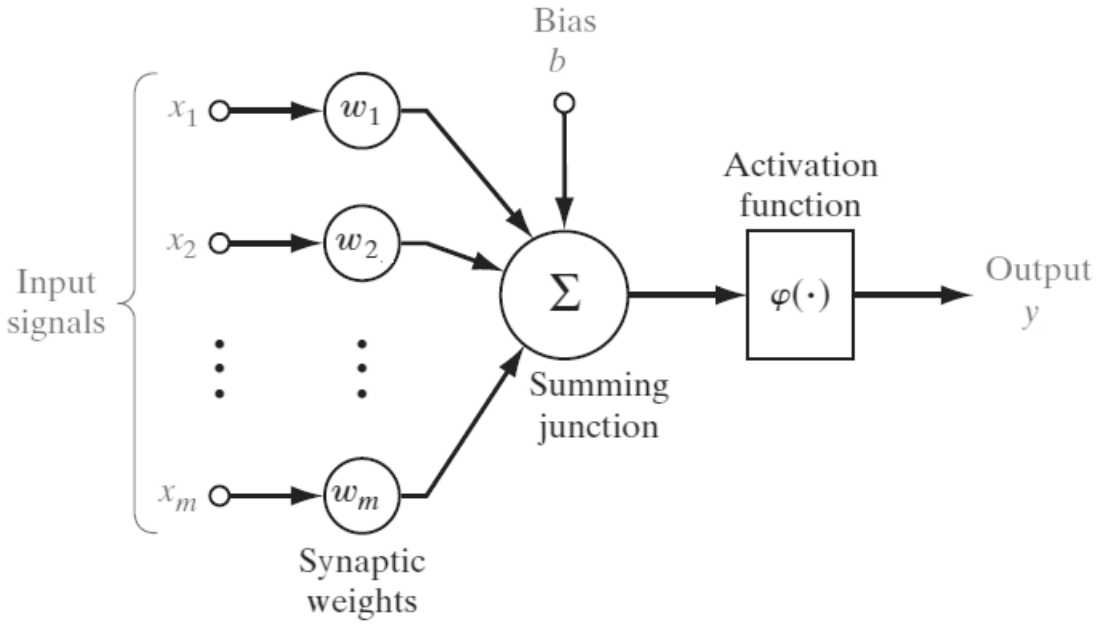

Figure 2.7: Artificial neuron model (HAYKIN, 2009).

neural model also incorporates an externally applied bias, denoted by b. The bias b, positive or negative, has the effect of rising or decreasing the net input of the activation function, respectively. Mathematically, the neuron model is represented as

$$\widehat{y} = \varphi(\sum_{i=1}^{m} w_i x_i + b_i) \tag{2.7}$$

where m is the total number of inputs and φ is the activation function. The activation function φ is part of the network design and may be a linear or a nonlinear function. Thus, there are a great number of possibilities for activation functions. The commonly used are illustrated in Figure 2.8. Linear (Figure 2.8(a)), hyperbolic tangent (Figure 2.8(b)), sigmoid (Figure 2.8(c)) and threshold (Figure 2.8(d)) functions are shown.

2.3.1 Network Architecture

The neurons are organized in layers depending on the application and with a certain learning algorithm. Frequently, the neurons in the layer have the same activation function. The way the neurons are linked in the layers conform the network structure. The three more common structures are the *single layer feedforward, multilayer feedforward* and the *recurrent network*.

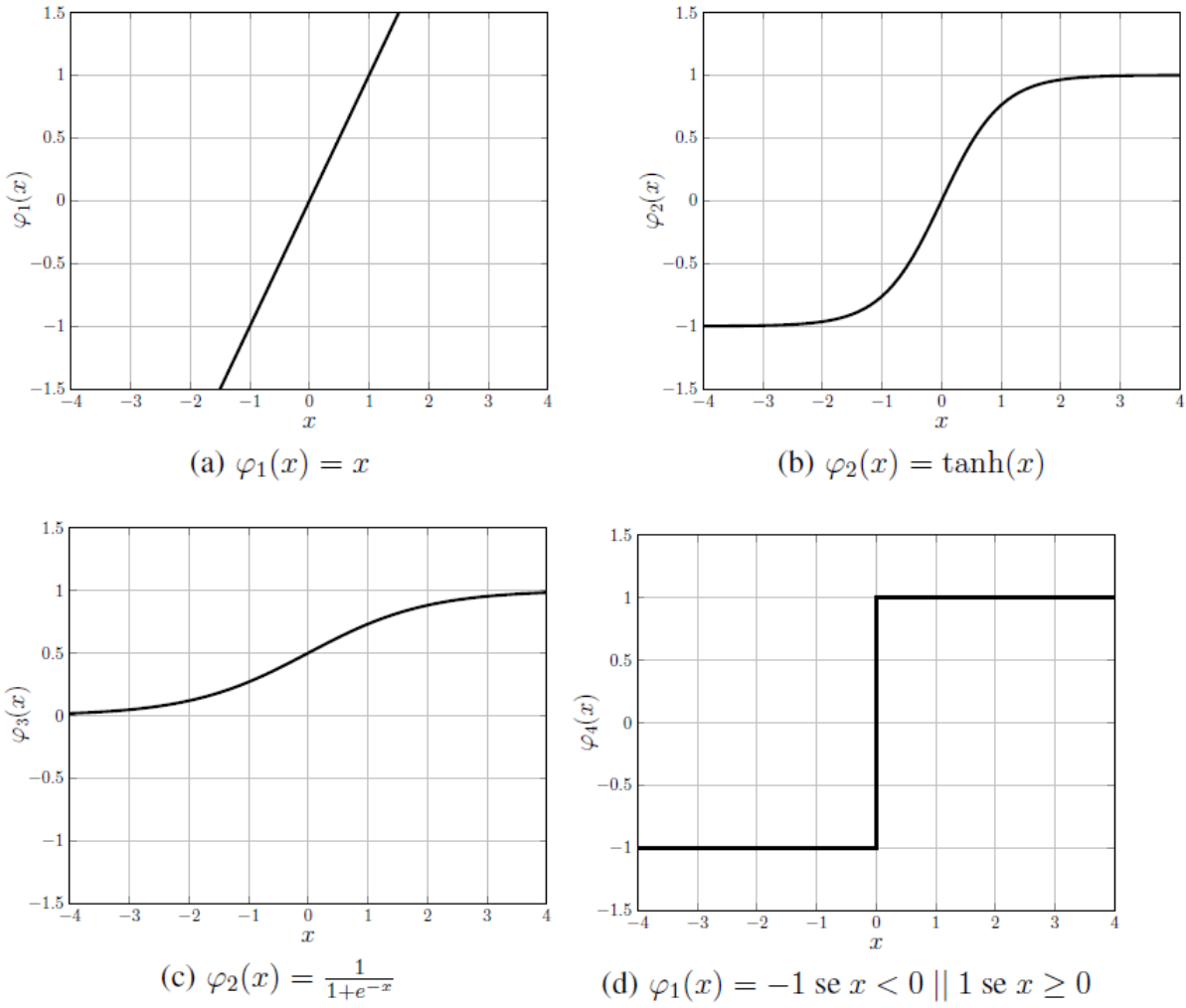

(a) $\varphi_1(x) = x$

(b) $\varphi_2(x) = \tanh(x)$

(c) $\varphi_2(x) = \frac{1}{1+e^{-x}}$

(d) $\varphi_1(x) = -1$ se $x < 0$ || 1 se $x \geq 0$

Figure 2.8: Activation function commonly used in ANN.

The single layer is the simplest form of a layered network. The input layer is the source for all nodes that transmit information directly to the output layer of neurons. In Figure 2.9, a single layer is illustrated. The term simple layer is widely used in this field, because of the output layer is the responsible part for calculating the network response. The input layer is not considered because it is a source of the nodes and doesn't perform any calculation.

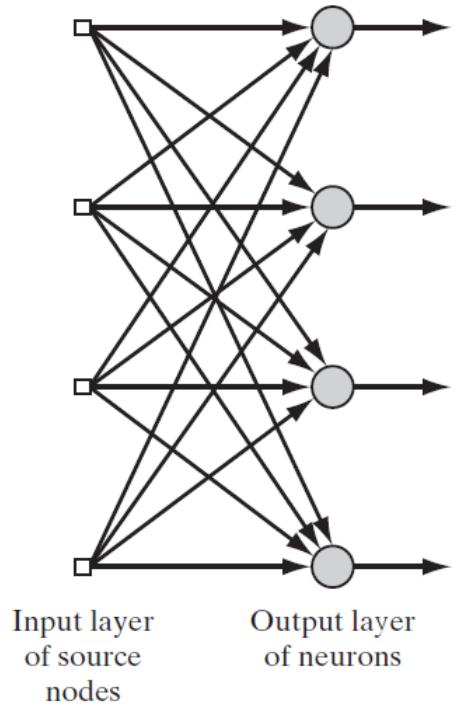

Figure 2.9: Simple layer neural network structure (HAYKIN, 2009).

Multilayer feedforward is a neural network that has the addition of one or more hidden layers as the main characteristic. Its nodes are correspondingly called hidden neurons because the input and output of the network are not able to "see" directly these neurons. The hidden layer has the purpose to be between the external inputs and the network outputs for some convenient aspect. The addition of one or more hidden layers to the network makes possible to extract higher-order information from their inputs. In spite of their local connectivity, the network obtains a general perspective, considering the additional set of synaptic connections and the additional dimension of the neural interactions.

The input layer of the network provides the information to the corresponding elements of the activation pattern, which are the input signals employed to the neurons in the second layer, also called the hidden layer. The second layer outputs are employed as inputs for the

third layer, and so on for the next layers of the network. Frequently, the synapse connections between every corresponding neuron in the layer have as inputs the outputs of the preceding layer only. The final layer outputs are the response of the neural network. The Figure 2.10 shows a typical multilayer feedforward neural network structure.

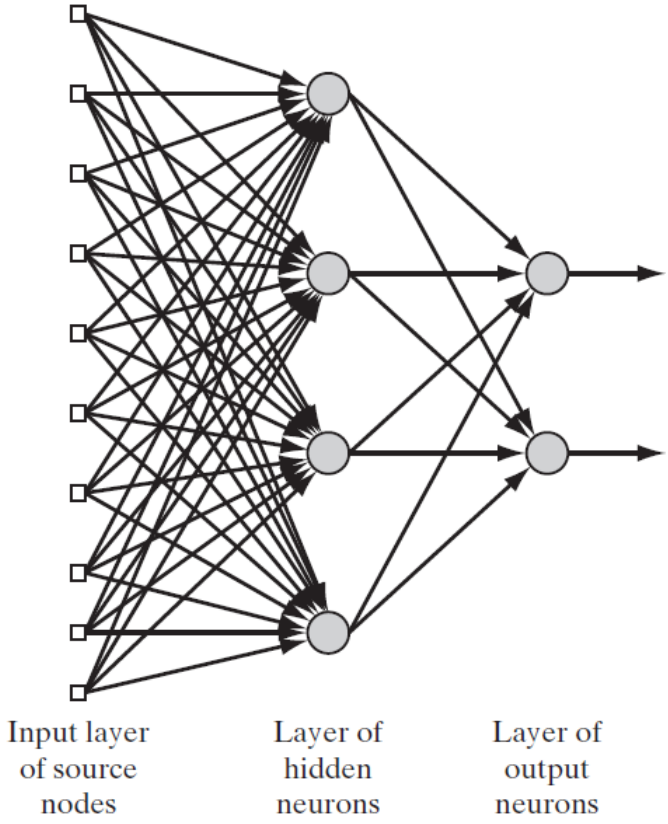

Figure 2.10: Multilayer feedforward neural network structure (HAYKIN, 2009).

The principal characteristic of the recurrent neural network is that it has at least a feedback loop, differing from the feedforward neural network. An example is a network with a single layer of neurons with every neuron feedbacking its output signal back to the inputs neurons in the layer. This structure has a deep effect on its performance and on its learning capability. The Figure 2.11 shows the feedback connections between the outputs, which are part of the source for the neuron, and the neuron's input.

It can be seen that the feedback loops use a block composed of unit-time delay elements (denoted by z^{-1}), which add a nonlinear dynamic behavior, assuming that the neural network has nonlinear activation functions.

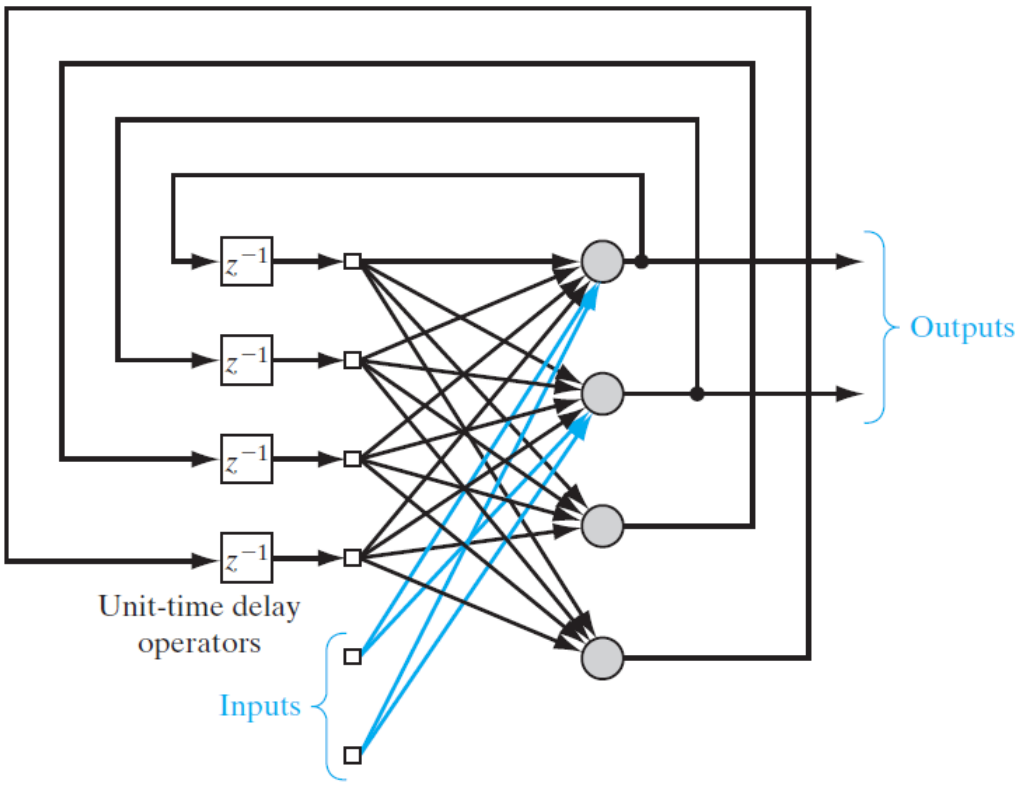

Figure 2.11: Recurrent neural network structure (HAYKIN, 2009).

2.3.2 Learning process

The training phase, or learning phase, refers to a minimization problem. The goal is to obtain the optimal values of the vector of synaptic weights $\boldsymbol{W}$ (the vector of all neurons weights w_{km}) of all connections of neurons in the ANN, using the inputs and outputs data set of the system. The inputs and outputs are obtained previously in an experiment or in a simulation (NØRGÅRD ET AL., 2000). The ANN models the relation between the inputs and the outputs in a system, changing the values of the weights according to a function of performance or cost function to be optimized.

The ANN training process for a system identification can be seen in Figure 2.12, where $x(k)$ is the input signal applied to the plant to be identified, $y(k)$ is the output of the plant and $\widehat{y}(k)$ is an ANN estimation of plant output. $\widehat{y}(k)$ is compared with $y(k)$ through a stopping criterion in order to adjust the synaptic weights of the network through the optimization process.

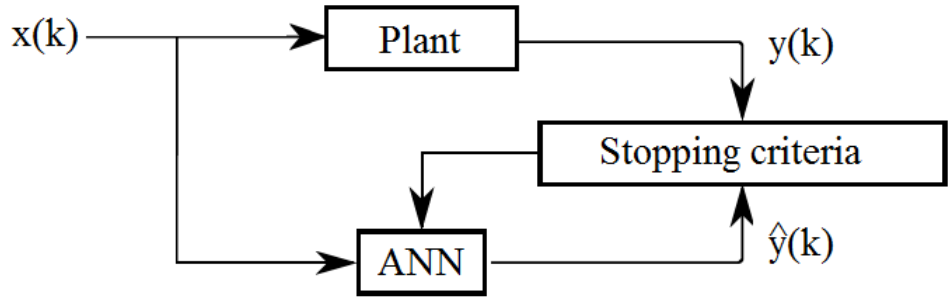

Figure 2.12: ANN training process.

The most commonly performance measure for this type of problem is the mean square error (MSE), which is calculated as follows:

$$\varepsilon(\boldsymbol{W}) = \frac{1}{2N}\sum_{i=1}^{N}[y_i - \hat{y}_i(\boldsymbol{X}, \boldsymbol{W})]^2 \tag{2.8}$$

where $\boldsymbol{W}$ is the vector of synaptic weights and biases of the ANN, $\boldsymbol{X}$ is the input vector of both ANN and system, $y_i(k)$ and $\widehat{y}_i(k)$ are the elements of the vectors of the system output and the ANN estimate respectively. So, given the input and the output, the vector $\boldsymbol{W}$ is modified to ensure the minimum MSE, and as consequence, the best approximation of $\widehat{y}_i(k)$ to $y_i(k)$. The optimization problem can be described as:

$$\boldsymbol{W}^* = \min_{\boldsymbol{W}} \ \varepsilon(\boldsymbol{W}) \tag{2.9}$$

where $\boldsymbol{W}^*$ is the optimal vector resulting from the training process.

The most common method for training an ANN is the back-propagation algorithm, which is a specific implementation of the gradient method, also called the steepest descending method. The weights matrix adjustment employed by the gradient method is given by

$$\boldsymbol{W}_{n+1} = \boldsymbol{W}_n - \eta \boldsymbol{g}_n \tag{2.10}$$

where η is a positive constant known as learning rate or stepsize, $\boldsymbol{g}_n$ is the gradient vector evaluated at the point $\boldsymbol{W}_n$, and n is the iteration number. In addition, second order methods are also used, which use the information from the Hessian matrix or an approximation of it. Usual second-order methods are the Newton method, Quasi-Newton method, Gauss-Newton,

the Pseudo-Newton method and the Levenberg-Marquardt method. The equations for some of these algorithms are

- Newton method

$$\boldsymbol{W}_{n+1} = \boldsymbol{W}_n - \boldsymbol{H}_n^{-1}\boldsymbol{g}_n \tag{2.11}$$

- Quasi-Newton method

$$\boldsymbol{W}_{n+1} = \boldsymbol{W}_n - (\boldsymbol{J}_n^{\mathbf{T}}\boldsymbol{J}_n)^{-1}\boldsymbol{J}_n\boldsymbol{e}_n \tag{2.12}$$

- Levenberg-Marquardt method

$$\boldsymbol{W}_{n+1} = \boldsymbol{W}_n - (\boldsymbol{J}_n^{\mathbf{T}}\boldsymbol{J}_n + \lambda\boldsymbol{I})^{-1}\boldsymbol{J}_n\boldsymbol{e}_n \tag{2.13}$$

where $\boldsymbol{H}_n$ is the Hessian matrix, $\boldsymbol{J}_n$ is the Jacobian matrix, λ is a regularization factor and $\boldsymbol{e}_n$ is the error between $\widehat{y}_n$ and y (HAYKIN, 2009).

The Levenberg-Marquardt training algorithm is normally used for the ANN. In some cases, this algorithm allows the overfitting error in the ANN model. This error occurs when the ANN is not able to predict new data but has a low error on the training set. To consider this aspect, a modification of the training algorithm for a more suitable generalization is required. For this purpose, a modification of the algorithm based on the Bayesian Regularization in combination with the Levenberg-Marquardt algorithm is suggested (DEMUTH AND BEALE, 1993). The cost function of Bayesian regularization is:

$$\varepsilon(\boldsymbol{W}) = \beta E_D + \alpha E_W; \tag{2.14}$$

where E_D represents the error sum square, E_W is the sum of square of the weight, α and β are the regularization parameters. This type of training changes the performance function normally used on Levenberg-Marquardt base as following

$$\varepsilon(\boldsymbol{W}) = \frac{\beta}{2}\sum_{i=1}^{N}\left[y_i - \hat{y}_i(\boldsymbol{X}, \boldsymbol{W})\right]^2 + \frac{\alpha}{2}\sum_{m=1}^{M} w_m^2 \tag{2.15}$$

The size of these values can emphasize the type of training. If $\alpha \ll \beta$, then the training equation will emphasize the error minimization. If $\alpha \gg \beta$, then the training will emphasize the weight reduction, making a smoother response (FORESEE AND HAGAN, 1997). α and β can be calculated by using the Mackay Method (MACKAY, 1991) using the following

$$\alpha = \frac{\gamma}{2E_W(\mathbf{W})} \tag{2.16}$$

$$\beta = \frac{N-\gamma}{2E_D(\mathbf{W})} \tag{2.17}$$

where N is the number of data training, γ is called the effective number of parameters and it is calculated as

$$\gamma = M - 2\alpha \mathbf{tr}((2\beta \boldsymbol{J}_k^{\mathbf{T}} \boldsymbol{J}_k + 2\alpha \boldsymbol{I})^{-1}) \tag{2.18}$$

where M is total number of weights in the network, $\boldsymbol{I}$ is the identity matrix, and **tr** is the trace of a matrix.

The parameter γ is a measure of how many parameters in the neural network are effectively used in reducing the error function. After the last iteration of the ANN, if the final value of γ is close to the number of data training N, then ANN may not represent the response properly. In that case, a possible solution is to increase the number of neurons or/and the number of hidden layer until the value of γ stabilizes. When this happens if the larger network has the same γ as the smaller network, then the smaller network could be enough to represent the response (FORESEE AND HAGAN, 1997).

2.3.3 ANN Dynamic modeling

In this section, the dynamic identification of the FSW process using ANN and the Nonlinear Auto-Regressive with eXternal input (NARX) model is described. To identify the nonlinear dynamic behavior of a system, the NARX equation is usually employed to form a structure with an ANN. The NARX model consists of a time series data that allows to understand not only the actual dynamic, but also is able to predict the future values using the current and past data (NELLES, 2001). The equation of a NARX model is generally defined as:

$$y_t = F(y_{t-1}, y_{t-2}, y_{t-3}, \ldots, y_{t-k}, x_{t-1}, x_{t-2}, x_{t-3}, \ldots, x_{t-dl}) \tag{2.19}$$

where y_t represents the output, $y_{t-1}, y_{t-2}, y_{t-3}, \ldots, y_{t-dl}$ represent their backward time-shifts, x_t represents the input, $x_{t-1}, x_{t-2}, x_{t-3}, \ldots, x_{t-dl}$ their time-shifts, and dl represents the total number of backward time-shifts. F represents an unknown nonlinear function (NELLES, 2001) to be determined. For this research, the nonlinearity is added when the ANN is used in this type of model; in this case sigmoid functions were used in all neurons of hidden layer and the output layer. A structure of the NARX model is presented in Figure 2.13.

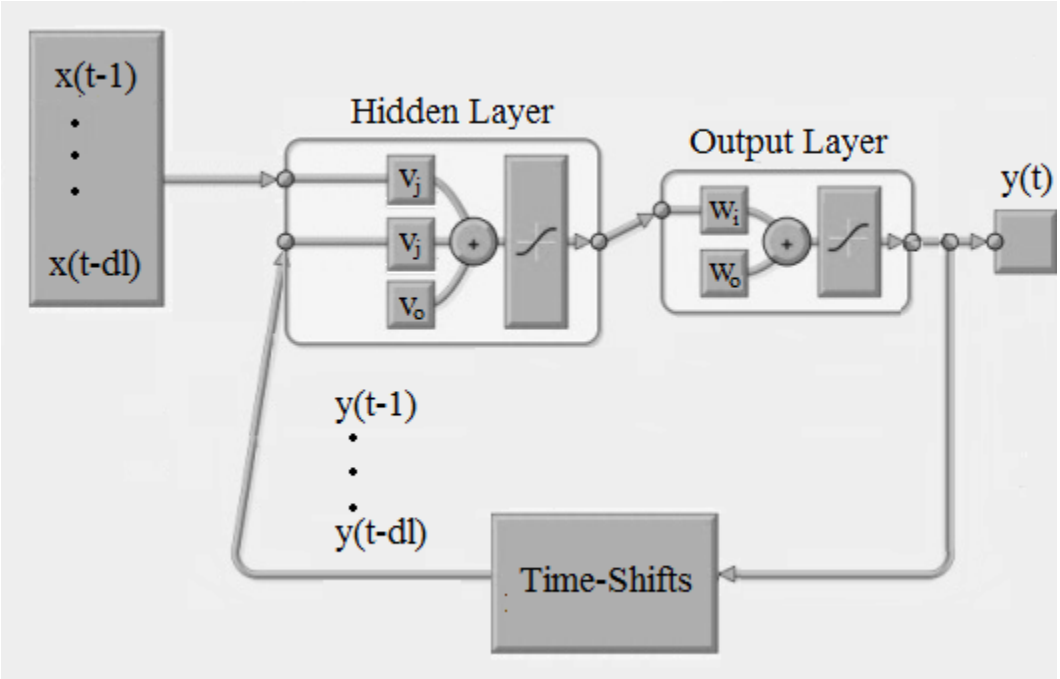

Figure 2.13: NARX using artificial neural network.

It is possible to notice in Figure 2.13 that the model inputs can consider also the delays of the outputs, which are part of the NARX formulation. Some functions used in the ANN are nonlinear in this case.

2.4 Fuzzy logic

In computer science, the fuzzy logic is included as part of the soft computing (also called computational intelligence) with other several computing paradigms including machine learning, evolutionary computation, and probabilistic reasoning, which can be used to form powerful hybrid intelligent systems. Fuzzy logic consists of the association of the uncertainty with the structure of a data set (ZADEH, 1965). The fuzzy systems are described as a knowledge-based system expressed in a linguistic form. For this reason, the design of fuzzy model depends on the experience and the human heuristic knowledge.

2.4.1 Fuzzy sets and Membership functions

The elements of a fuzzy set are ordered pairs that indicate the value of the element and its degree of membership. A fuzzy set is defined as:

$$A = \{(x, \mu_A(x)) | x \in X\} \tag{2.20}$$

where A is the fuzzy set, $\mu_A(x)$ is the membership function and x the element that belongs to the set A with a degree of membership $\mu_A(x)$, which can vary between 0 and 1. Therefore, a variable can be characterized by different linguistic values, each of them representing a fuzzy set.

For example, speed can be characterized by linguistic values such as "Low", "Medium" and "High", which represent "a speed of approximately 30 km/h", "a speed of about 60 km/h" and "a speed of about 90 km/h" respectively. These terms are associated to fuzzy sets with membership functions as shown in the Figure 2.14.

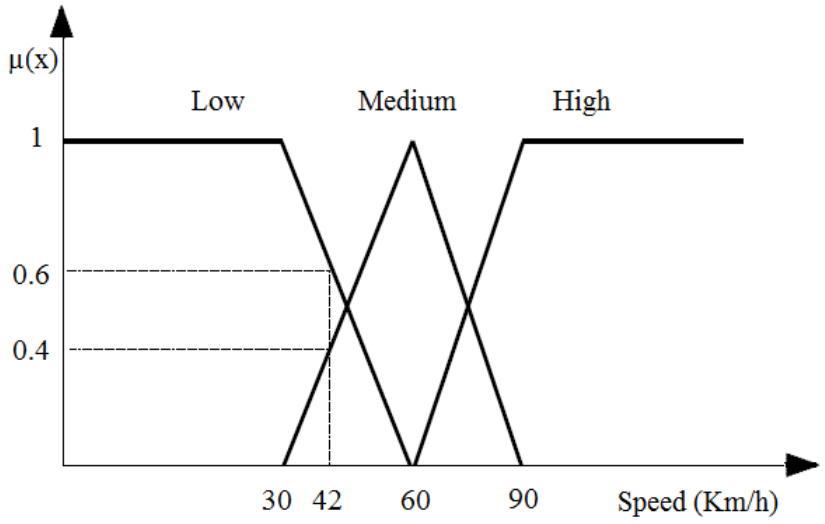

Figure 2.14: Examples of a fuzzy sets and membership functions.

Therefore, if the speed is 42 km/h, there are 3 degrees of membership 0.6, 0.4 and 0 to the fuzzy sets "Low", "Medium" and "High" respectively.

2.4.2 Membership function (MF)

There are several types of membership function. The most used are: triangular, trapezoidal, gaussian and generalized bell. A triangular MF is specified by three parameters, a, b and c, as follows:

$$\mu(x) = \begin{cases} 0, & x \leq a. \\ \dfrac{(x-c)}{(b-a)}, & a \leq x \leq b. \\ \dfrac{(c-x)}{(c-b)}, & b \leq x \leq c. \\ 0, & c \leq x. \end{cases} \tag{2.21}$$

where the parameters a, b, c (with $a < b < c$) determine the x coordinates of the three corners of the underlying triangular MF.

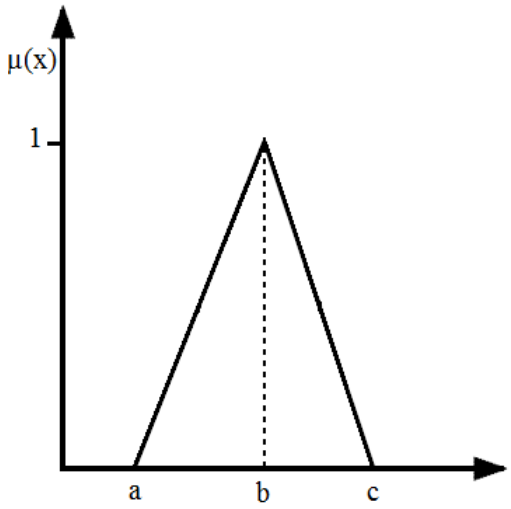

Figure 2.15: Triangular membership functions.

A trapezoidal MF is specified by four parameters, a, b, c and d, as follows:

$$\mu(x) = \begin{cases} 0, & x \leq a. \\ \dfrac{(x-a)}{(b-a)}, & a \leq x \leq b. \\ 1, & b \leq x \leq c. \\ \dfrac{(d-x)}{(d-c)}, & c \leq x \leq d. \\ 0, & d \leq x. \end{cases} \tag{2.22}$$

where $a < b \leq c < d$ determine the x coordinates of the four corners trapezoidal MF. Figure 2.16 presents a typical trapezoidal MF.

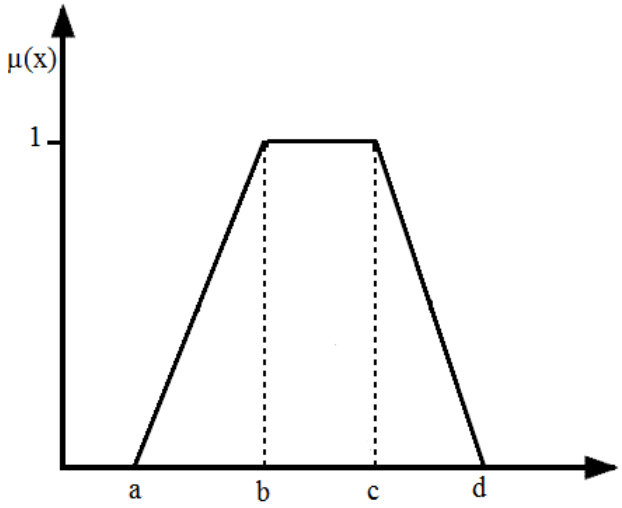

Figure 2.16: Trapezoidal membership function.

A Gaussian MF is specified by two parameters, c and σ, according to:

$$\mu(x) = e^{\frac{-(x-c)^2}{2\sigma^2}} \tag{2.23}$$

where c represents the MF center and σ determines the MF width. Figure 2.17 shows a Gaussian MF.

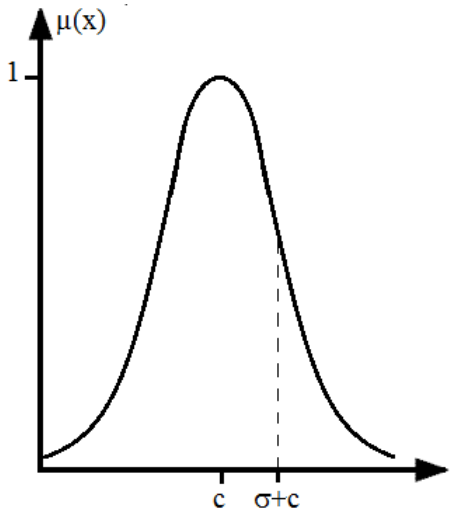

Figure 2.17: Gaussian membership function.

A generalized bell MF is specified by three parameters, a, b and c, according to:

$$\mu(x) = \frac{1}{1 + |\frac{x-c}{a}|^{2b}} \tag{2.24}$$

where the parameter b is positive. This function also known as Cauchy MF, because is based in a direct generalization of the Cauchy distribution used in probability theory. The Figure 2.18 illustrates this function.

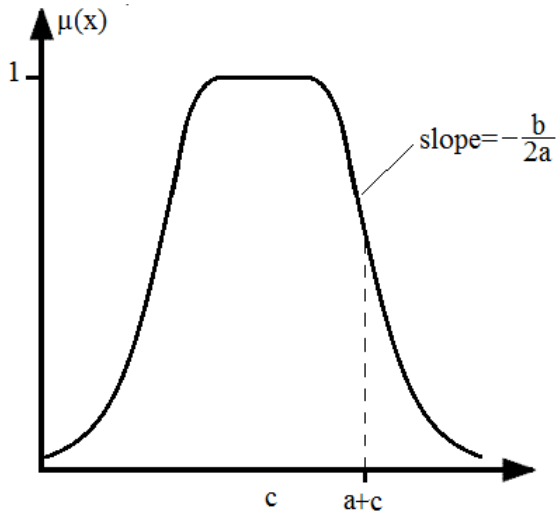

Figure 2.18: Generalized Bell membership function.

2.4.3 Fuzzy logic basic operations

For two fuzzy sets A and B in the same universe X, with membership functions μ_A and μ_B, respectively, you can define the following basic operations:
Union. The membership function union of A and B can defined as:

$$\mu_{A \cup B} = max\{(\mu_A(x), \mu_B(x))\} \tag{2.25}$$

Intersection. The membership function of the intersection of A and B is:

$$\mu_{A \cap B} = min\{(\mu_A(x), \mu_B(x))\} \tag{2.26}$$

Complement. The membership function of the complement of A is defined as:

$$\mu_{\overline{A}}(x) = 1 - \mu_A(x) \tag{2.27}$$

Cartesian product. Given the fuzzy sets A_1,A_2, ... , A_n with universes X_1,X_2, ... , X_n respectively, we define the Cartesian product as a fuzzy set in $X_1 \times X_2 \times ... \times X_n$ with the following function of membership:

$$\mu_{A_1 \times A_2 ... \times A_n}(x_1, x_2, ..., x_n) = min\{\mu_{A_1}(x_1), ..., \mu_{A_n}(x_n)\} \tag{2.28}$$

For example, for A and B as fuzzy sets evaluated in $\mu_A(x_1)$ and $\mu_B(x_2)$, the Cartesian product is:

$$\mu_{A \times B}(x_1, x_2) = min\{\mu_A(x_1), \mu_B(x_2)\} \tag{2.29}$$

2.4.4 Fuzzy Modeling

The fuzzy models are based on a set of heuristic rules where the linguistic variables of the inputs and outputs are represented by fuzzy sets. The Figure 2.19 shows the main components of a Fuzzy linguistic model: fuzzy interface, knowledge base, inference engine and defuzzification interface (LEE, 1990), described in the following.

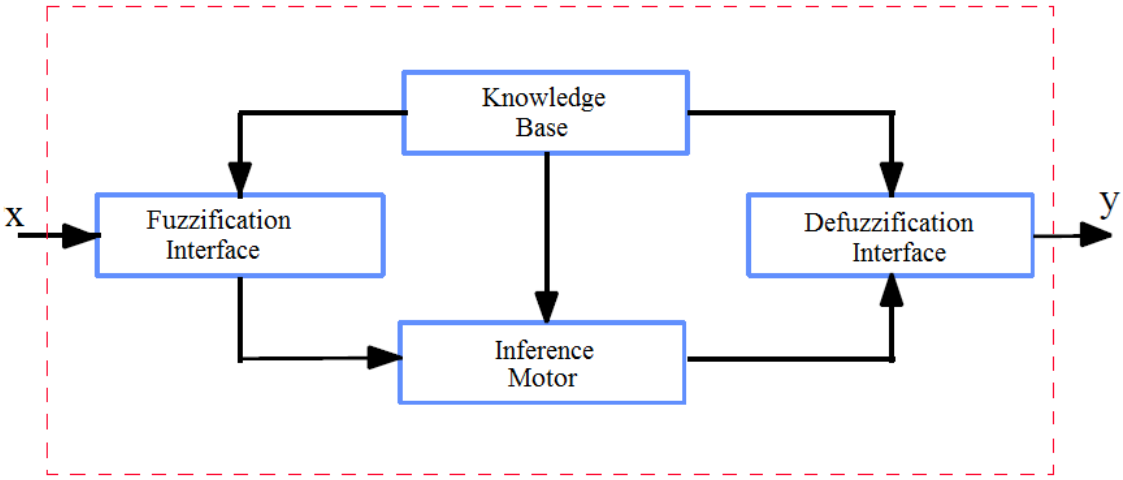

Figure 2.19: Fuzzy model representation.

Fuzzy interface. This element transforms the input variables of the model x into fuzzy variables. For this interface, the ranges of variation of the input variables and the fuzzy sets

associated with their respective membership functions must be defined.

Knowledge base. It contains the linguistic rules of the control and the information regarding the functions of membership of the fuzzy sets. These linguistic rules typically have the following form:

$$\text{If } x_1 \text{ is A and } x_2 \text{ is B, then } y \text{ is } C.$$

where A, B and C are the fuzzy sets of the input variables x_1 and x_2, and the output variable y respectively. There are several ways of deriving the rules (LEE, 1990), among which are those based on:

- *Expert experience and knowledge of control engineering*. The basis of rules is determined from interviews with the operator or through knowledge of the dynamics of the process.

- *Process modeling*. The parameters of the knowledge base are obtained from input and output data of the process.

Inference engine. It performs the task of calculating the output variables from the input variables, using the rules of the controller and the fuzzy inference, delivering fuzzy output sets. In general, we can say that a fuzzy inference system implements a non-linear mapping from its input space to output space. This mapping is accomplished by a number of fuzzy if-then rules, each of which describes the local behavior of the mapping. In particular, the antecedent of a rule defines a fuzzy region in the input space, while the consequent specifies the output in the fuzzy region. For example, given a knowledge base with n rules of the type:

$$\text{If } x_1 \text{ is } A_i \text{ and } x_2 \text{ is } B_i \text{ then } y \text{ is } C_i$$

where A_i represent one of the fuzzy sets associated with the input x_1, B_i represent one of the fuzzy sets associated with the input x_2, and C_i represent one of the fuzzy sets associated with the output y. The sequence of calculations performed by the inference engine includes:

- Determining the degree of compliance R_i of each rule from the degrees of membership of the input variables obtained in the fuzzification stage, that is:

$$R_i = min(\mu_{A_i}, \mu_{B_i}) \tag{2.30}$$

  Usually, the rules join the expression by the "AND" operator, and they are defined as the intersection of fuzzy sets.

- For each rule we have a consequence "y is C_i", which has associated a membership function μ_{C_i}. Therefore, we have an output set C_i, whose membership function is:

$$\mu_{C_i} = min(R_i, \mu_{C_i}) \tag{2.31}$$

  where R_i is the degree of compliance for rule i.

- To evaluate the total set of rules, the resulting fuzzy sets C'_i from each rule are joined, generating an output set with the following membership function:

$$\mu_{C'} = max(\mu_{C'_i}) \tag{2.32}$$

  In this way, we obtain a fuzzy output with a membership function μ'_C

Defuzzification interface. This element provides discrete and deterministic outputs from the fuzzy sets C' obtained as a result of the inference. There are different methods of defuzzification, some of which are described below:

- **Maximum method**. The output corresponds to the value for which the membership function μ_C reaches its maximum.

- **Mean of maximum**. The output is the average between the elements of the set C' which have a maximum degree of membership.

- **Centroid of area**. It generates as output the value corresponding to the center of gravity of the membership function of the output set C.

The model can be modified in any part to find the finest response. The use of the fuzzy logic during this thesis will be fundamental because the amplitude of spectrum changes in every variable analysis with its own intensity. The experiment made during the thesis explored variation on the amplitude of spectrum in different operation points.

3 Friction Stir Welding

3.1 Introduction

In this chapter the friction stir welding process was explained, giving more details on how the joint occurs and why some variables are so important for the process. In addition, the chapter describes all the system, equipment, measurement instruments, materials and details of the process used in this research. It also discusses the design of experiment including the parameters of interest and how the samples were taken.

3.2 Basic concepts of Friction Stir Welding Process

The Friction Stir Welding process is a relative new technique to join metals invented by The Welding Institute (TWI) in Cambridge, England, at the earlier 90's (THOMAS ET AL., 1995). The joint process is accomplished using a nonconsumable tool formed by a shoulder and a probe (KHALED, 2005). The rotating tool is plunged between the two pieces and, as a result of the combination of a deformation and friction heat, the material generates an extrusion and forging stirring effect (BUFFA ET AL., 2006) joining the two pieces. The tool rotates and moves on joint line completing the joining process.

The process has four main stages: the plunging, dwelling, welding and the lift-off of the tool. These stages are described in the following.

The plunging: At first, a rotating tool plunges into the workpiece until the entire probe is inserted and the tool's shoulder surface gets in contact with the joint. During this stage, the material flows around the probe tool and the plastic deformation process begins.

Dwelling: In this stage, the rotating tool maintains its position. The pressure and the friction, exerted by the tool's shoulder, heat the joint making the material softer. When the rotation speed reaches a constant value, the tool starts the movement and begins the welding stage.

Welding: In this stage, the FSW tool moves in the direction of the joint to be performed. During this stage, the flow around the tool generates the material extrusion to the backside of the probe, where the material is forged by the shoulder's force pressure.

Lift off: Finally, in the fourth stage, the tool stops and lift off the workpiece.

The main stages of the process are shown schematically in Figure 3.1.

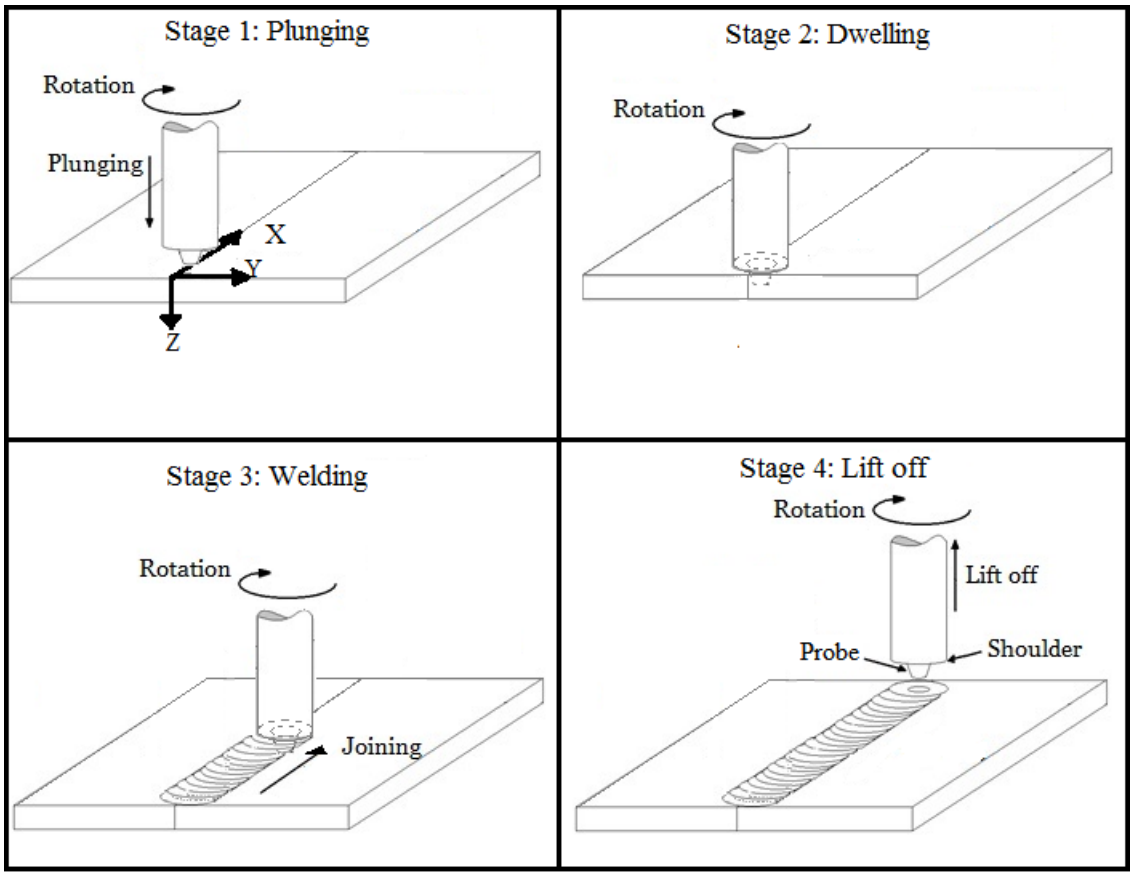

Figure 3.1: Scheme of the FSW process stages.

The resulting joint has extremely different metallurgical properties in comparison with the conventional methods. However, the FSW joint depends on the welding parameters used and on the tool geometry. The deviation from the correct parameters or the selection of the incorrect tool geometry could form undesirable defects in the joint. These aspects will be discussed next.

3.3 FSW Metallurgy

The joint resulting from a FSW process has specific characteristics divided by four zones illustrated in Figure 3.2.

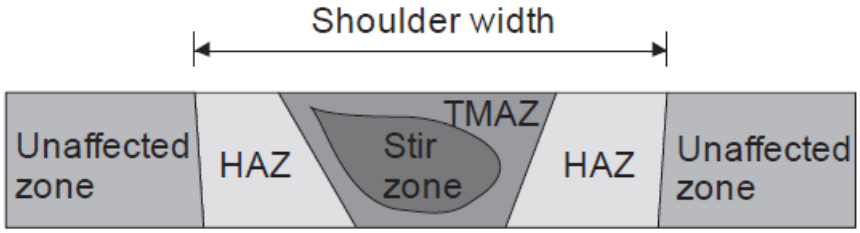

Figure 3.2: Scheme of the FSW resulting micro-structure zones (PODRZAJ ET AL., 2015).

The first zone is the material base (unaffected zone). This is the zone that was not affected by the process and maintains all the mechanical properties. The second zone is the Heat Affected Zone (HAZ), where the material is affected only by the thermal cycle. Due to this cycle, some of the localized properties in this zone change. The third zone is known as the Thermo-Mechanical Affected Zone (TMAZ). In this zone, the extreme plastic deformation and temperature affect the material properties. The fourth zone is known as the Stirred Zone (SZ) and this zone coincides with the center of the joint. The material in this zone has been submitted to 90% of fusion temperature and the extreme strain causes a finer grain microstructure (ZHI-HONG ET AL., 2004).

3.4 Tool geometries

The FSW tool has been evolving since the discovery of this technique (MISHRA AND MA, 2005). At the beginning, the FSW tool was only a cylindrical probe with a concave shoulder. Since then, a wide range of tool geometries has been developed. FSW tools can be categorized by the shoulder geometries in three types: flat, convex and concave. The types of shoulder geometry are shown in Figure 3.3. The first in Figure 3.3(a) is the most commercially used because of the cheap cost and ease fabrication. The convex tool, Figure 3.3(b), can rise a high range of depth penetration, and allows uniform contact with workpiece while increases the plunge depth. Finally, the concave tool, Figure 3.3(c), forms a space cavity during the initial plunge where the material flows up and fills the cavity. The material keeps flowing inside the cavity, which reduces flash formation in comparison to a flat shoulder.

On the other hand, there are three main probe constructions, i.e., fix probe, retractable probe and self-retracting probe. These probe constructions are illustrated in Figure 3.4. The fix probe, Figure 3.4(a), is the most common because it is cheap and easy to manufacture, and it is used in many applications. For the retractable probe, Figure 3.4(b), the shoulder remains

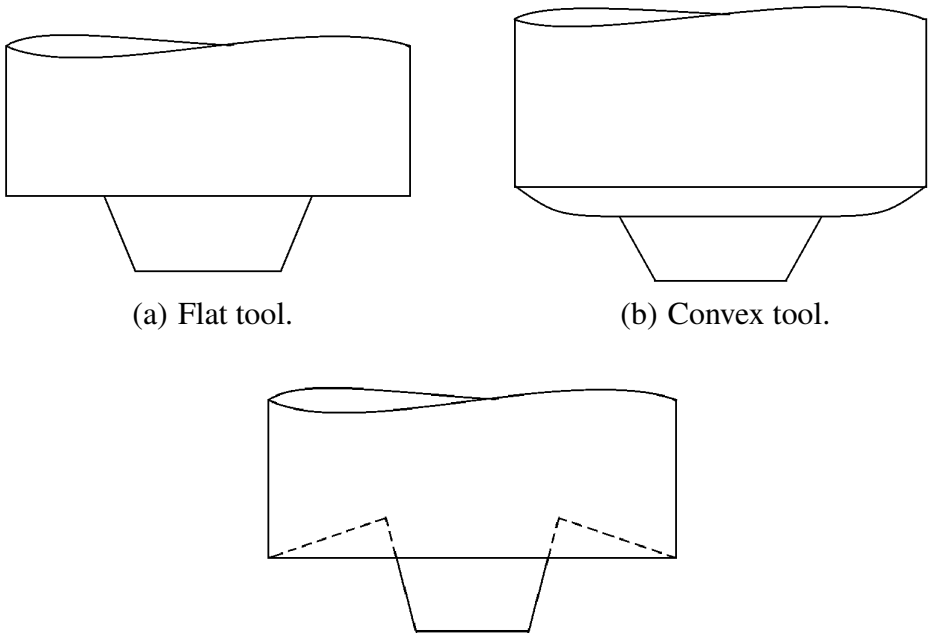

(a) Flat tool.

(b) Convex tool.

(c) Concave tool.

Figure 3.3: Types of shoulder geometries.

in contact with the workpiece, while the probe is plunged and removed from the workpiece. The self-retractable probe, Figure 3.4(c), has an adaptable lower shoulder included in the probe system that makes unnecessary the backing anvil used in the other styles. The adaptable of the upper and lower shoulders can generate heat at both sides of the welding joint. This additional input heat permits the tool moves at traversing speed faster than the other options.

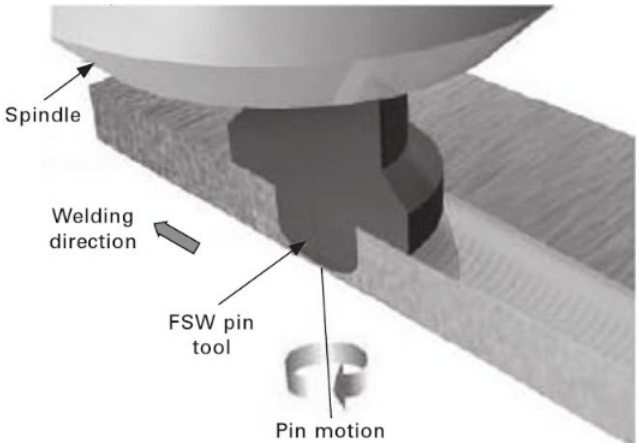

(a) Fix probe.

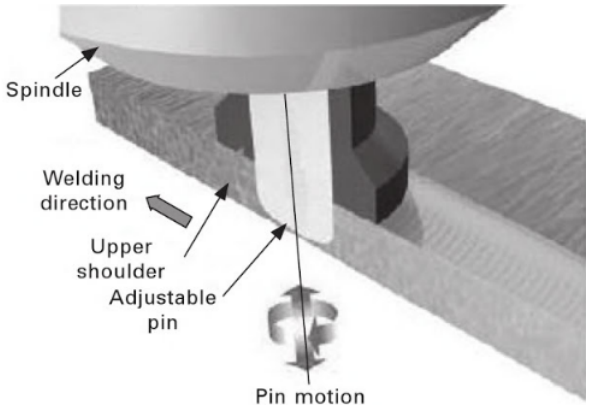

(b) Adjustable probe.

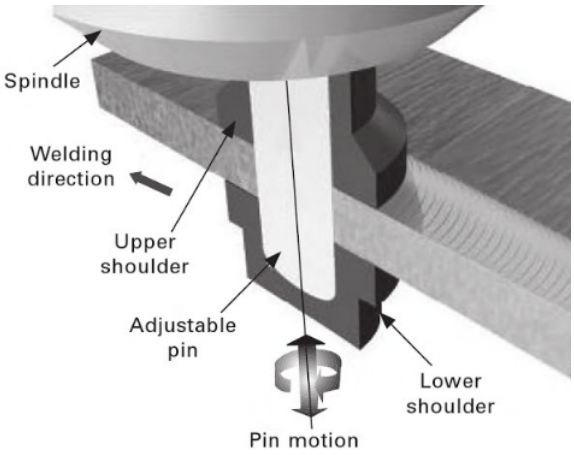

(c) Selfreacting probe.

Figure 3.4: Types of probe (or pin) constructions (LOHWASSER AND CHEN, 2009).

Another aspect that has an enormous importance is the probe geometry because it improves the material flow depending on style and shape. There is an innumerable number of probe geometry, for example, the cylindrical, threaded cylinders, triangular prism, oval, circular, conical and square profiles. The most commonly used are illustrated in Figure 3.5.

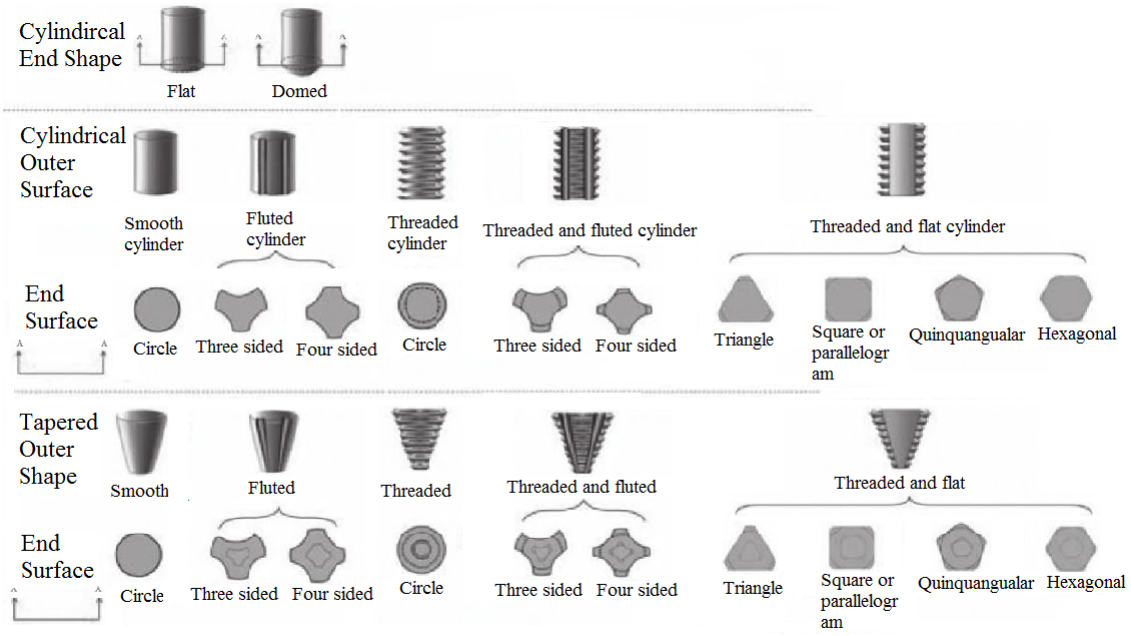

Figure 3.5: Types of probe geometries (MISHRA AND SIDHAR, 2016).

3.5 Process Parameters

As mentioned before, the FSW depends on a number of important parameters to make a good joint. However, this research is concentrated in the following parameters (KHALED, 2005).

The plunge depth: It is the position of the tool shoulder relative to the surface of the workpieces. This parameter is crucial for a good joint because increases the pressure applied by the tool, which guarantees a proper forging of the material in the backside of the probe.

Traversing speed: This parameter defines how fast the tool moves on the interface of the workpieces. The traversing speed influences the heat input during the FSW process. So when the traversing speed increases the heat input decrease.

Tool rotation speed: This parameter shows how fast the tool rotates. The rotation is also associated with the heat input in the FSW process. The rotation has a direct relation to heat generation, so if the rotation increases the heat input will increase too.

The tool down force: This force is necessary to maintain the position of the tool and to ensure the contact with shoulder maintaining the material below the surface. The contact between the tool and the workpieces contributes to the welding process by adding heat generated by friction.

The tool traversing force: This is an output variable and corresponds to the opposing force in the tool movement during the welding process. This force has a parallel direction to the movement and depends on the parameters employed and the temperature during the joining process.

The tool side force: This is the force perpendicular to the down and traversing forces. The side force is generated by the unsymmetrical characteristics of the FSW process.

The spindle torque: This is the torque necessary to maintain the tool rotation. This torque depends on the down force and the friction generated in the contact area. In addition, it also depends on the material flow around the probe.

The tool temperature: This temperature is usually used for monitoring the actual joint temperature at the process. Normally this temperature is taken by a thermocouple near to the tool's shoulder that represents only part of the real tool-material temperature.

3.6 Energy in the FSW

The energy consumption of processes, like FSW or other welding techniques are difficult to evaluate, because all the parameters have to be taken into account. One way to measure the consumption was described in the work of Shrivastava et al. (2015b), where energy for aluminum alloys (7075-T6 and 6061-T6) welding were analyzed. These analyses included the energy from the start of the spindle motor to the end of all process movement. However, it is necessary to consider the pre-process and post-process for a better analysis.

One advantage of the FSW process is the low energy consumption in relation to the conventional joint by fusion techniques like Gas Metal Arc Welding (GMAW), Gas Tungsten Arc Welding (GTAW), Shield Metal Arc Welding (SMAW). In a recent study, Shrivastava et al. (2015a) compared the energy consumption in the pre-processing, processing and post-processing of the FSW to GMAW, and concluded that the energy used in the FSW is 40% less than the GMAW for a 6060 T6 aluminum alloy. They established that the reason for this is because the FSW doesn't exceed the solidus temperature of the alloy. The FSW process is considered as a solid-state nature using less energy. The authors also evaluated the environmental impact emissions in all the processes and concluded that the FSW produced 31% fewer greenhouse emissions than GMAW, which constitutes another advantage of the FSW technique.

3.7 Imperfections and Defects in a FSW joint

The imperfections, flaws, and defects can be defined as was described by Threadgill (2007). The author stablish that there is often confusion between terminology such as imperfections, flaws or defects, and suggest to follow the definitions given by ASME B31. The author said "ASME defines an "imperfection" in terms of departure of a quality characteristic from its intended condition and a "flaw" as "an imperfection ... detectable by NDE". A "defect" is defined as "a flaw ... of such size, shape, orientation location or properties as to be rejectable"...". For the purpose of this thesis, the formulated detection system will consider imperfections that were verified only by microscope and not by NDE. It is important to say these imperfections could represent flaws or even defects because of the side and geometries that they have but it will be considered here as imperfection. The following section presents the common types of flaws or defects in the FSW process

The FSW process has two classes of usual defects related to the geometric aspects of the tool and material, and these are related to material flow around the tool. The most common defects associated with geometric aspect are described in the following.

Lack of joining: This defect occurs when there is an improper alignment of the tool related to the abutting edges of the workpieces (KAH ET AL., 2015).

Lack of penetration: This occurs when the tool's probe is too short making that the bottom side of the weld does not accomplish a full junction.

The most common defects associated with the material flow are presented as follows.

Void (Volumetric flaw): It is known also as wormhole defects. The void is an empty space (hole) inside the weld that continues in the longitudinal direction of the weld. The defect is caused by low heat input, also known as Cold Weld, and appears usually when there is a low relation between the tool rotation speed and the traversing speed values.

Surface lack of fill: It is a longitudinal crack defect on the top surface of the welding. This crack is often related to a high heat input and usually appears when there is a high relation between the tool rotation speed and the traversing speed values.

Excessive flash: This defect occurs when the tool position is too deep, causing a high down force. As a result, the material will be pushed to the edge of the weld. This defect is also associated with the excessive heat generation that makes softer the boundary between the surface material and the tool shoulder. This defect reduces the strength because it also reduces the thickness of the plate.

Onion-rings: The Onion-rings are structures that can be seen as bands in the weld nuggets. The Onion-ring structures have these distinguished dark and bright bands, and the

distance between the bands is the same to the forward motion of the tool in one revolution of the tool. These bands have a subsequent role in the formation of crack paths in the weld nugget under cyclical loading when the process temperature increases significantly (KAH ET AL., 2015).

3.8 Nondestructive examination

The Non-Destructive Examination (NDE) is normally necessary for detection of defects that could affect the joint. There are multiple methods to detect defects in FSW welding joint, but the most usual methods used are the X-Ray radiography test and ultrasonic tests (Immerse Ultrasonic test or Phase Array Ultrasonic test).

X-Ray radiography: The X-ray Radiography test can be executed utilizing two options, X-rays or gamma rays, both of electromagnetic radiation. These rays have the ability to penetrate, travel through and exit, in diverse materials because of the short wavelength they have. In fact, the X and gamma rays have the shortest wavelength of the electromagnetic spectrum, which permits to test materials as carbon steel and other metals.

Immerse Ultrasonic Test: This NDE technique permits to detect and evaluate cracks, dimensional measurements and material characterization. Other ultrasonic techniques use a probe (normally piezoelectric transducer) to emit an ultrasonic beam in a liquid, normally water, as an ultrasonic couplant. This means that the transducer is not in a direct contact with the material. During the test, the material and the transducer face are immersed in the tank. This system is multi-purpose ultrasonic testing equipment, featuring a large immersion tank and a computer controlled precision device with three axis motion for scanning.

Phase Array Ultrasonic: It is a nondestructive testing method that has as principal applications to find flaws in manufactured materials such as joint welds. In this case, the probe contains small ultrasonic transducers that can be pulsed independently. The modifications in the timing of these elements are in a sequence, one by one along the row, forming a pattern of constructive interference resulting in a beam at a set angle. This also means that the beam can be focused and steered electronically. The beam is swept through the object being tested, and finally, a visual image from the data processed is shown by using the multiple beams of the sample. The terms phased and array refers to the timing of the pulse and the multiple elements, respectively (ASTM, 2014).

In the work of Ferlin (2012), the authors developed a method to detect defects during FSW using the vibration frequency spectrum. For this purpose, the vibration signals of the two plates during the process were measured by three accelerometers. The data were pro-

cessed using Fourier Fast Transform and the wavelet transform, comparing and describing what happened in bad or in a good weld. The accelerometers were in three different places. One in the fixation bar and the other two were placed on each plate to be weld. Only one accelerometer was able to detect all the failures that occurred during the process. After the spectral analysis, it was possible to detect and locate failures using the two alternatives, FFT analysis and wavelet transform.

Boldsaikhan et al. (2011a) show that with a frequency spectrum analysis of the traversing and side forces it is possible to determine relevant information on the weld quality. The previous work and other authors like Arbegast (2003), Schmidt and Hattel (2005), Chen et al. (2006) and Schneider and Nunes (2004), explain the variation of these forces with the following hypothesis:

"As the moving weld tool advances along the weld path, a small cavity opens up at the trailing face of the probe. During the initial stage of the cavity formation, a stress barrier holds a shear layer of material from entering into the cavity. However, while the cavity size increases, the stress barrier decreases. As soon as the cavity size reaches a critical value, the shear layer of material is released, and fills the opened cavity. This "pulsating" process then repeats itself, with the void opening and filling process repeated as the tool rotates and advances. For aluminum friction stir welding at relatively high advance per revolution, this "pulsating" process is assumed to happen in every single rotation of the weld tool."

On the other hand, other works like Burford et al. (2012) and Boldsaikhan and McCoy (2013), have established the effect of the material flow on the tool forces during the FSW processing. Based on the information recorded in an AA2024-T23 butt weld joint, they developed a 2D heuristic model of the traversing and side forces harmonic oscillation. The model was developed using pseudo shear concept, obtaining a similar result to the actual weld force process. Finally, two scenarios were simulated, a good and a bad weld. Using the frequency spectrum analysis, the similarities with the real process were shown. They concluded that when the joint is perfectly performed, the frequency spectrum of these two forces will only show a peak in the spindle frequency. However, the bad welding shows frequency peaks not only in the spindle frequency but in the other frequency due to the more irregular and unstable material flow during the process.

The same authors suggest a method (BOLDSAIKHAN ET AL., 2011b) to relate these frequencies with wormhole (cavity) diameter using an artificial neural network (ANN). Using an AA7075-T73, they made a butt weld recording the forces at 68.2 Hz in a 3 seconds segment. In their paper, it was shown that the relationship between the void diameter and the low-frequency side force is nonlinear.

The main difference of their method with this thesis is the used of the spectral temporal analyzed multiple signals by using the Short-Time Fourier Transform to detect imperfections patterns. This analysis was made for plates of aluminum alloy 5052-H32, in a butt-welding configuration. The down force, the traversing force, the side force, and the torque were included for the spectral analyses during the process and under different condition of tool rotating speed, traversing speed, and depth penetration. These permitted to design a system fuzzy logic monitoring for detection of imperfections during the process involving all four parameters analyzed.

4 Methodology and Experimental Setup

In this thesis, we apply some tools of computational intelligence technology using a FSW process machine to detect the imperfection during the process. For this, an ANN dynamic model of the process was used. The main phases of this research are described in the following.

First, it was necessary to know the FSW limits using its operational parameters. In this case, the rotational speed, the traversing speed and the penetration depth of the weld were the considered parameters. Some tests with different configurations to produce bad and good welding were conducted. In consequence, a design of experiment was required to cover a range of parameters and combinations. These data were first evaluated by using an Analysis of Variance (ANOVA) to determine the relevant effects that could modify significantly the process outputs and to evaluate the nonlinear behavior. The response of this experiment was then used to train the ANN model. The responses of the experiment were the axial force, the spindle torque and tool temperature to do the dynamic analysis of this process. The results contributed to the imperfection detection by using the frequency spectrum of the tool forces (down, traversing and side forces) and the spindle torque using a fuzzy logic system.

At the same time, an additional data acquisition (DAQ) system was implemented for the measurements because of the sample rate, used by the machine's control system, was not appropriate to allow an accurate spectrum analysis. The DAQ permitted measurements with high sample rates for the forces sensors and for the spindle torque, so the spectrum analysis could cover a wide range of frequencies. This also permitted to see how the frequency was modified during the time, generating the spectrogram. Using the values of these results, a fuzzy logic system was developed to establish if there is a failure in the joint or not.

Once the experimental analysis was done, an ANN model was developed. Different configurations of ANN models were tested to try a better performance. It was also necessary to evaluate the model to verify its performance in terms of prevision. The performance of the model was validated with a testing to replicate the real condition. The model also helps to understand the dynamic of the process.

Normally, the imperfections in the joints were inspected by cutting some samples to make macrography analysis, allowing verifying the predicted results of spectrum analysis. The voids in the joint are an indication of a bad weld. In figure 4.1, the scheme of the methodology is shown.

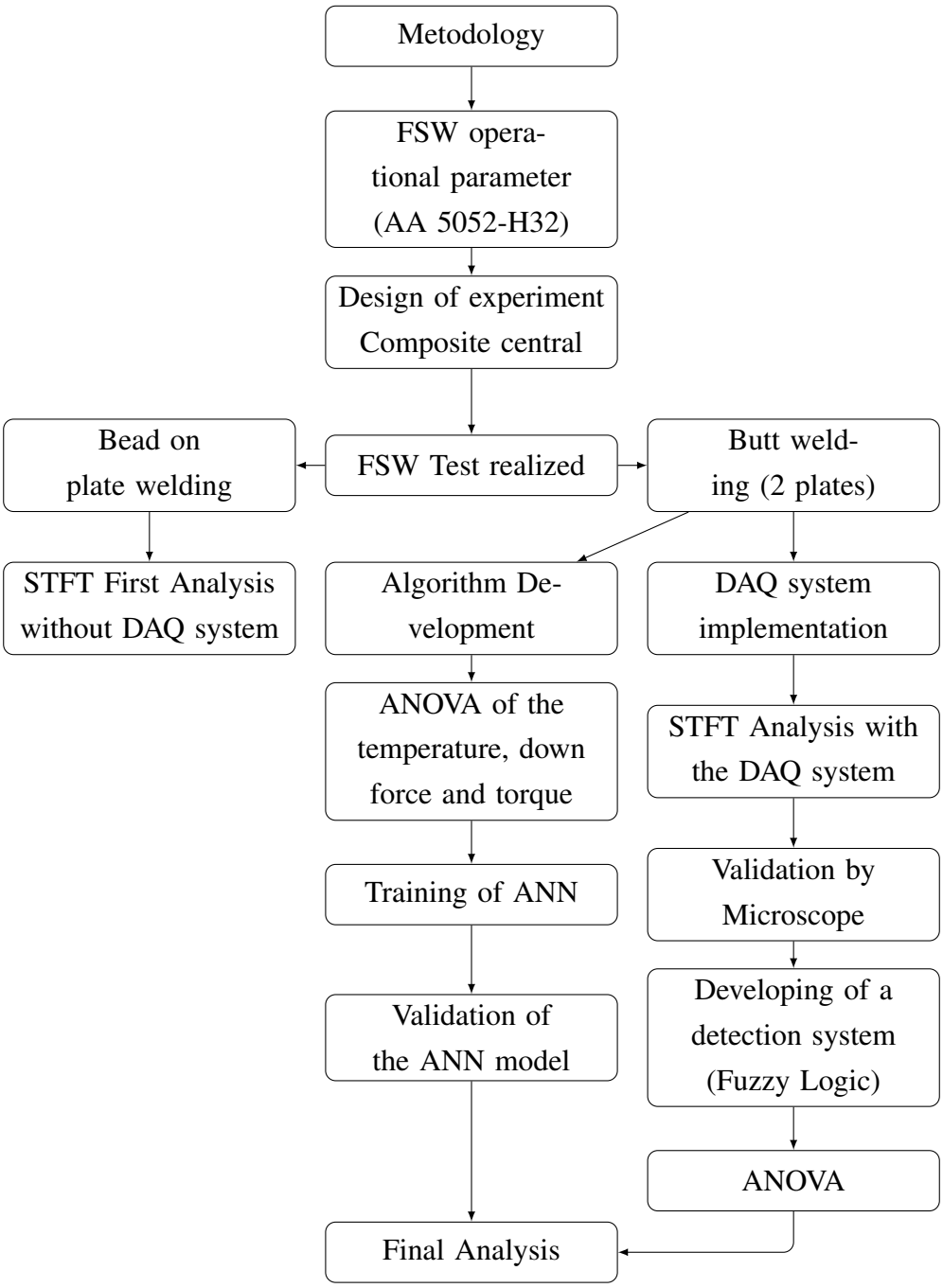

Figure 4.1: Schematic description of the methodology used for this thesis.

In the following section, it is described the specification of the welding machine, the DAQ system, the materials used, the experimental setup and the design of the experiment.

The experiment details are also presented to ensure its replication for future researches.

4.1 Research Equipment

4.1.1 Friction Stir Welding Machine

The equipment used for welding is the SAPNC, RM1 model of Manufacturing Technology, Inc, available in the LNNANO (National Nanotechnology Laboratory) in Campinas, São Paulo, Brazil. This equipment is shown in Figure 4.2. This machine is able to weld ferrous and non-ferrous alloys.

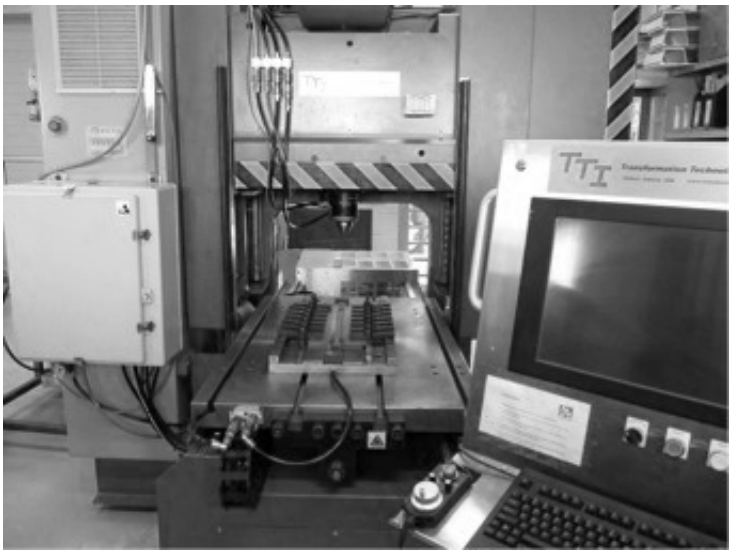

Figure 4.2: FSW Machine SAPNC, RM1 of Manufacturing Technology.

The spindle is driven by a 27 kW YASKAWA servo motor with a range of 5000 rpm. It has also a belt ratio 2:1 with the spindle tool. The spindle tool position is also controlled with servo motors in all axes and a maximum travel of 700 mm in X, 300 mm in Y, 400 mm in Z according to the axis in Figure 3.1. The control system consists of a Rockwell Programmable Logic Controller (PLC) with a human-machine interface (HMI) connected to force sensors, encoders, and YASKAWA servo motors. This permits multiple types of control loops in this system. This machine can be controlled by the tool position, force, power, and the tool temperature (available only for high fusion temperature alloys). The force sensors measure them in all orthogonal axes with a maximum load of 22 kN for axis X and Y, 80 kN for Z. The torque is evaluated by the measurement of the current used by the motor. The

system also measures the tool temperature using a thermocouple type K, which is linked to a wireless device installed in the tool holder. A rooter receives the signal of the measurement, which is sending to the PLC for monitoring its value.

4.1.2 DAQ system

Although the welding machine has a good instrumented control system, there are some limitations. One of them is the sample rate that the weld machine used, 10 Hz that is not enough to show a wide spectrum range in frequency for all studied variables. With this frequency, the spectral analyses will only allow a 0 Hz to 5 Hz range (Nyquist frequency limit). In most cases, this range is below the spindle frequency that is used as a reference in comparison to the lateral forces peaks.

For this reason, a Data Acquisition system was implemented using the sensors signals, increasing the sample rate to 100 Hz and allowing the spectral analyses range between 0 Hz to 50 Hz. The system allows analyses above the spindle frequency. The equipment used is an i100 model Instrunet data acquisition system. The DAQ has 44 screw terminals, 16 are voltage input channels, 8 voltage output channels and 8 digital I/O. Figure 4.3 illustrates the DAQ system used in this research.

Figure 4.3: Instrunet DAQ system used in this research.

This system registers the forces sensors and the spindle torque. In that form, the spectral analyses of these variables are possible. The measurements were taken in parallel to the controller measurements. Figure 4.4 illustrates the scheme of the DAQ system implemented in the FSW machine.

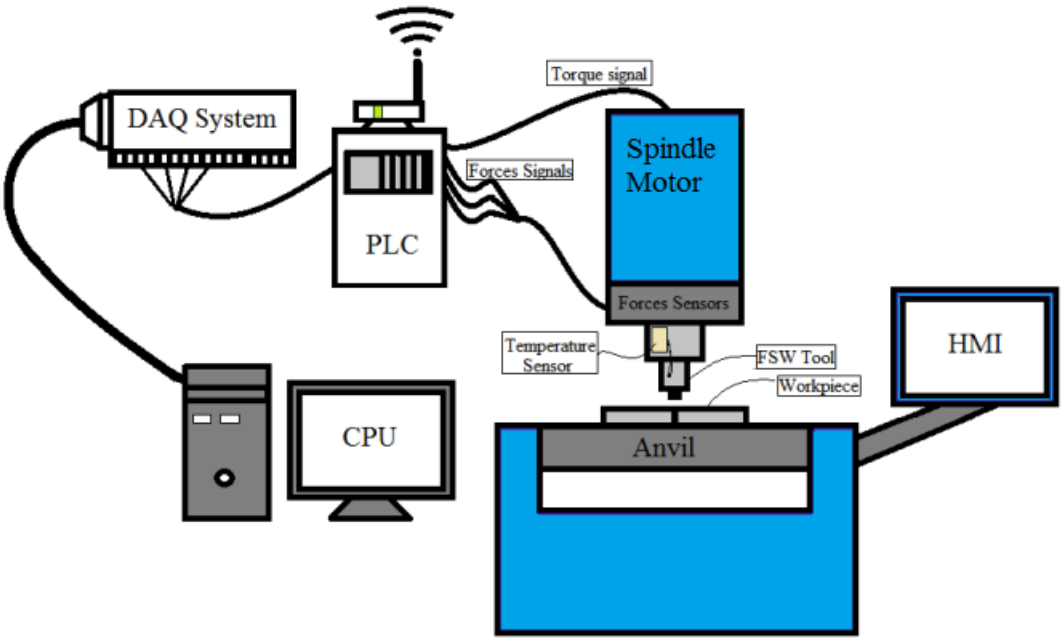

Figure 4.4: Scheme of the FSW Machine with the DAQ system.

The DAQ system records the tool forces and spindle torque signals at 100 samples per second. All the signals are in voltage, so the DAQ and the sensors were connected to the Programmable Logic Controller (PLC) connections. A computer (CPU) records all data during the process. The PLC saves all data including the tool temperature for a different sample rate, which are 10 samples per second.

4.2 Material and test

4.2.1 Material: 5052-H32 Aluminum

The material used for this research was the aluminum alloy AA5052-H32 alloy. This aluminum has the magnesium and chrome as its principal components. The full weight composition is 97.3% Al, 0.155% Cr, 0.0046% Cu, 0.216% Fe, 2.21% Mg, 0.0381% Mn, 0.0706% Si and 0.001% Zn. The AA5052 has a reasonably high strength and is hardenable only by cold working in a significant degree, allowing a series of "H" tempers. The H32 means that the alloy is hardened by cold work.

This is an aluminum alloy nonhardenable by heat treatment and is commercially available in flat roll coils, plates and sheets. This material has used in a wide range of environments due to excellent corrosion resistance, especially in salt water. Although it loses some strength

in the range of 200 to 250 °C, this alloy increases its strength under subzero temperature, making it ideal for low-temperature applications. The AA5052 alloy has many industrial applications due to its corrosion resistance and the strength in the low temperature and it is used in food processing, small marine ships, fuel cabinets, hydraulic tubes, home freezers, industrial and marine flooring, trailers and tool boxes.

On the other hand, the microstructure of AA5052-H32 aluminum alloy sheet substrate material showed a characteristic of a material conformed by a laminating mechanism showing an anisotropic array of elongated grains aligned in the rolling direction (RD) and a morphology of deformed grains in the normal direction (ND) of the plate with the presence of constitutive intermetallic particles with "fish-eye" shape possibly Al3Mg2 or Al8Mg5 (GALVIS PEREZ, 2016).

Figure 4.5 show the micrographs obtained by optical microscopy of the materials used in this thesis in the condition as received. The rolling direction (RD), traversing direction (TD), normal direction (ND) and direction of deposition (DD) are shown in the image below.

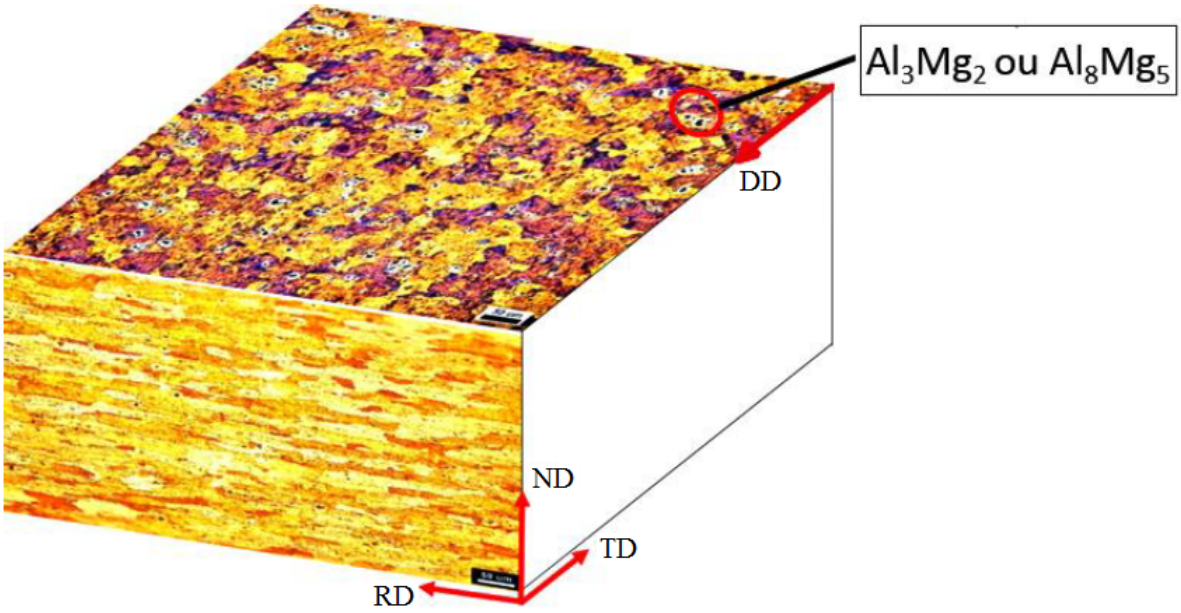

Figure 4.5: Microstructure of the AA5052-H32 (GALVIS PEREZ, 2016).

4.2.2 Test plates and FSW Tool

The workpieces consist of two plates with 150 mm by 75 mm by 2.5 mm each of aluminum AA5052-H32. In this case, a butt joint welding configuration was used for this

research. During the butt welding, the tool penetrates the joint line between the two plates with a controlled position and it moves with a constant traverse speed until it completes a specific length, in this case, 100 mm, as it is shown in Figure 4.6. For every sample the encoder data were recorded including the data of the tool spindle, the tool forces, the torque, and the tool shoulder temperature.

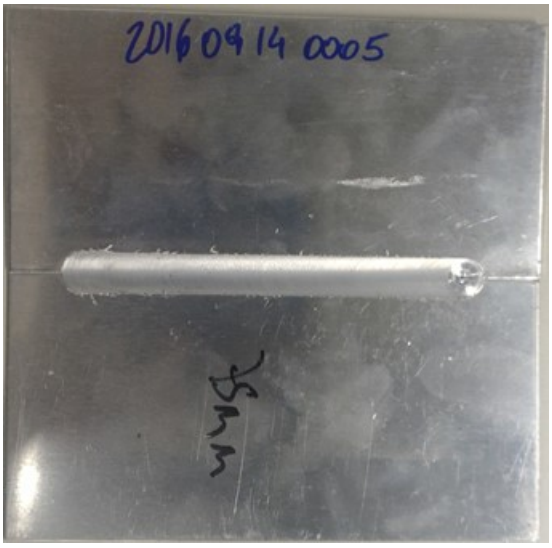

Figure 4.6: Welding plates sample used in the processing by FSW.

The FSW tool, used in this test, was made of H13 tool steel and it has a circular cylinder probe with 5 mm diameter, 15 mm in the shoulder diameter, and 2.4 mm of probe longitude. This tool is refrigerated by a cool holder system and it is has a temperature sensor in the tool's shoulder near to the base of the pin. Figure 4.7 illustrates the tool used. For this research, a thermocouple type K was used to measure the temperature.

Figure 4.7: Tool use in the FSW process.

4.3 Experimental Parameters used

The experiment used a range of parameters in order to obtain experimental data to supply the training process of an ANN. These combinations of operational parameters produce imperfections as a consequence of the wide range. The parameters levels used in the experiment are presented in Table 4.1.

Table 4.1: Process inputs for the experiment

Levels	d_p (mm)	ω (rpm)	ν (mm/min)
Low	2.1	400	75
High	2.4	600	125
Center	2.25	500	100
star point 1	1.95	500	100
star point 2	2.25	300	100
star point 3	2.25	500	50
star point 4	2.45	500	100
star point 5	2.25	700	100
star point 6	2.25	500	150

These inputs parameters are the tool rotation ω, the traverse speed ν and the penetration depth d_p. With the purpose to obtain the effect of every input of the process, a central composite design with two samples experiment was run. The central composite design (CCD) consists of a 2^k factorial design, with a low and a high level per every input factor, testing every permutation. This part of the CCD provides the data for estimating each factor first-order effect and interactions between the input factors. The complementary points of the CCD, or star points consist of $2k+1$ points, providing data for estimating second-order effects. Figure 4.8 represents all configurations used during the experiment, including the star points that make part of the star design. It can be seen that, for each factor in the design, the star points represent new extreme values (low and high) (NATRELLA, 2010). Outputs for this FSW process experiment were the tool axial force, the spindle torque and tool temperature. These results were used to build the ANN structure.

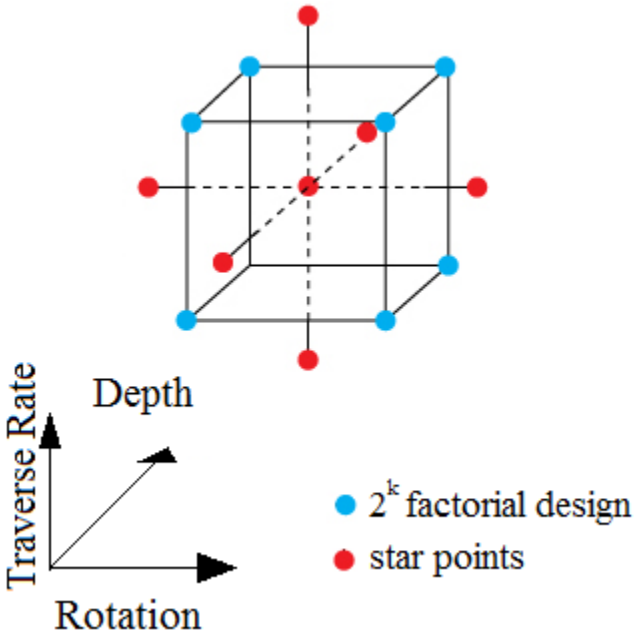

Figure 4.8: Composite Central design for the experiment.

4.4 Experimental Limitation

Due to the thickness of the plates, the backing, which supports the workpieces, must be checked to verify its flatness. The non-flatness can cause deformation on the plate altering the penetration of the tool, causing to loose the reference to the tool position. The process response can be altered significantly because of this reason.

Another limitation of the experiment is the tool temperature measurement. This variable was measured by a thermocouple positioned in the tool, in a hole that leads to the shoulder surface in contact with the workpiece. The contact of the thermocouple with the tool and the respective variation in its position may affect the measurement. Additionally, the temperature measurement may be affected by the entrance of material in this zone causing deviation.

4.5 Experimental Analysis

For this experiment, an Analysis of Variance (ANOVA) (MONTGOMERY, 2008) was conducted to determine the major effects of every input in outputs. Responses analyzed by the ANOVA were the average value of the tool axial force, temperature and the spindle torque during the joint stage. To do this, the residual Square sum (Sq sum), the degree of freedom (d.f.), the mean squares (Mean Sq), the F distribution and the p-value of each factor and its

interaction (relation with other parameters) were calculated. Also, the mean square error was calculated.

Using the p-value of each factor and its interaction, we can analyzed if a specific factor has a major effect on the response or not. The p-value is defined as the significance value of a factor. If the p-value is less or equal than the significant level of the experiment (p-value ≤ 0.05 for example), a high significance effect is identified. In the work, the ANOVA was made with a significant level of 5% to ensure accurate analysis. Table 4.2 shows the results of the ANOVA performed using the statistics analysis software called DESIGN EXPERT 10 (ANDERSON AND WHITCOMB, 2015).

Table 4.2: Axial Force ANOVA

Source	Sq sum	d.f.	Mean Sq	F	p-value
d_p	18920000	1	18920000	226.3	$<$0.0001
ω	4411000	1	4411000	52.76	$<$0.0001
ν	73688.13	1	73688.13	0.88	0.3585
$d_p\ \omega$	5466.08	1	5466.08	0.065	0.8007
$d_p\ \nu$	12530.6	1	12530.6	0.15	0.7026
$\omega\ \nu$	405500	1	405500	4.85	0.0389
d_p^2	869200	1	869200	13.6	0.0016
ω^2	405200	1	405200	4.85	0.039
ν^2	54305.98	1	54305.98	0.65	0.4293
Error	1756000	21	1756000		
Total	26250000	30			

It is possible to verify that the penetration depth and the rotational speed affect the axial force significantly (p-value < 0.0001), and this result is in accordance with a previous research described in (DAVIS ET AL., 2011). The ANOVA results also establishes that the rotational speed and the traverse speed interaction term ($\omega\nu$ term) is also relevant (p-value=0.0389 ≤ 0.05). We can also verify that the depth and the rotational speed pure quadratic terms (d_p^2 and ω^2) are significant (p-values of 0.0016 and 0.039 respectively), which also confirms a nonlinear relation between these variables. These results evidence the nonlinear relation between the inputs and the axial forces.

In addition, it was also verified that the penetration depth and the rotational speed had

also a highly significant influence effect in the variation of the torque, presented in the Table 4.3 (p-value < 0.0001). This is expected due to the physical relation existing between them (ROSS AND SORENSEN, 2013). In this case, the quadratic components were not significant (p-value > 0.05).

Table 4.3: Spindle Torque ANOVA

Source	Sq sum	d.f.	Mean Sq	F	p-value
d_p	682.14	1	682.14	109.89	$<$0.0001
ω	190.13	1	190.13	30.63	$<$0.0001
ν	12.69	1	12.69	2.04	0.1676
$d_p\ \omega$	11.57	1	11.57	0.01	0.1865
$d_p\ \nu$	3.21	1	3.21	0.52	0.4801
$\omega\ \nu$	8.06	1	8.06	0.64	0.431
d_p^2	13.35	1	13.35	2.15	0.1573
ω^2	9.11	1	9.11	1.47	0.2391
ν^2	7.19	1	7.19	1.16	0.2939
Error	130.35	21	6.21		
Total	1091.93	30			

Finally, ANOVA results for the temperature are reported in the Table 4.4. It is possible to observe that the depth and rotational speed also affect significantly the tool temperature (p-value ≤ 0.0001). The traverse speed is also significant with a p-value=0.0022. From the evaluation of the quadratic terms, the ANOVA reveals that the depth pure quadratic term (d^2) is significant (p-value=0.017$<$0.05). The changes of the rotational speed and the depth influences the tool axial force, the tool temperature and the spindle torque the most. Although the traverse speed influences also the tool force with a nonlinear term and the tool temperature, it doesn't affect the spindle torque.

Table 4.4: Tool Temperature ANOVA

Source	Sq sum	d.f.	Mean Sq	F	p-value
d_p	44128.71	1	44128.71	105.68	$<$0.0001
ω	21432.98	1	21432.98	51.33	$<$0.0001
ν	5050.47	1	5050.47	12.1	0.0022
$d_p\ \omega$	32.93	1	32.93	0.079	0.7816
$d_p\ \nu$	51.26	1	51.26	0.12	0.7295
$\omega\ \nu$	47.84	1	47.84	0.11	0.7383
d_p^2	2804.96	1	2804.96	6.72	0.017
ω^2	41.3	1	41.3	0.099	0.7563
ν^2	40.56	1	40.56	0.097	0.7584
Error	8768.79	21	417.56		
Total	80748.77	30			

In summary, the rotational speed and the depth influence the axial force, the temperature and the spindle torque. The traverse speed influences also the axial force and the temperature with a nonlinear term, but it does not affect the spindle torque. For the dynamic model, it will be considered the three inputs (rotational speed, traverse speed and penetration depth) in order to predict the three output responses (axial force, spindle torque and tool temperature). These results were used to build the ANN structure.

The same experimental design was also used for a spectral analysis of the response. The objective of this experiment was to determine spectral patterns that indicate imperfections during the FSW process. These patterns were analyzed by using the STFT and the fuzzy logic system considering a time-varying frequency analysis.

5 Results and Discussions

5.1 Artificial neural networks structure and training parameters

The three principal inputs of the process (tool rotation speed, traversing speed and penetration depth) were controlled in order to obtain the outputs (the tool down force, the tool temperature and the spindle torque). The idea is to take into account all the effects of inputs and training the ANN with all the data of the design of experiment expecting the model to be precise. The inputs and outputs were concatenated in series with all data recorded. All signals were taken at a sample frequency of 10 Hz, which is normally used by the welding machine controller.

Focused on the actual process, the ANN uses the experimental data, evaluates the ANN predicted results and minimize the error by modifying the weights and biases values. In this case, the minimization process was done by the Levenberg-Marquardt training algorithm (NØRGÅRD ET AL., 2000), that usually uses the mean square error between the model results and the real data. Some modification in the training procedure was implemented in order to minimize the model error as described as follows.

Subsequently, it was necessary to scale all the data because of the difference in scale of the inputs and outputs. This scaling of the data was necessary, preventing a variable to be more dominating than others. For this purpose a maximum and minimum normalization according to the following equations were applied:

$$\overline{y}_i = \frac{y_i - y_{min}}{y_{max} - y_{min}} \tag{5.1}$$

$$\overline{x}_i = \frac{x_i - x_{min}}{x_{max} - x_{min}} \tag{5.2}$$

where y_{min} is the minimum value of the respective output, y_{max} is the maximum value of the respective output, x_{min} is the maximum value of the respective input and x_{max} is the maximum value of the respective input.

After the data is scaled, it is necessary to initialize the weights and biases for the training algorithm. The Levenberg-Marquardt algorithm normally begins with some random weights and biases in every layer. In order to reduce the computational time of the training process, the weights and biases were initialized using the Nguyen-Widrow algorithm (NGUYEN AND WIDROW, 1990). This algorithm finds the initial weights and biases located in the activated regions of the neurons reducing the training time. However, this algorithm has a limitation that it can not be initialized with activation function defined in the $(-\infty, \infty)$ interval. The

structure suggested, in this case, satisfies this condition, since the hidden layer and the output layers have the sigmoid function as the activation function. The Bayesian training modification and the initialization algorithm used in this work are part of the MATLAB neural network toolbox (DEMUTH AND BEALE, 1993). In addition, the ANN training requires two data sets, the training and the testing sets, which are data sets for training the model and to test the ANN performance. In this case, the training set is compounded of 85% of the data and the test set is 15% of all data, both chosen randomly.

Finally, the number of neurons in the hidden layers and the delays were found by testing some configurations. The structure of the ANN has three inputs including the hidden layer with 27 neurons and the output layer with three neurons. All the ANN inputs are completed with 10 time-shifts of the inputs and outputs. It was verified for the data used in this work that if it is considered less than five neurons with the same time-shift, then the model response deviate more from the real value. If the number of neurons is more than 27 with the same number of time-shifts, the training time increases and there is no significant difference in the response obtained with 27 neurons. This also happened when the time-shifts were more than 10.

5.2 Simulation model and experimental validation

Once the ANN was trained, analysis and simulation tests are necessary to verify the performance of the model. First, the model is analyzed using the same data used for training the ANN using a recurrent structure. The NARX structure was used because the activation functions are nonlinear function (sigmoid function). Figure 5.1 shows the experimental data compared with the NARX model output.

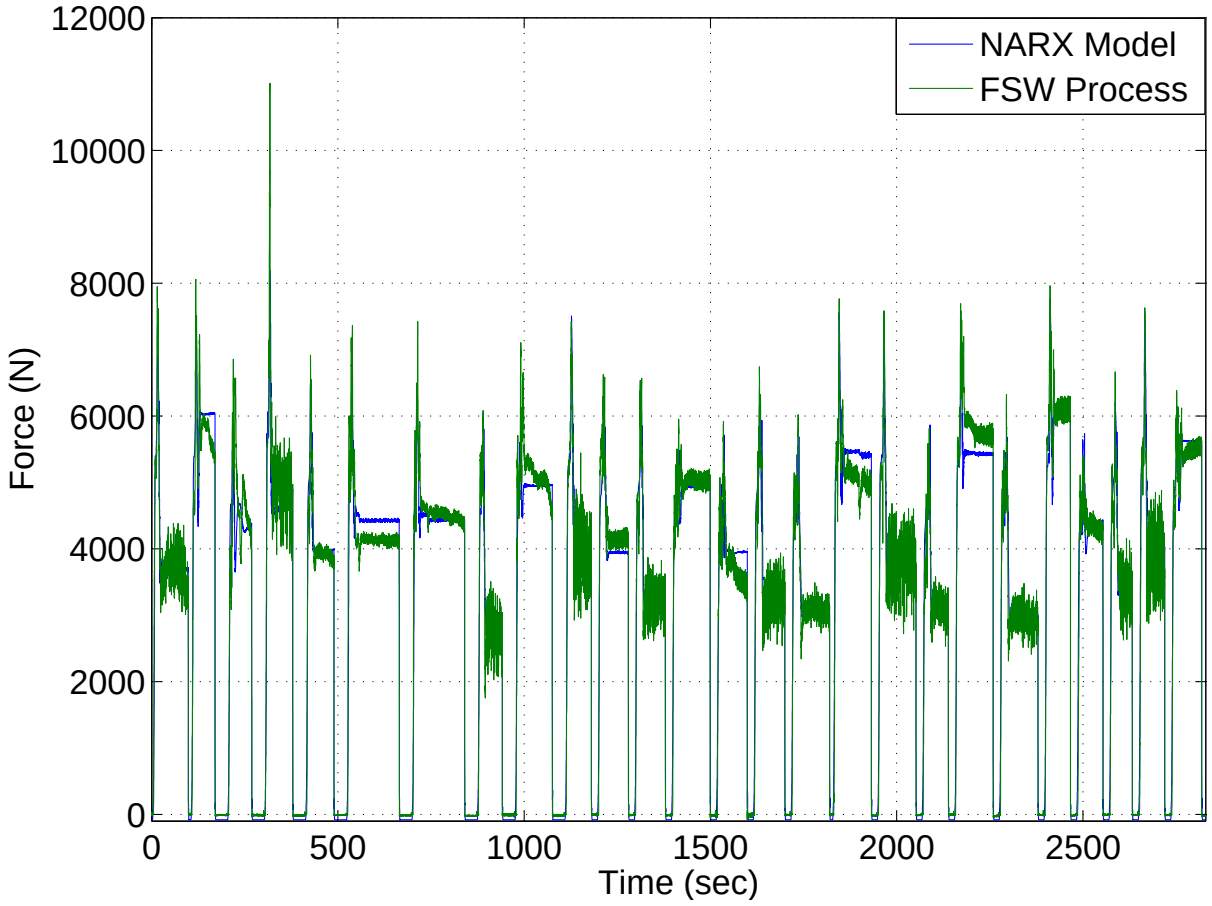

Figure 5.1: Comparison between the response of the down force NARX model prediction and the experimental data (FSW process) during all test.

The Figure 5.1 contains the variation of the down force signal response for all tested configurations in the FSW process. It is possible to verify that the model result has a few outline points. These points occur when the tool lift off the work-piece which causes abrupt force and torque changes. This figure also shows that some parts of the model have a little deviation from the experimental data.

In order to have a validation with the training data, a regression analysis between the target (all experimental data) of the ANN and the model output was conducted. The model has a correlation coefficient of 0.99255 for the training set, which means that the prediction of the model can be considered close to the training data. The Figure 5.2 shows a comparison between the experimental data and the model response, and the respective correlation coefficient. The analysis was made with the three outputs data training set.

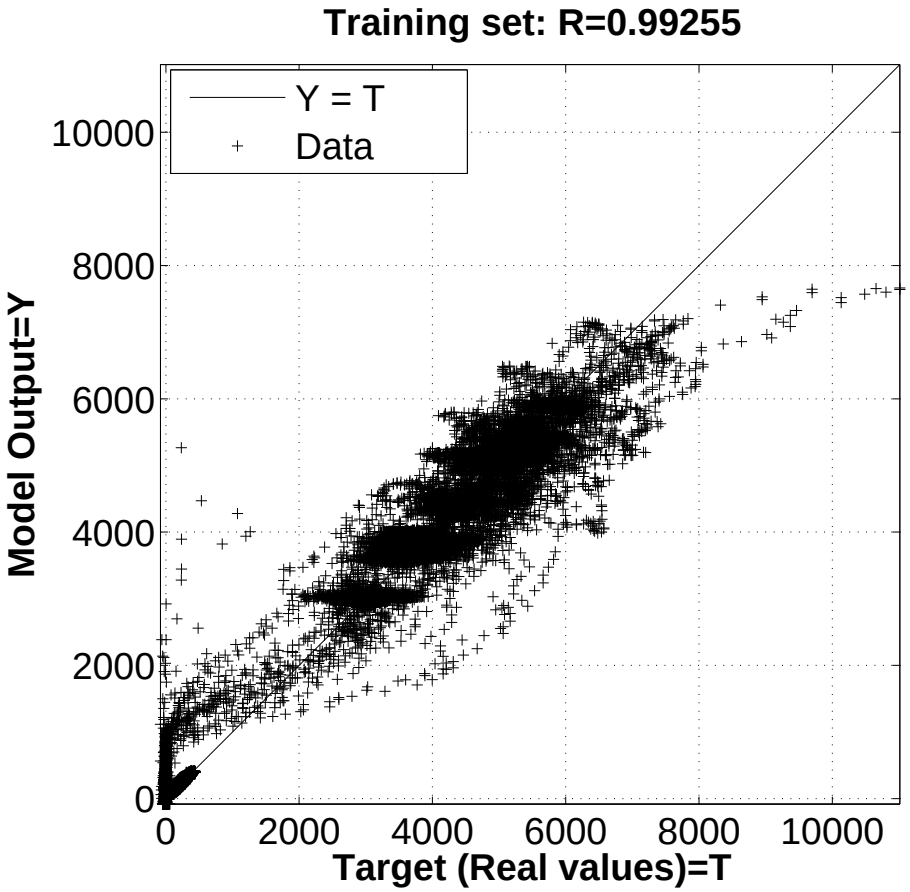

Figure 5.2: Artificial neural network model correlation with experimental training set (down force, torque and tool temperature response).

In the same way, an analysis was made with the test set. In this case, a correlation coefficient of 0.99241 was obtained, which demonstrates a good performance. The model results are close to the experimental data. The correlation is illustrated in the Figure 5.3. The analysis was conducted considering the three concatenated inputs and the three concatenated outputs.

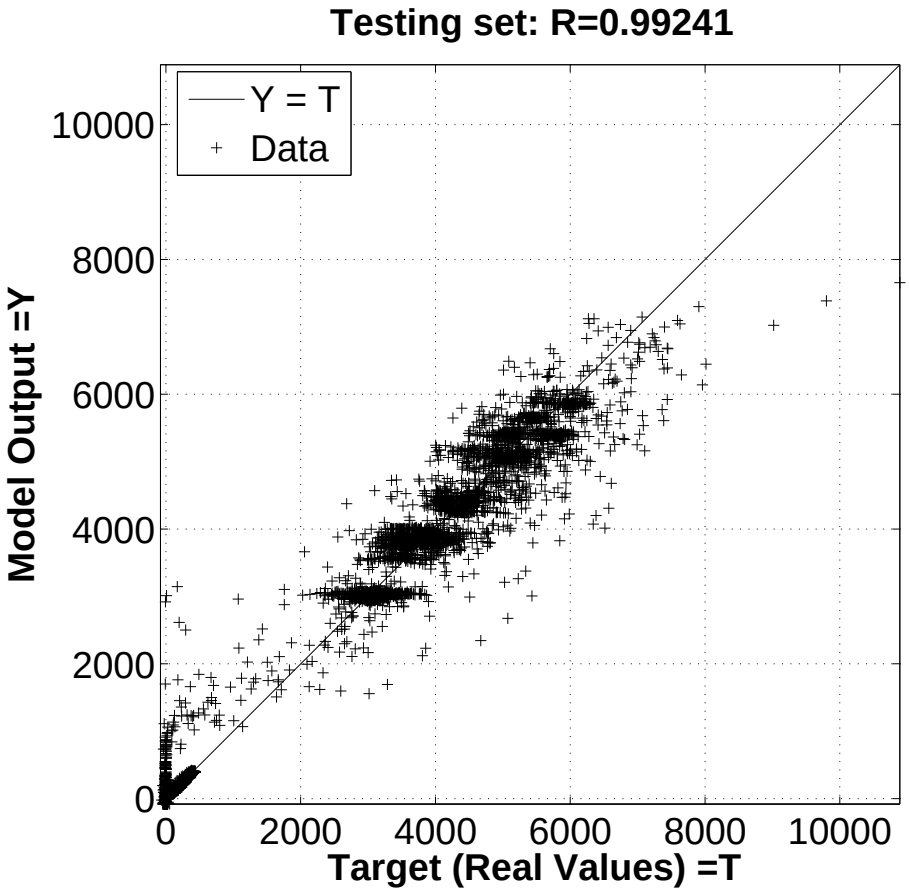

Figure 5.3: Artificial neural network result and correlation with experimental testing set (down force, torque and tool temperature response).

Finally, the ANN was simulated with a different experimental input condition and then was compared to the model response to see how close the simulated results were from the real response. This procedure was executed with data that were not used in the training. For this test, the model received unknown input data (ν = 100 mm/min, ω = 700 rpm and d_p = 2.25 mm) and as a response, the model presented the dynamic response of the force, the torque and the temperature. Subsequently, the model response was compared with the real dynamic response, showing a similar response. Real process signals of force, torque and temperature of the ANN model prediction are presented in the Figure 5.4. The figure shows a good prediction with low error and only with a few missing points.

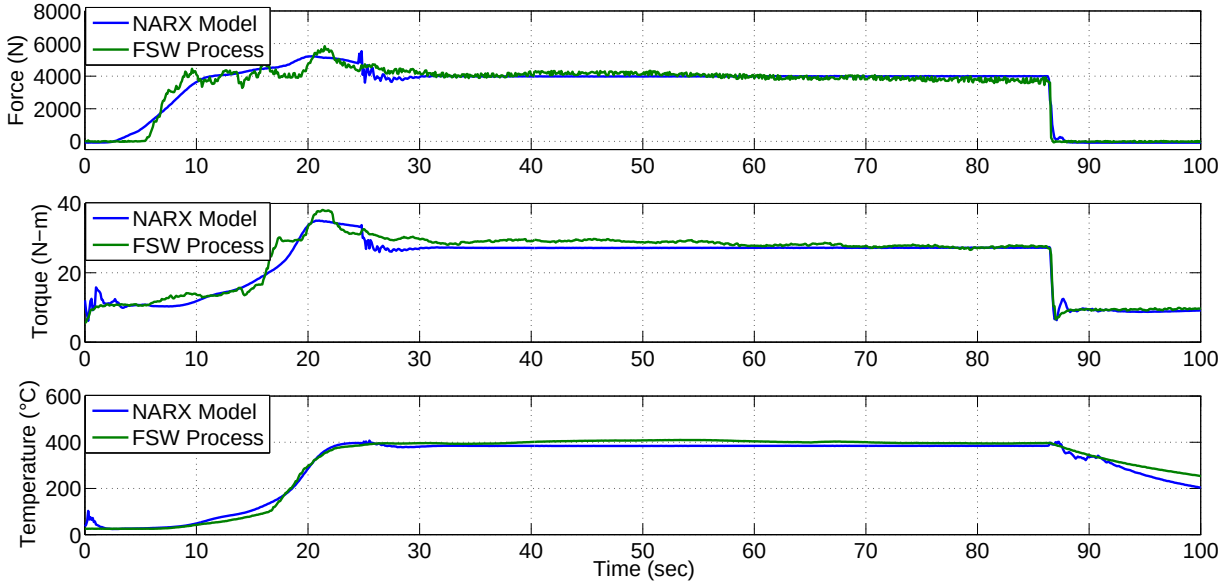

Figure 5.4: Comparison between the response of the output ANN model and the experimental data for ν = 100 mm/min, ω = 700 rpm and d_p = 2.25 mm.

Despise the results of the model, the outputs like the traversing force and the side force were difficult to analyze and to model, especially when the process presented an irregular behavior (for example in surface flaws cavities). Additionally, there are not clear imperfection patterns in the time domain.

5.3 Preliminary test using the STFT (Spectral analysis)

The first attempts were to determinate the operation region and also try to differentiate signal patterns and its spectrum. These first attempts were done only with the weld machine instrumentation system. As explained before, this is a limitation that could affect the final result in the spectrum. During these welding tests, the tool penetrates a plate within a controlled position and it moves with a constant traversing speed until it completes a specific length, in this case, 60 mm. This procedure is also called as bead-on-plate welding. For this test, it was only analyzed the side and traversing forces. Figure 5.5 shows the plate used for this test.

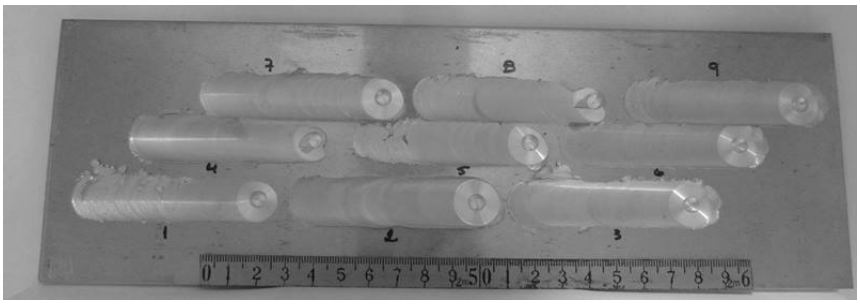

Figure 5.5: Plates used for the preliminar tests.

5.3.1 Example of a good weld

The operational parameters, rotational speed ω, traversing speed ν and penetration depth d_p, were changed to find a good behavior in the welding process. In these tests, visual inspection was made to detect the imperfection after the welding process was finished. Figure 5.6 shows a sample with a good quality aspect. This sample was made using the following parameters: ω = 500 rpm, ν = 125 mm/min and d_p = 2.1 mm.

Figure 5.6: Example of a good welding.

As it was seen before, the side and the traversing forces are important to identify a process imperfection. Figure 5.7 illustrates the forces responses (time variation) during the process. F_x is the traversing force and F_y is the side force.

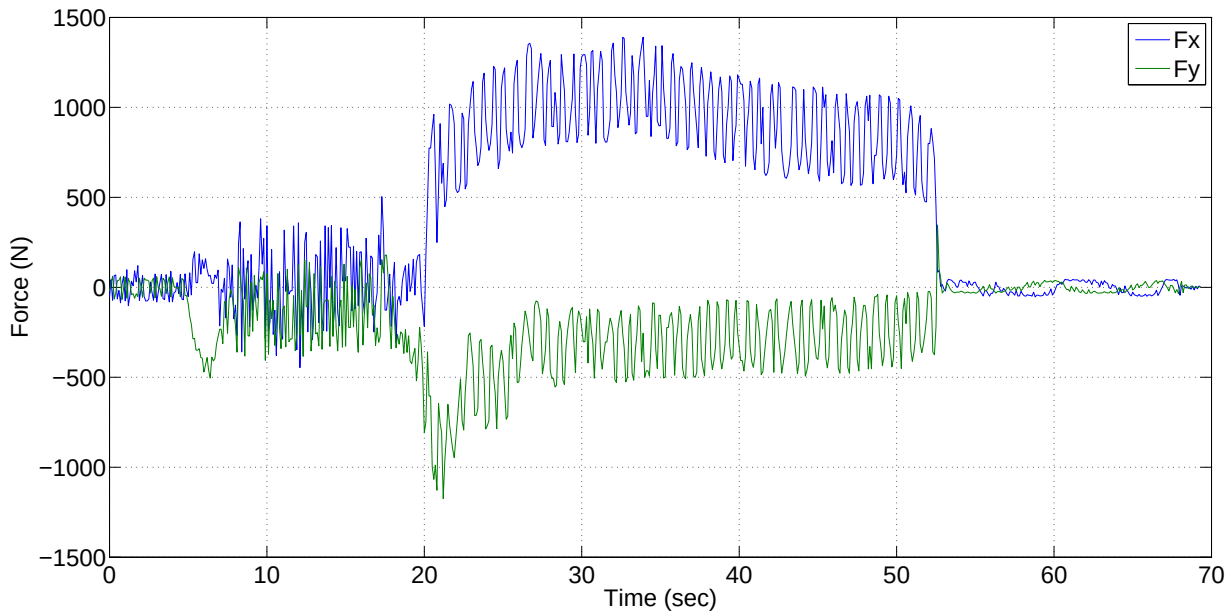

Figure 5.7: Forces for a sample with a welding of good quality.

Figure 5.7 shows that the side and the traversing force response have oscillatory response in the joint phase of the process. The spectrum of these signals are represented in figures 5.8 and 5.9. The spectrograms have a rectangular window of 5 seconds with 50% overlap and a sample rate of 10 Hz. This permits a spectral analysis until 5 Hz (Nyquist frequency) to avoid the aliasing effect. The lateral color bar indicates the intensity of the components. The signals were similar and have higher amplitude in the 1.5 Hz showing a pattern of the signal in that frequency. This is an indication of a stable welding condition.

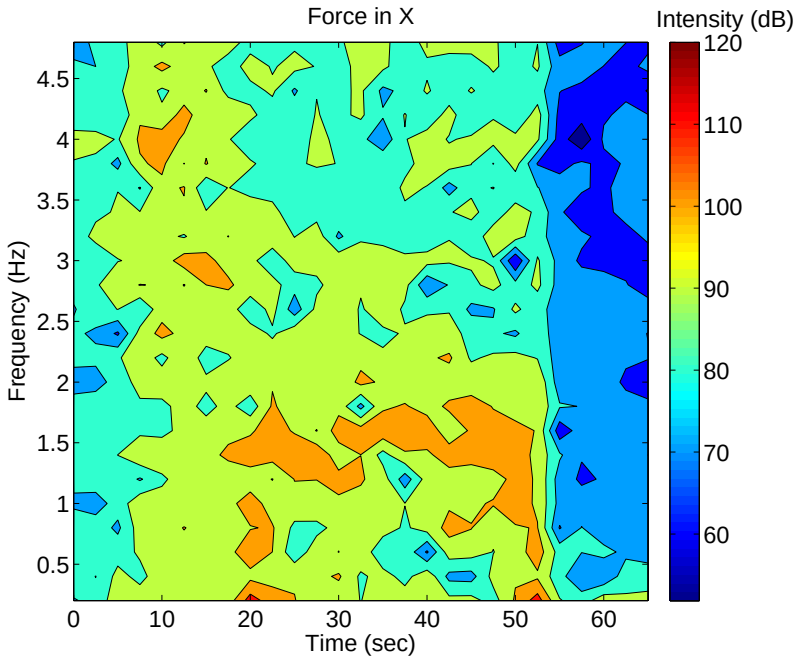

Figure 5.8: Force F_x spectrogram with a good welding process.

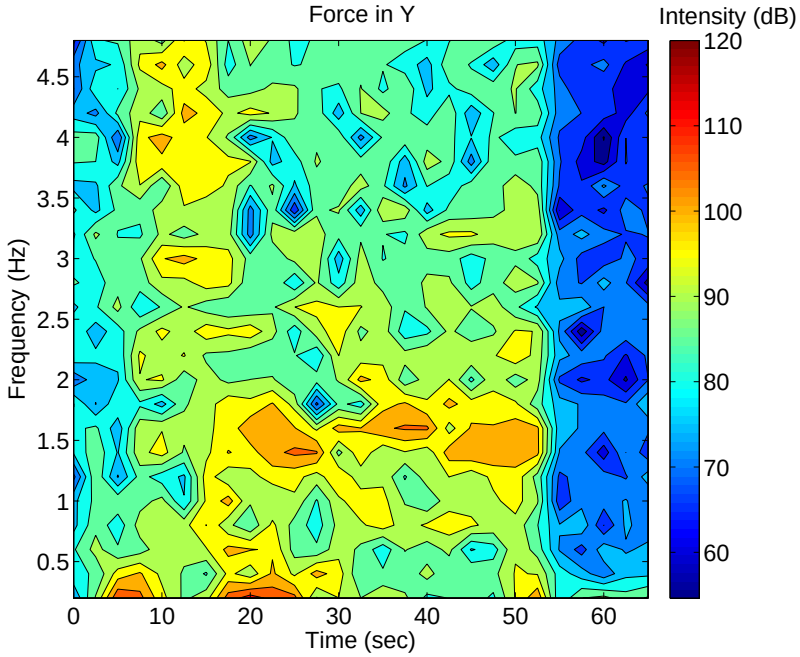

Figure 5.9: Force F_y spectrogram for a good welding process.

5.3.2 Example of a bad weld

In contrast, Figure 5.10 shows a process that does not have a good quality aspect. This sample has an irregular response in the parameters of the process.

Figure 5.10: Example of a bad welding.

This sample was made using the following parameters: ω = 400 rpm, ν = 125 mm/min and d_p = 2.1 mm. The rotational speed was modified when compared to the previous case. Figure 5.11 shows the response of the traversing force F_x and side force F_y.

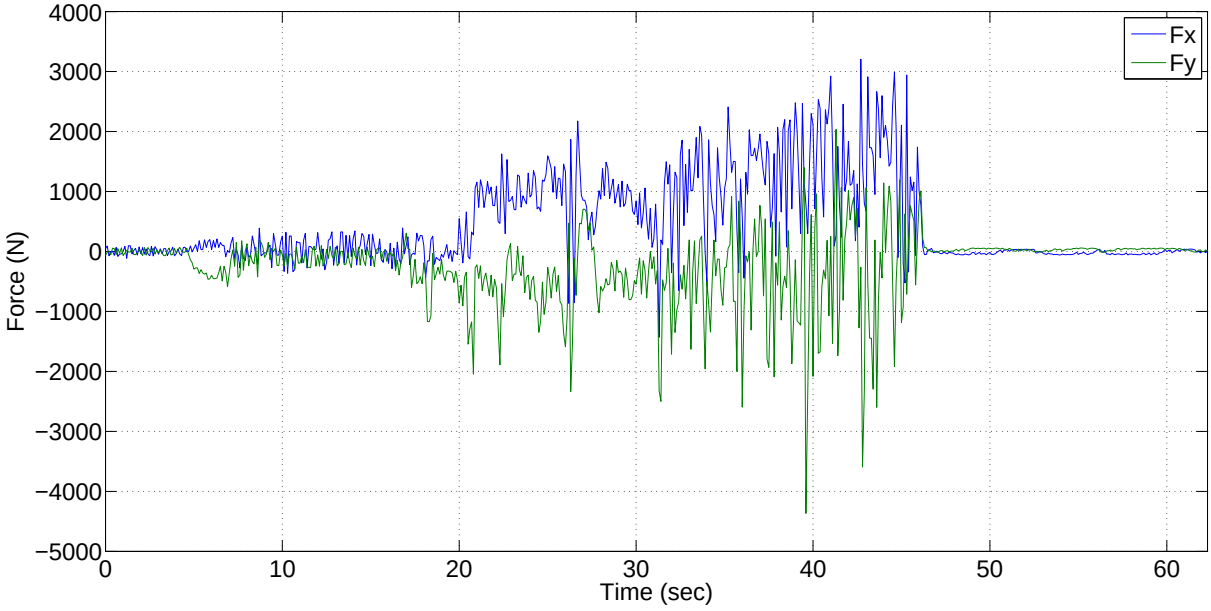

Figure 5.11: Forces for a sample with a welding of bad quality.

It can be seen the forces are noisy and without any aspect of a harmonic pattern. As a consequence, the spectrum shows a great alteration in almost all frequencies analyzed. In figures 5.12 and 5.13 the spectrogram of the F_x and F_y are illustrated.

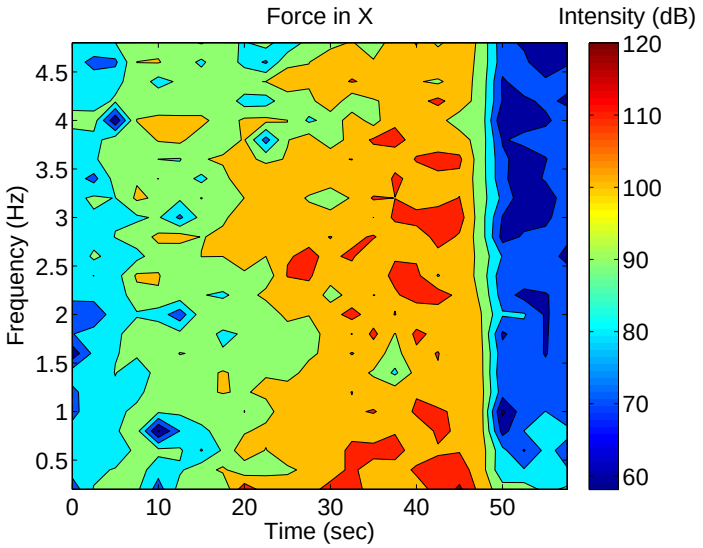

Figure 5.12: Force F_x spectrogram for a bad welding process.

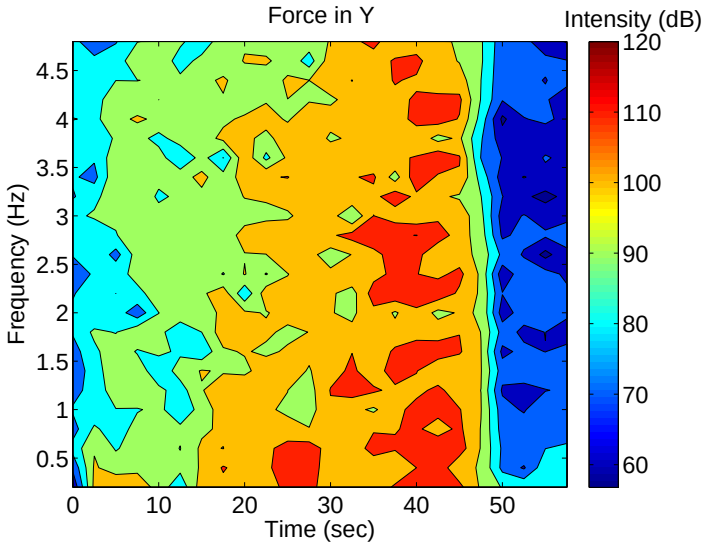

Figure 5.13: Force F_y spectrogram for a bad welding process.

5.3.3 Comments about good and bad welding

Both forces signal and spectrograms show a noise signal that explains the aspect of the sample. Clearly, the signals for both samples were different. The second signal is more irregular, which is the principal characteristic of the bad flow of material around the probe. Also,

as a difference with the first sample signals, no pattern is visible in the second sample signal. From the spectrum, it is seen that the components in the second sample are higher in intensity and have components in the lower frequency (below 1 Hz), which was pointed out by some authors as an indicator of an imperfection in the weld (BOLDSAIKHAN ET AL.; BARAKA ET AL., 2011b; 2015). In addition, there were peaks in all frequencies, which express again the nonuniform signal caused by poor stability achieved during the process in this particular sample.

The authors Boldsaikhan et al. (2011b) and Baraka et al. (2015) also described that, in the case of the traversing and side forces, it is expected a single peak in the rotation frequency during the FSW process. Due to the spam of frequency analyzed (less than 5 Hz), it was not possible to see that pattern. This justifies the importance of using a small sample time and the DAQ system. It is also important the visualization of the results using a logarithm scale because of the wide range of values resulting from the STFT.

5.4 STFT for the FSW process

Once a range of operational parameters was established, an experiment that explores all the range observing the spectrum of all tool forces and the spindle torque was conducted. As described in Chapter 4, the test was made with a butt welding configuration. For these tests, the DAQ system was used. As was explained before, this system permits a greater sample rate. In this case, all the variables were sampled at 100 Hz. The spectrograms were made with a rectangular window with 2 seconds and an overlap of 50%. As an example, it is shown in this document six welding samples whose spectrogram indicates imperfections (one good and five bad). The first two cases are the examples of a good and a bad welding. These two cases also help to know the interval of the intensity values for the fuzzy membership functions (high and low). The other four cases were analyzed under the microscope, by cutting the transversal sections of the welding and checking the spectrograms in this specific section to verify the imperfection occurrence.

5.4.1 Case 1: ω = 500 rpm, ν= 100 mm/min, d_p = 2.45 mm

This welding corresponds to ω = 500 rpm, ν= 100 mm/min and d_p = 2.45 mm, and this is an example of a good welding. The welding plates of Case 1 are shown in Figure 5.14.

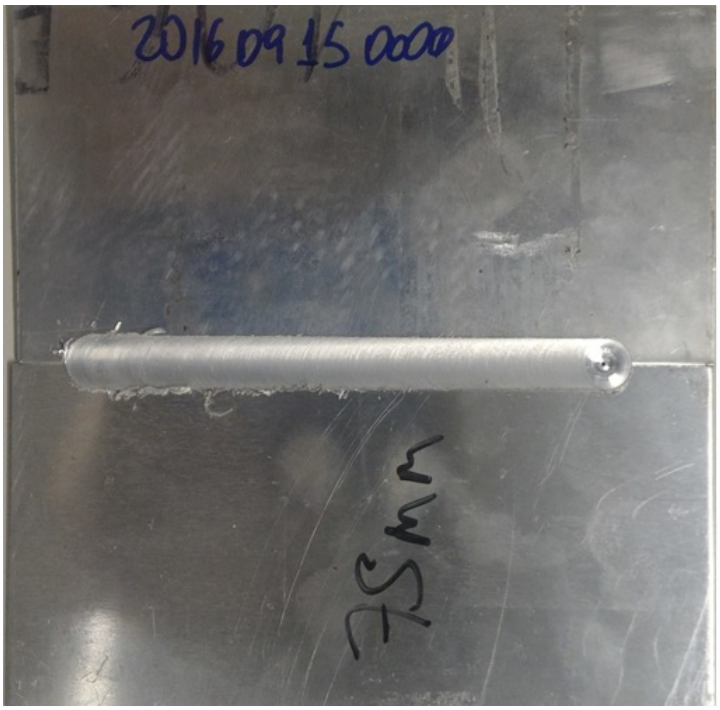

Figure 5.14: Welded plates of Case 1.

Using the traversing force signal and the STFT, the spectrogram is shown in Figure 5.15. The spectrogram was divided into the main stages of welding (plunging, dwelling, welding, and lift off). The intensity was set in dB. The figure does not present peaks in the low-frequency range. The figure only has a peak with maximum intensity (greater than 125 dB) in the rotating frequency of the tool (8.33 Hz).

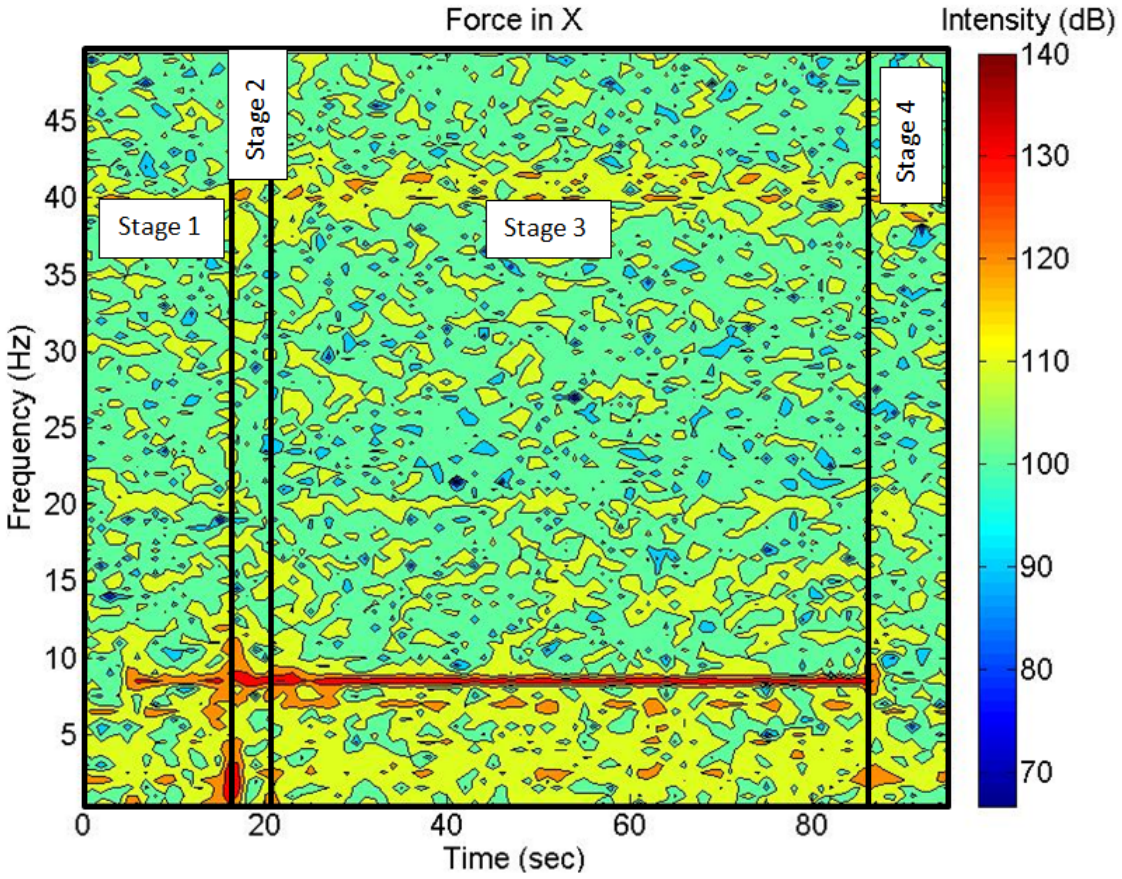

Figure 5.15: Force F_x spectrogram of Case 1.

Figure 5.15 is the spectrogram of the side force resulting from the previous welding, divided into the steps of welding. This welding has a good behavior. The figure does not have peaks in the low-frequency range. The figure only has a peak with maximum intensity (greater than 125 dB) in the rotating frequency of the tool (8.33 Hz).

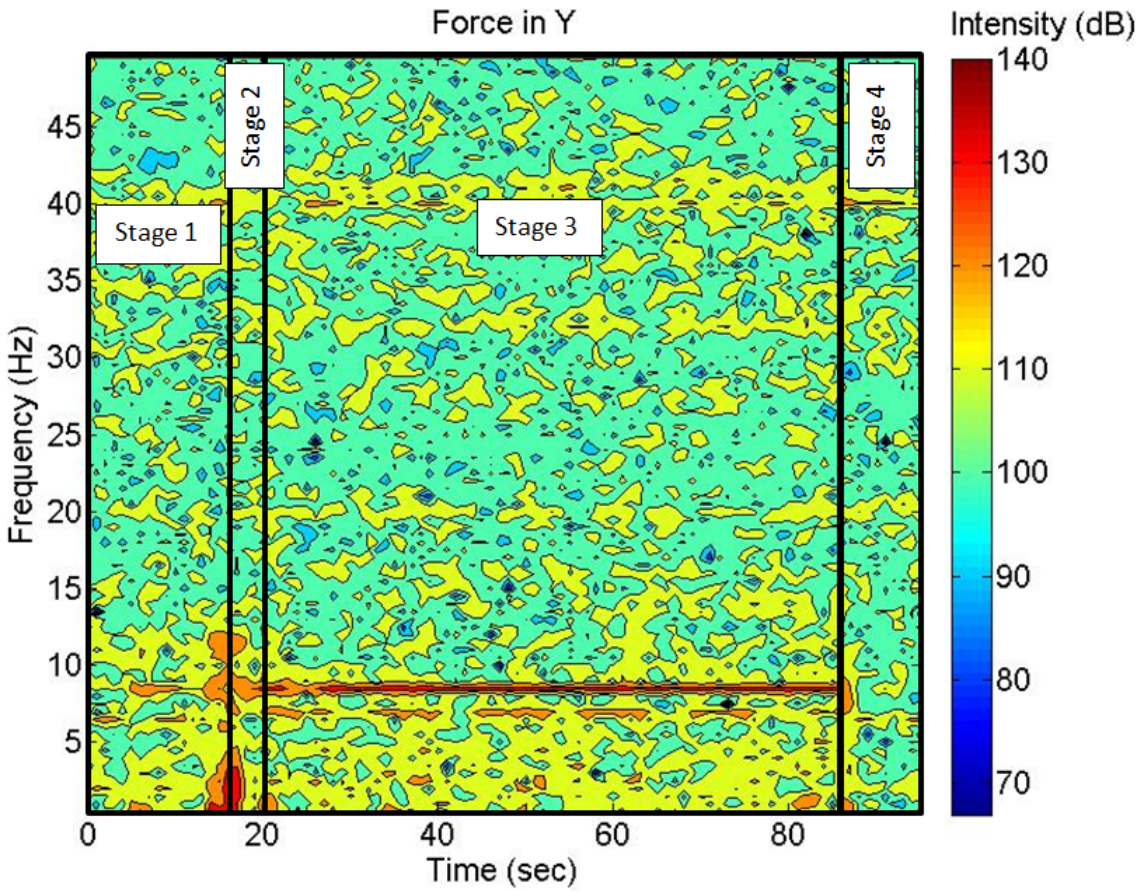

Figure 5.16: Force F_y spectrogram of Case 1.

Figure 5.17 is the down force spectrogram resulting from the previous welding, divided into the four welding stages (plunging, dwelling, welding and lift off respectively). The figure does not have peaks in the low frequency range. The figure only has peaks with maximum intensity (greater than 140 dB) at the beginning of the welding when the tool penetrates. A intensity peak is also present at the lift-off of the tool.

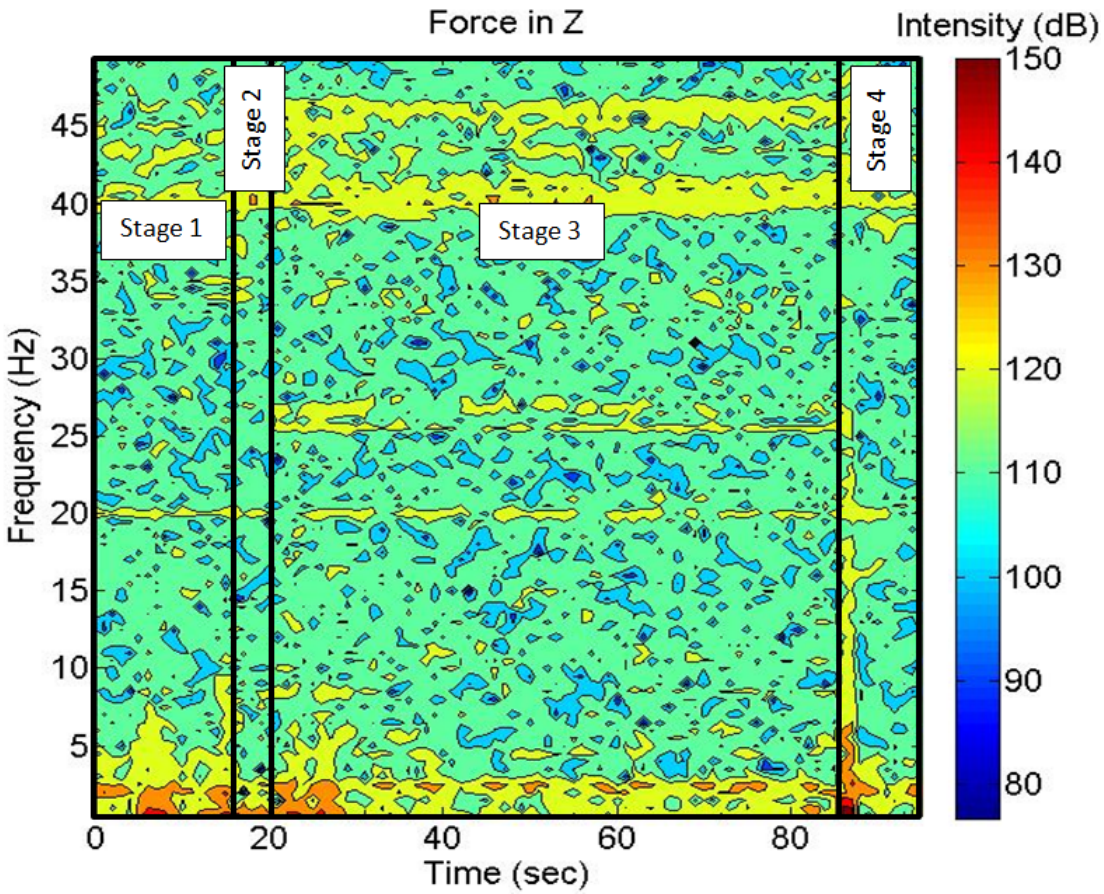

Figure 5.17: Force F_z spectrogram of Case 1.

Figure 5.18 is the spectrogram of the torque of the tool resulting from the previous welding, divided into the steps of the welding. The figure does not have peaks in the low frequency range. The figure only has peaks with maximum intensity (greater than 80 dB) at the beginning of the welding when the tool penetrates. At the lift off of the tool also has a high intensity peak.

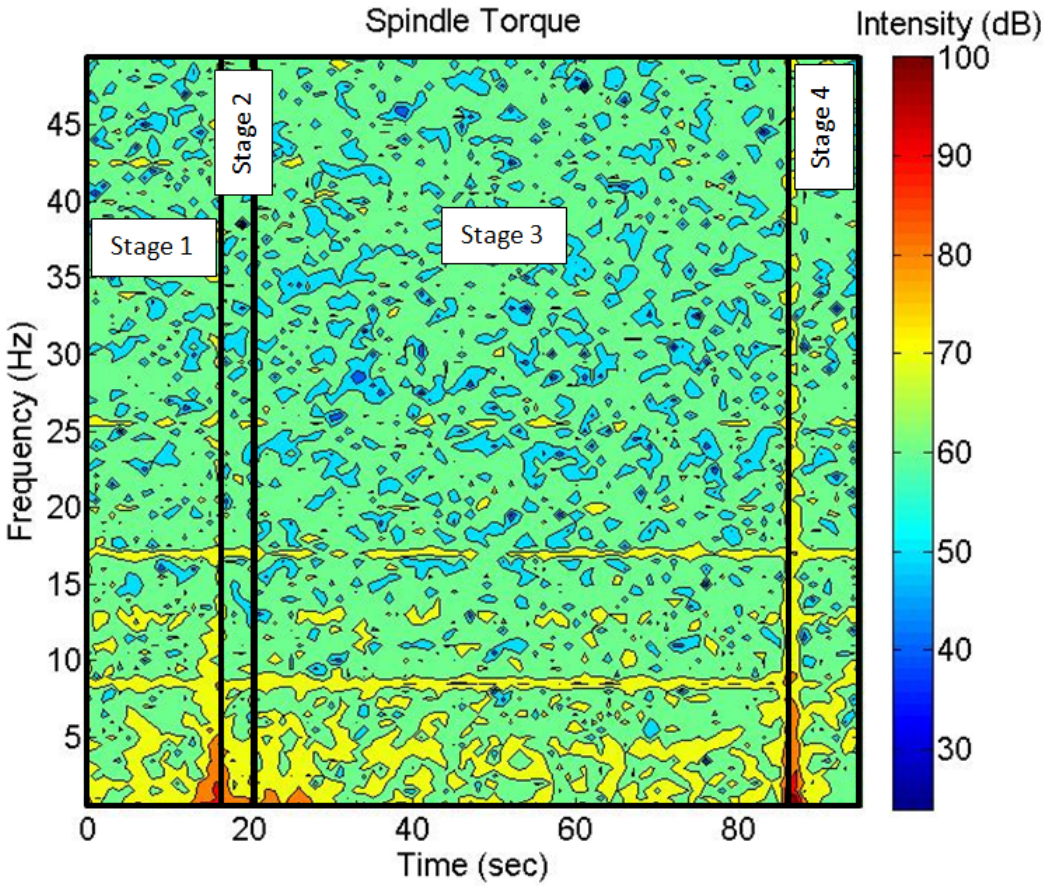

Figure 5.18: Spindle torque spectrogram of Case 1.

5.4.2 Case 2: ω = 400 rpm, ν= 125 mm/min, d_p = 2.1 mm

This welding was done with ω = 400 rpm, ν= 125 mm/min and d_p = 2.1 mm, and this is an example of a bad welding. The welding plates of the case 2 is shown in Figure 5.19. It can be seen that there are cavities and irregularity in the surface.

Figure 5.19: Welded plates of Case 2.

Using the STFT of the traversing force signal, a spectrogram was obtained as it is illustrated in Figure 5.20. The spectrogram was divided into the four stages of the welding. The spectrogram shows many peaks in the low-frequency range with maximum intensity (greater than 125 dB). These peaks are distributed throughout the welding stage, below the rotating frequency of the tool. Spikes in the rotating frequency of the tool (6.67 Hz) are also present.

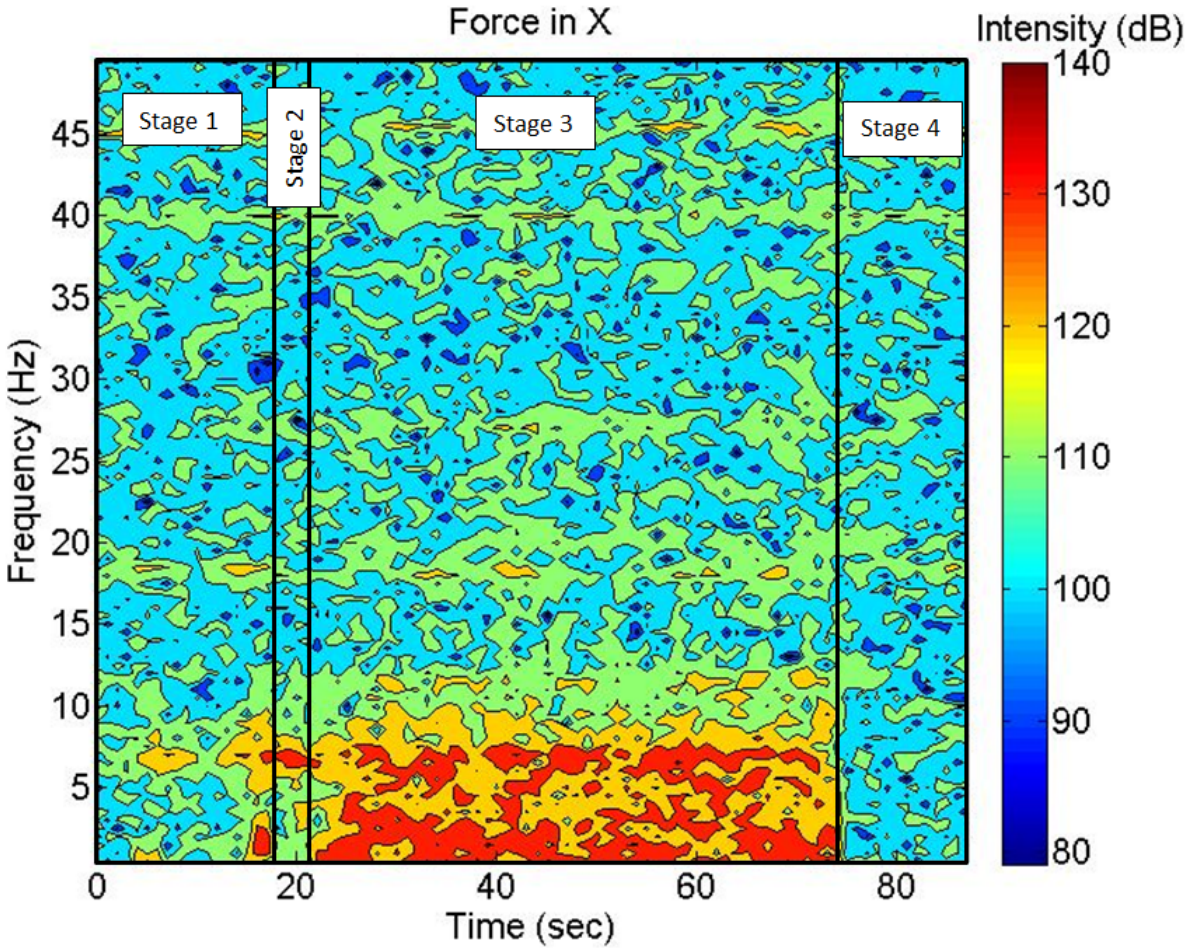

Figure 5.20: Force F_x spectrogram of Case 2.

Figure 5.21 is the spectrogram of the side force resulting from the previous welding, divided into the steps of welding. The spectrogram show many peaks in the low-frequency range with maximum intensity (greater than 125 dB). These peaks are distributed throughout welding stage, below the rotating frequency of the tool. The peaks in the rotating frequency of the tool (6.67 Hz) are also present.

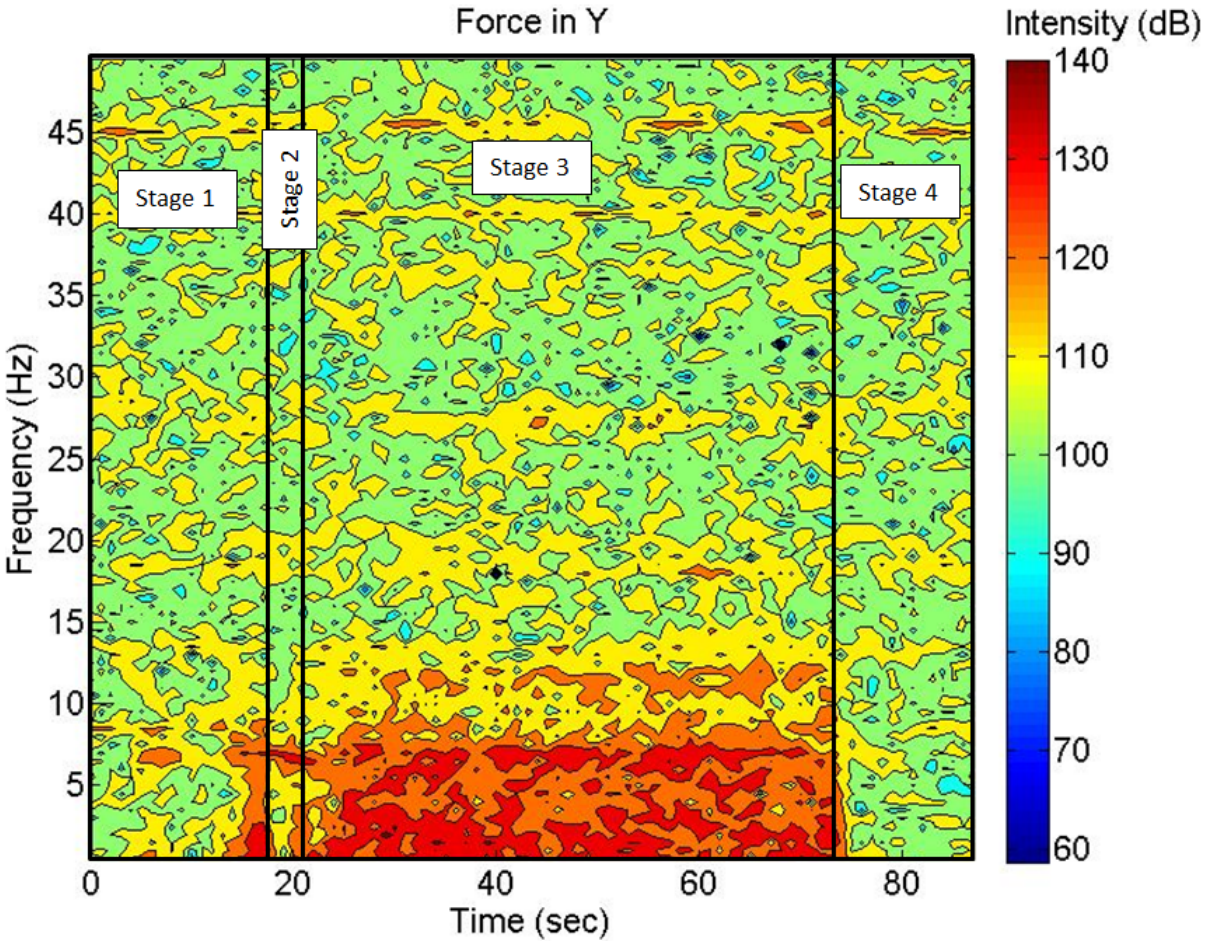

Figure 5.21: Force F_y spectrogram of Case 2.

Figure 5.22 is the down force spectrogram resulting from the welding under these conditions, divided into the welding stages. The spectrogram shows many peaks in the low-frequency range with high intensity (greater than 130 dB). In addition, it has peaks of maximum intensity (greater than 140 dB) at the beginning of the welding when the tool penetrates. A high intensity peak is present at the lift-off of the tool.

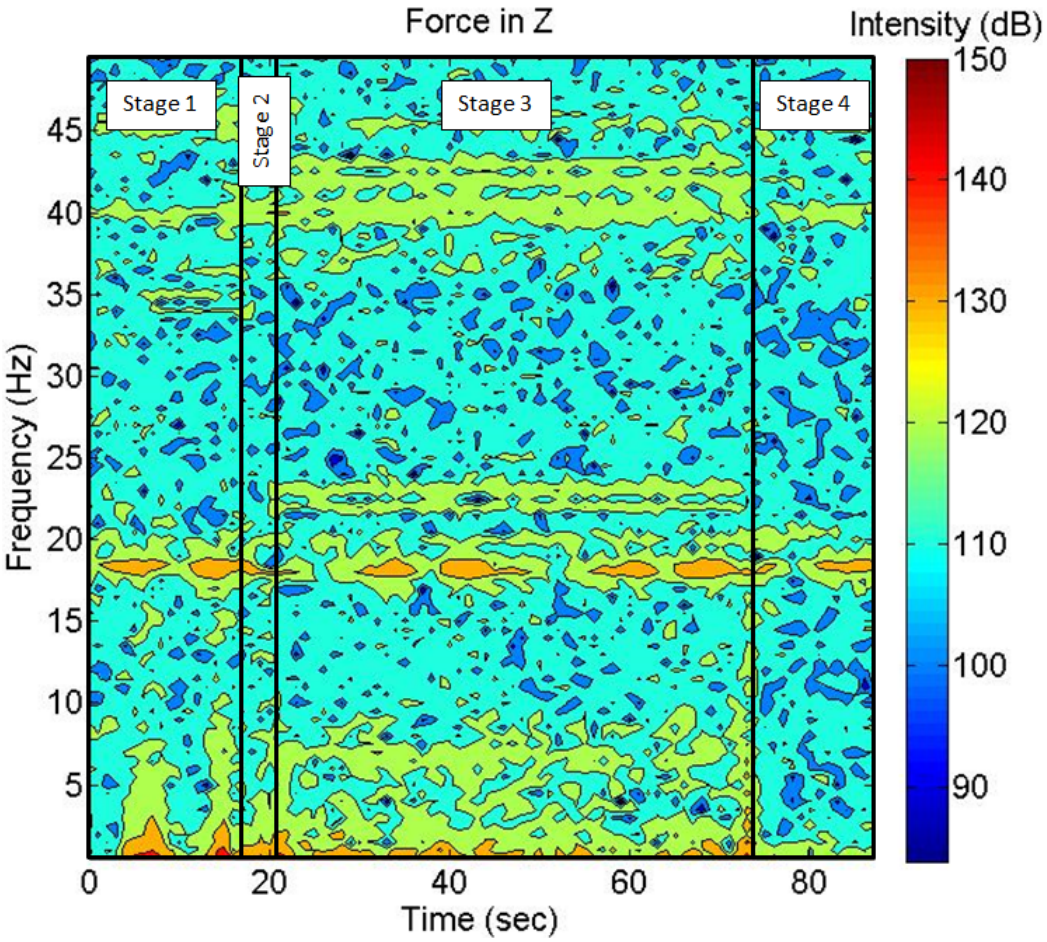

Figure 5.22: Force F_z spectrogram of Case 2.

Figure 5.23 is the spectrogram of the torque of the tool resulting from the previous welding, divided into the steps of the welding. The spectrogram shows peaks in the low-frequency range with maximum intensity (greater than 80 dB) along the welding. In addition, it has peaks of maximum intensity (greater than 80 dB) at the beginning of the welding when the tool penetrates. A high intensity peak is also present at the lift off of the tool.

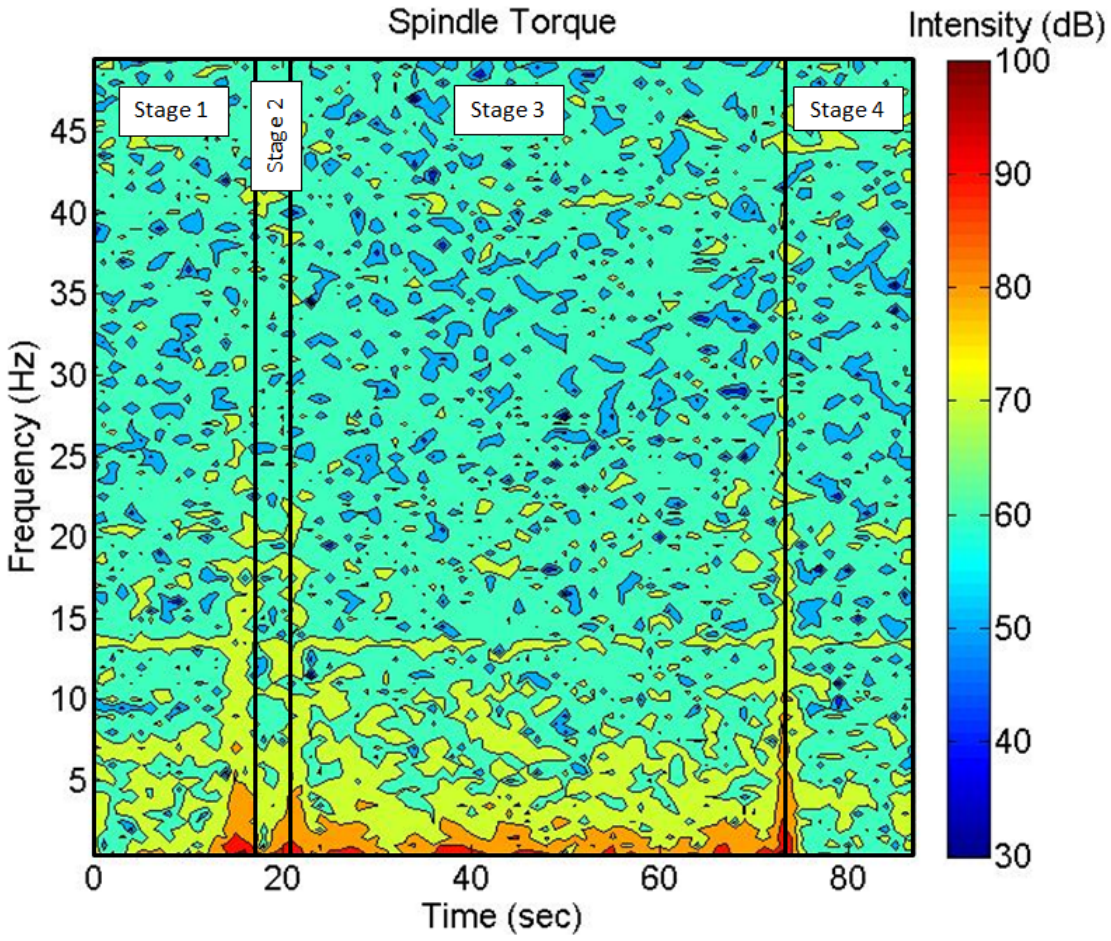

Figure 5.23: Spindle torque spectrogram of Case 2.

5.4.3 Case 3: ω = 500 rpm, ν= 50 mm/min, d_p = 2.25 mm

For the third case, ω = 500 rpm, ν= 50 mm/min and d_p = 2.25 mm, the resulting joint of the weld is shown in the Figure 5.24. The first half of the welding surface looks well, but the last part has a different texture. The weld also show a longitudinal cavity exit (wormhole) in the probe exit region, as shows the Figure 5.25

Figure 5.24: Welded plates of Case 3.

Figure 5.25: Probe exit of the weld of Case 3.

The forces and the spindle torque were examined by the spectral analysis. The Figure 5.26 shows the spectrogram of F_x.

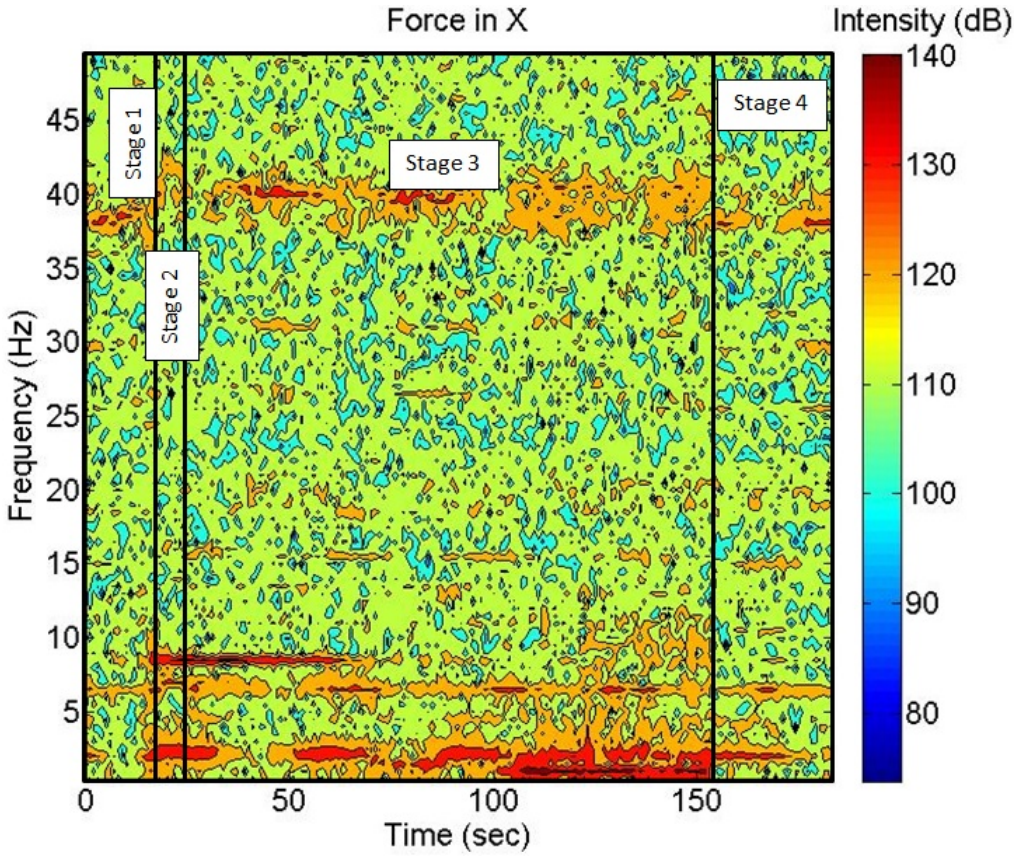

Figure 5.26: Force F_x spectrogram of Case 3.

Normally, the spectrogram should have a greater intensity in the spindle frequency, which is in this case 8.33 Hz (500 rpm). Nevertheless, for this case, only the first half of the welding has peaks near this value. Before that, the higher values in the low-frequency indicate a possible imperfection in the welding. The F_y spectrogram demonstrates a similar behavior as illustrated in the Figure 5.27.

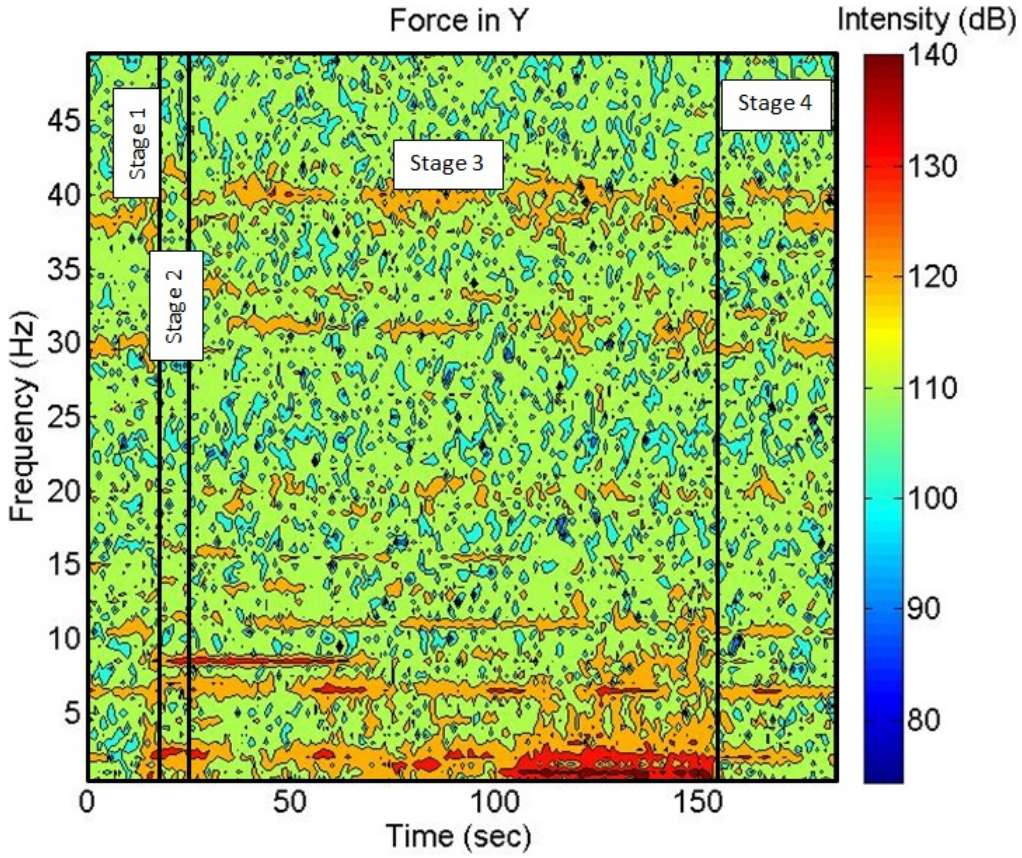

Figure 5.27: Force F_y spectrogram of Case 3.

The intensity of F_y is higher than F_x. In this signal, the intensity is higher mostly in the zone of low-frequency components. The down force F_z is illustrated in the Figure 5.28.

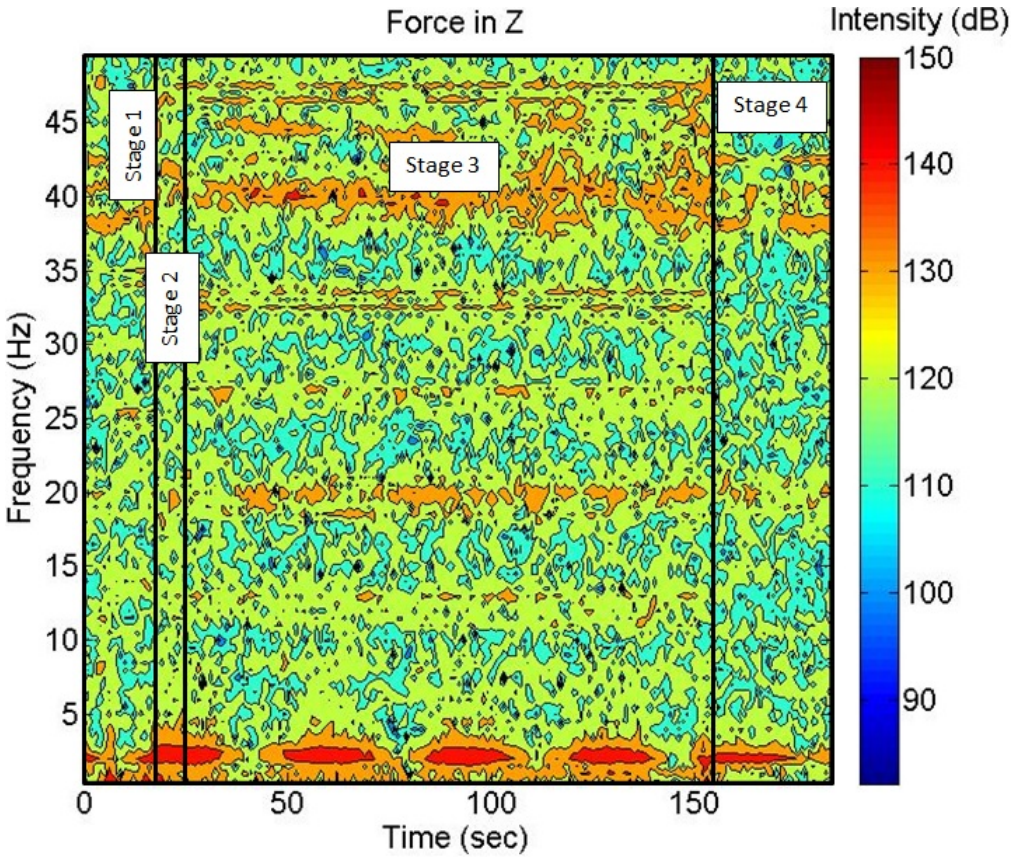

Figure 5.28: Force F_z spectrogram of Case 3.

In Figure 5.28, there are not components in the spindle frequency. The low-frequency patterns appear, showing that the F_z can also indicate an abnormality in the process. This pattern was also detected in the spectrogram of the torque as shown in Figure 5.29.

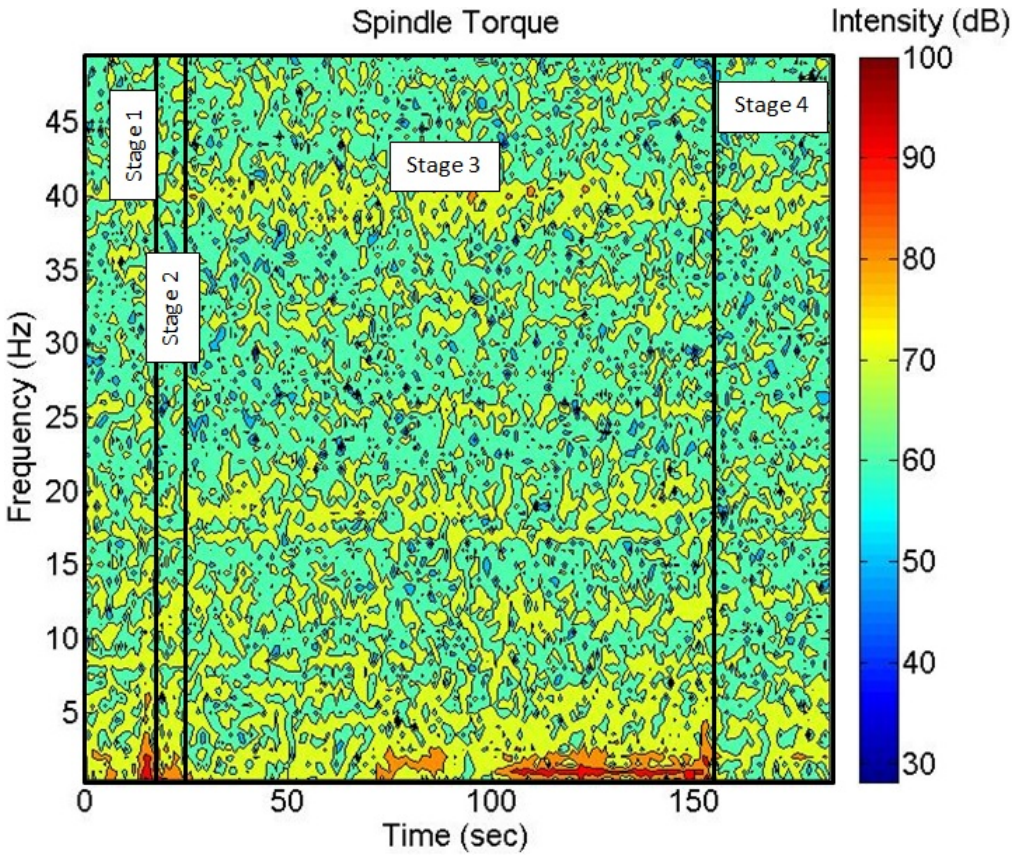

Figure 5.29: Spindle torque spectrogram of Case 3.

These low-frequency components may be caused by an imperfection, making important the examination of this section of the sample with more detail. For this purpose, the plates were cut transversely and then analyzed on the microscope to see if any imperfection occurred. The Figure 5.30 shows the traversing zone of the joint in the zone where the low-frequency components were higher.

Figure 5.30: Microscope picture of the welding in Case 3.

This picture of Figure 5.30 presents a series of cavities that corresponds to a discontinuity (wormholes), probably caused by noncontinuous material flow around the tool. The

changes in the welded were caused by geometric irregularities in the support of the welded pieces (backing) that altered the penetration depth value in the last part of the weld. This is the reason the components of the low frequency only appear in the second half of the weld.

5.4.4 Case 4: ω = 600 rpm, ν= 75 mm/min, d_p = 2.1 mm

In this case, the process conditions are ω = 600 rpm, ν= 75 mm/min and d_p = 2.1 mm, and the weld joint is illustrated in the Figure 5.31. The welding surface has an irregular texture and also has what appears to be a longitudinal cavity exit (wormhole) in the probe exit region, as shown in Figure 5.32

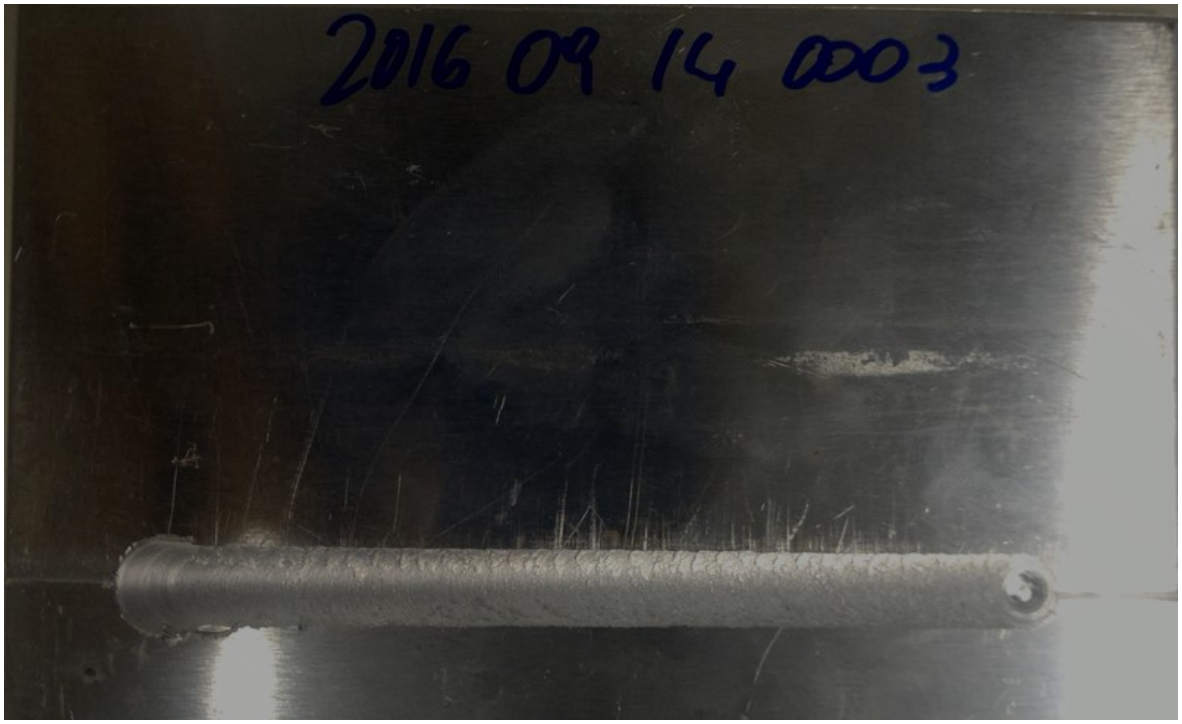

Figure 5.31: Welding plates in the Case 4.

Figure 5.32: Probe exit of the weld for Case 4.

Again, forces and the spindle torque were examined by the spectral analysis. The Figure 5.33 shows the spectrogram of F_x.

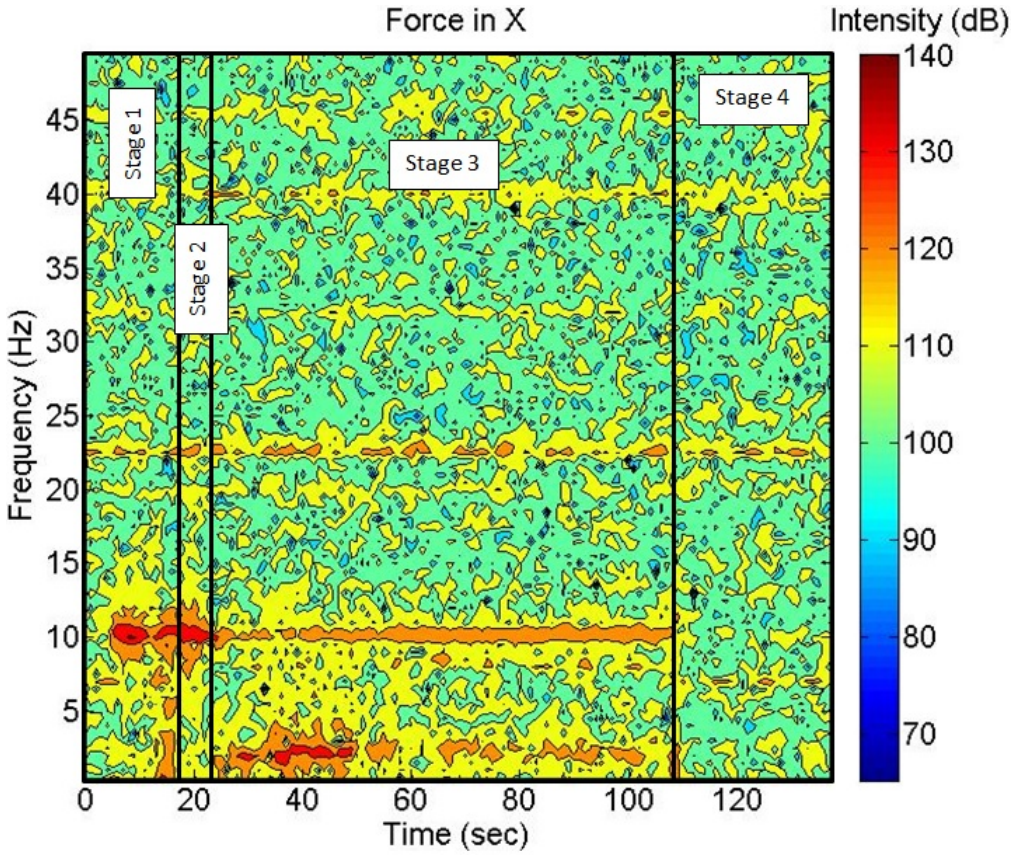

Figure 5.33: Force F_x spectrogram of Case 4.

For this welded joint, the force has a greater intensity in the spindle frequency of 10 Hz (600 rpm). In this case, there is a high intensity in the first stage of the process (plunging stage). But then, in the joining stage, the weld show lower amplitudes in this frequency. The spectrogram also shows peaks in the low-frequency components which indicate a possible imperfection in the welding.

The F_y spectrogram demonstrates a similar behavior as illustrated in Figure 5.34. The intensity of F_y is lower than F_x. In this signal, the intensity in the spindle frequency components is lower.

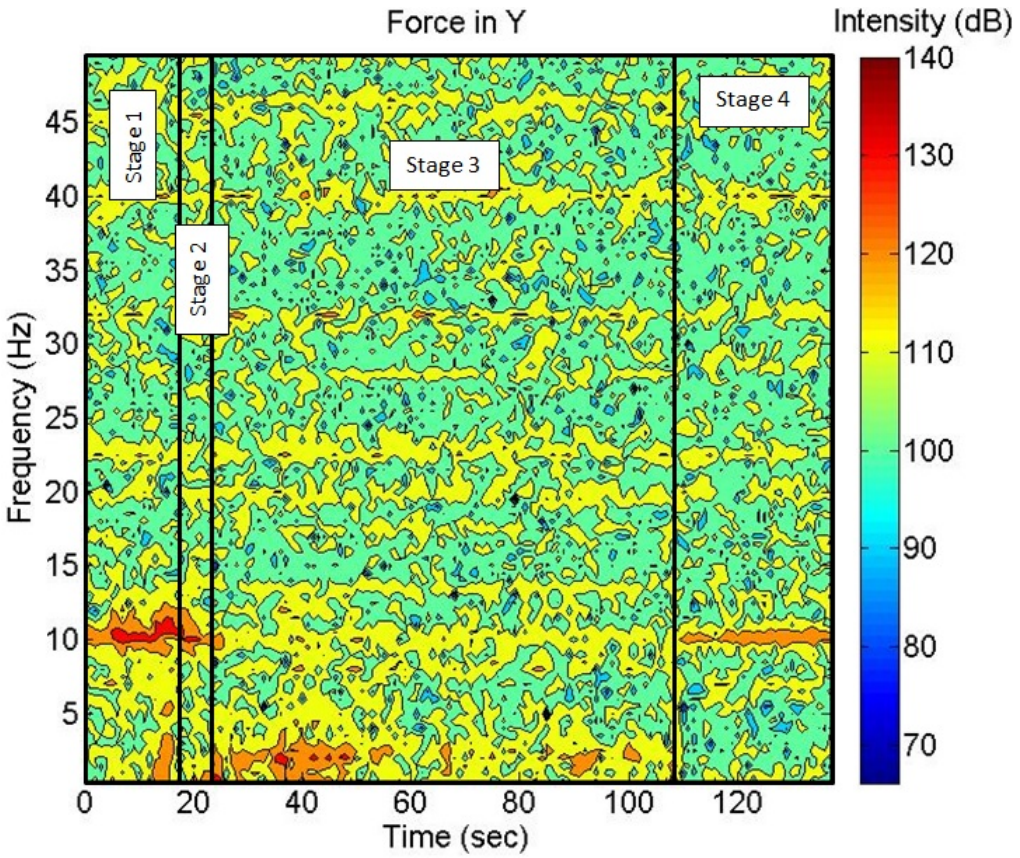

Figure 5.34: Force F_y spectogram of Case 4.

In contrast, the down force F_z spectrogram showed in the Figure 5.35 has a different response. In this case, there were not any components in the spindle frequency. There were only a few peaks in the low-frequency components. The low-frequency patterns didn't appear in this case, and there were a few peaks that may represent an imperfection in the process. The response is similar to the one presented in the spectrogram of the torque.

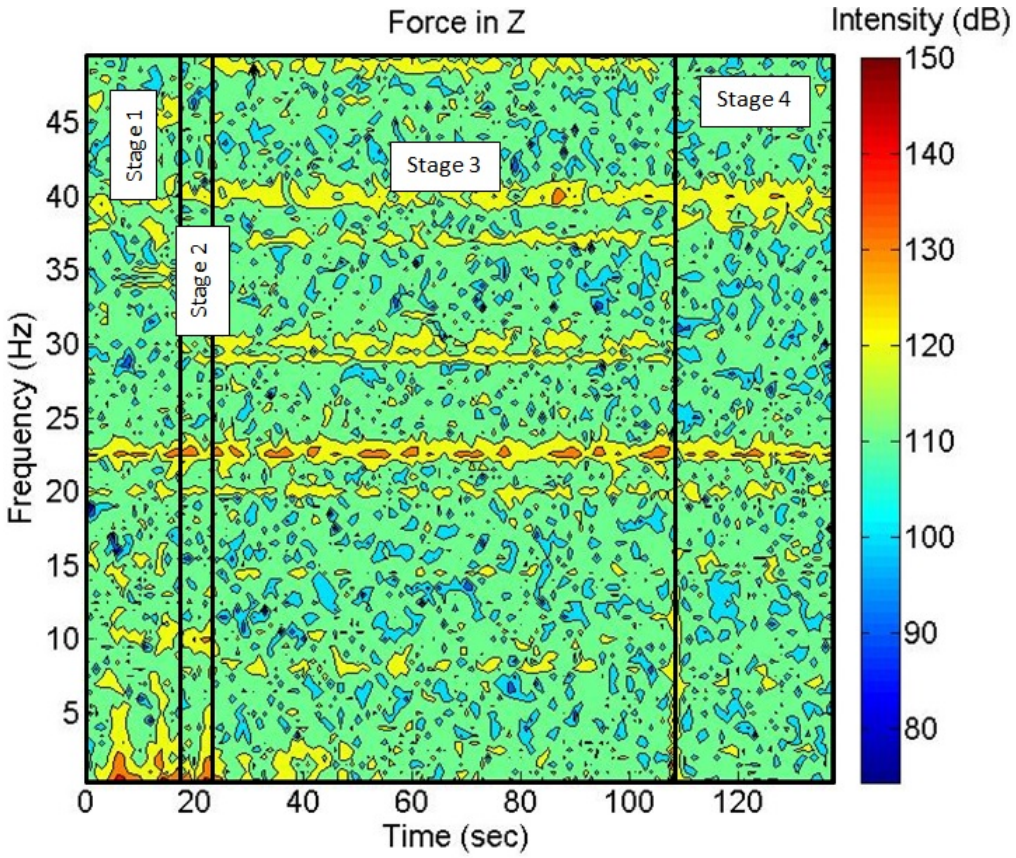

Figure 5.35: Force F_z spectrogram Case 4.

In Figure 5.36 the spectrogram of the torque is illustrated. The low-frequency peaks components in the F_x and F_y and the few peaks in F_z and torque may indicate the formation of an imperfection in the joint during the process. As a consequence, the plates were analyzed under the microscope to see if there is any imperfection occurring in this section.

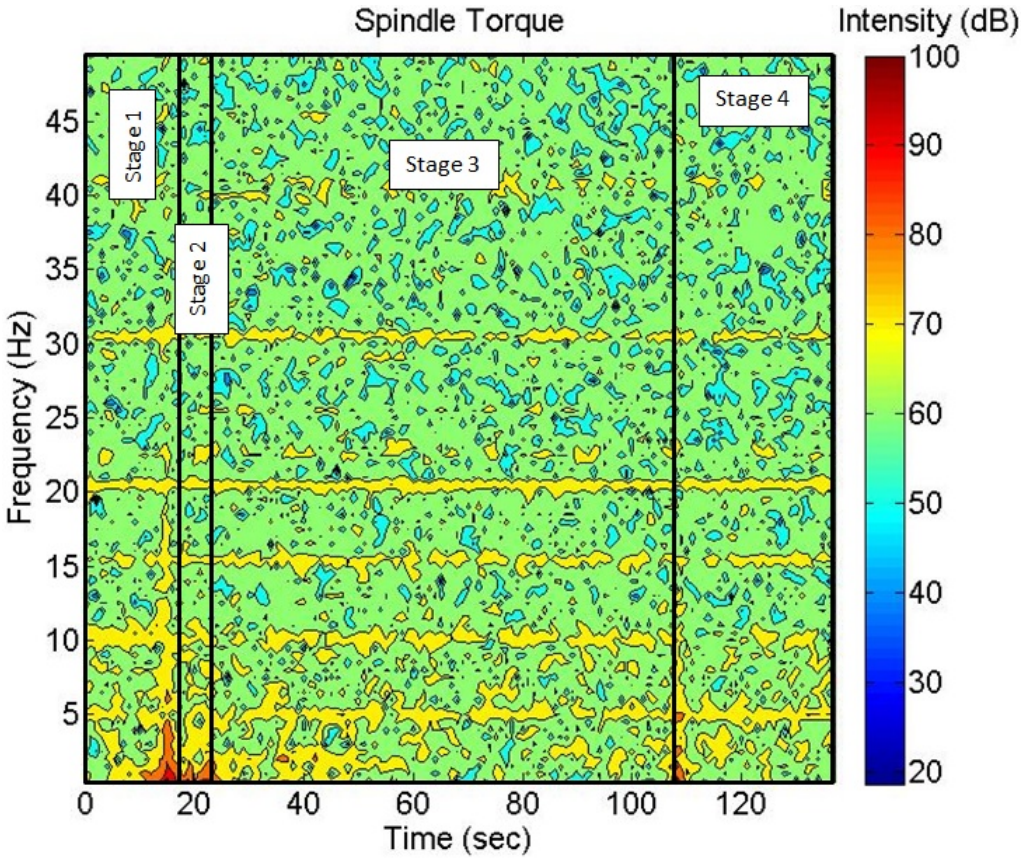

Figure 5.36: Spindle torque spectrogram of Case 4.

Figure 5.37 shows the traversing section of the joint in the zone where the low-frequency components were higher. This picture presents a great cavity that corresponds to an imperfection. The penetration depth of this weld was considerably low which is caused by a poor contact between the material and the tool shoulder. This is the reason why the components of the low frequency only appear in the F_x and F_y spectrogram. The F_z and the spindle torque spectrogram only have a few peaks of low frequency.

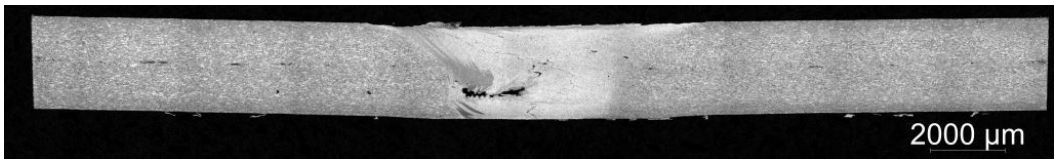

Figure 5.37: Microscope picture of the welding in Case 4

5.4.5 Case 5: ω = 600 rpm, ν= 125 mm/min, d_p = 2.4 mm

In this case, the process conditions are ω = 600 rpm, ν= 125 mm/min and d_p = 2.4 mm, and the welded joint is illustrated in Figure 5.38. The welding surface has a regular texture with fine flash and looks like achieving a good depth.

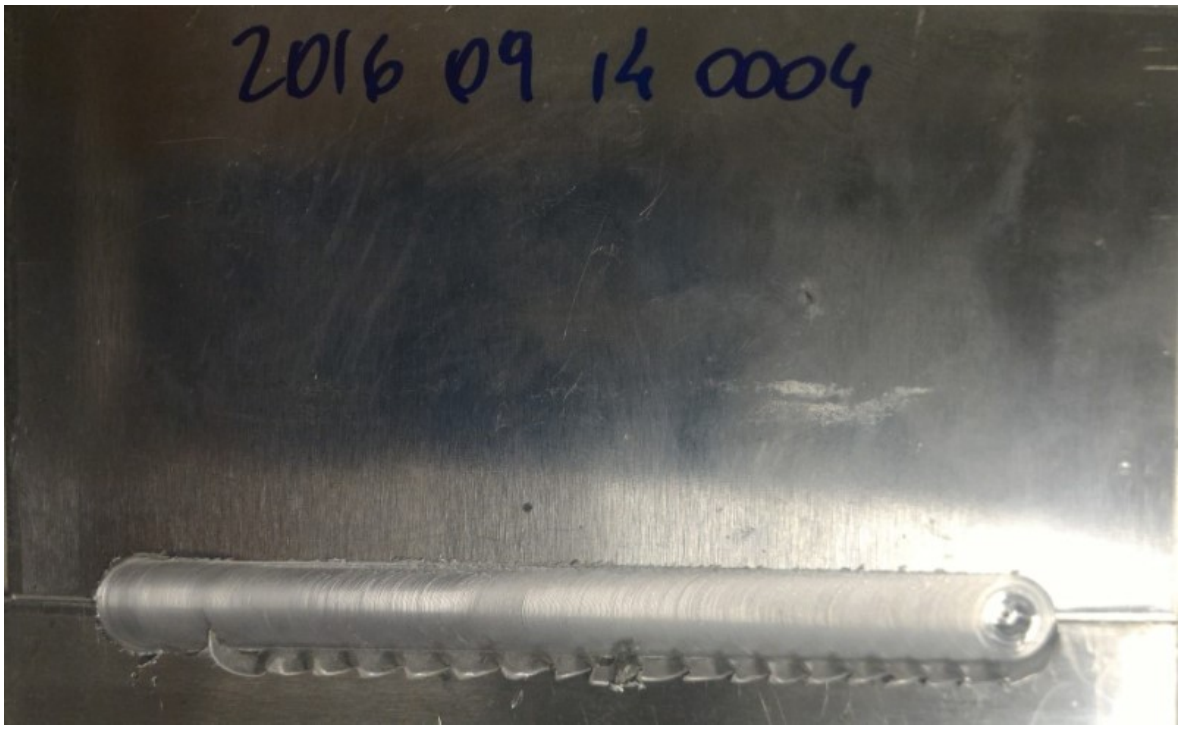

Figure 5.38: Welding plates in the Case 5.

Figure 5.39 shows the spectrogram of F_x, which represents the frequency response during the time and its intensity. For this welded joint, it is possible to see that the greater force intensity is in the spindle frequency, 10 Hz (600 rpm) in this case. However, these components decrease its value in the middle of the process. In addition, the graphic also didn't show peaks patterns in the low-frequency components that suggest a good behavior in the process.

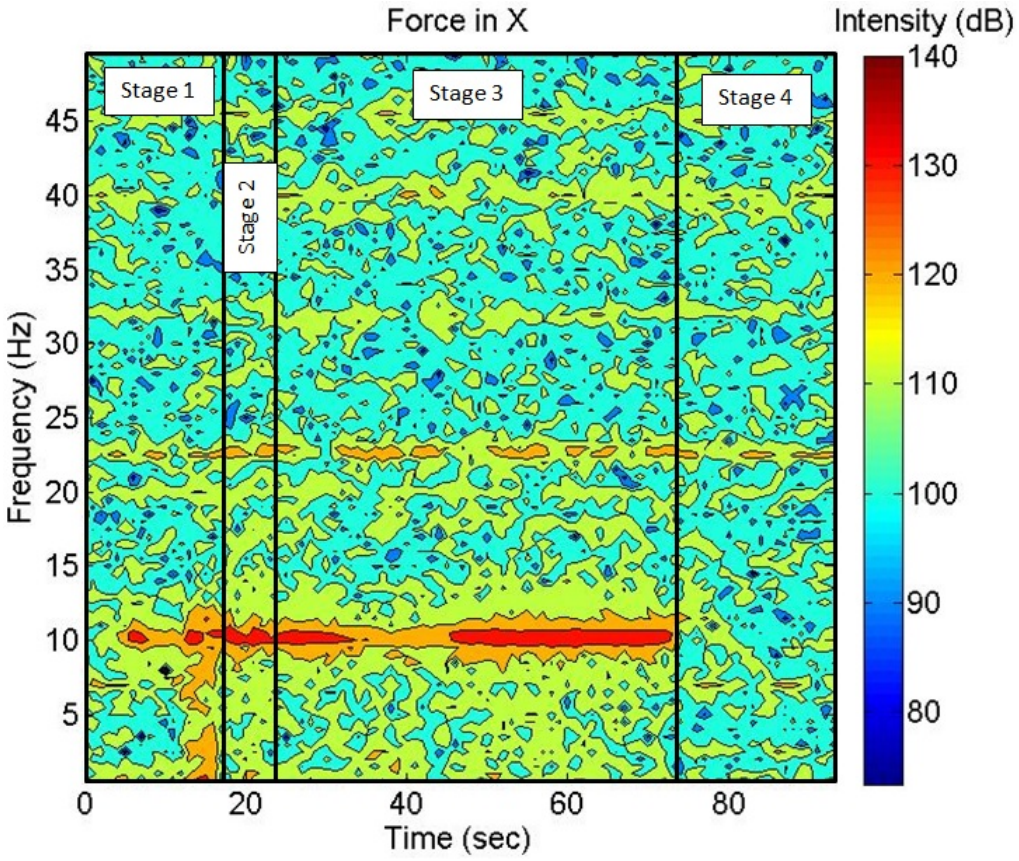

Figure 5.39: Force F_x spectrogram of Case 5.

Nevertheless, the F_y spectrogram, illustrated in the Figure 5.40, demonstrates some differences in the response that can suggest some imperfections. The F_y has components in the low frequency in the middle of the process, where the spindle components decrease.

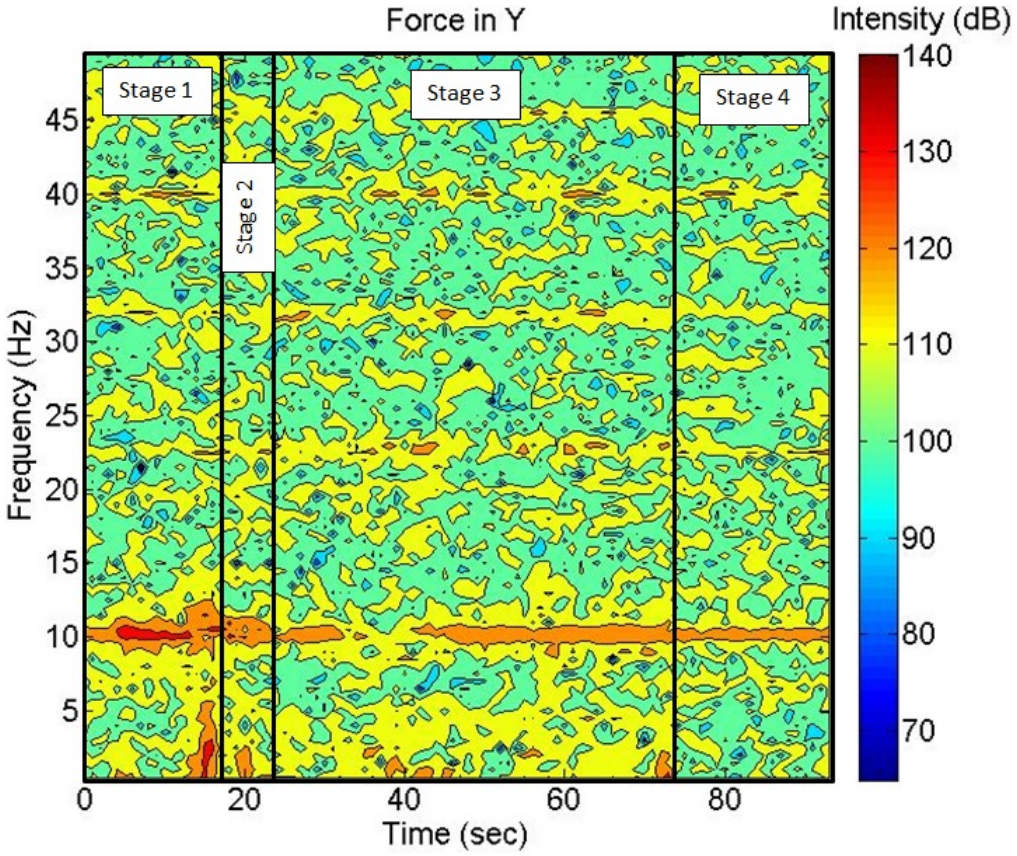

Figure 5.40: Force F_y spectrogram of Case 5.

Thus, the down force F_z spectrogram shows in Figure 5.41 some components in the low frequency in the same region, suggesting a possible imperfection in the middle of the weld.

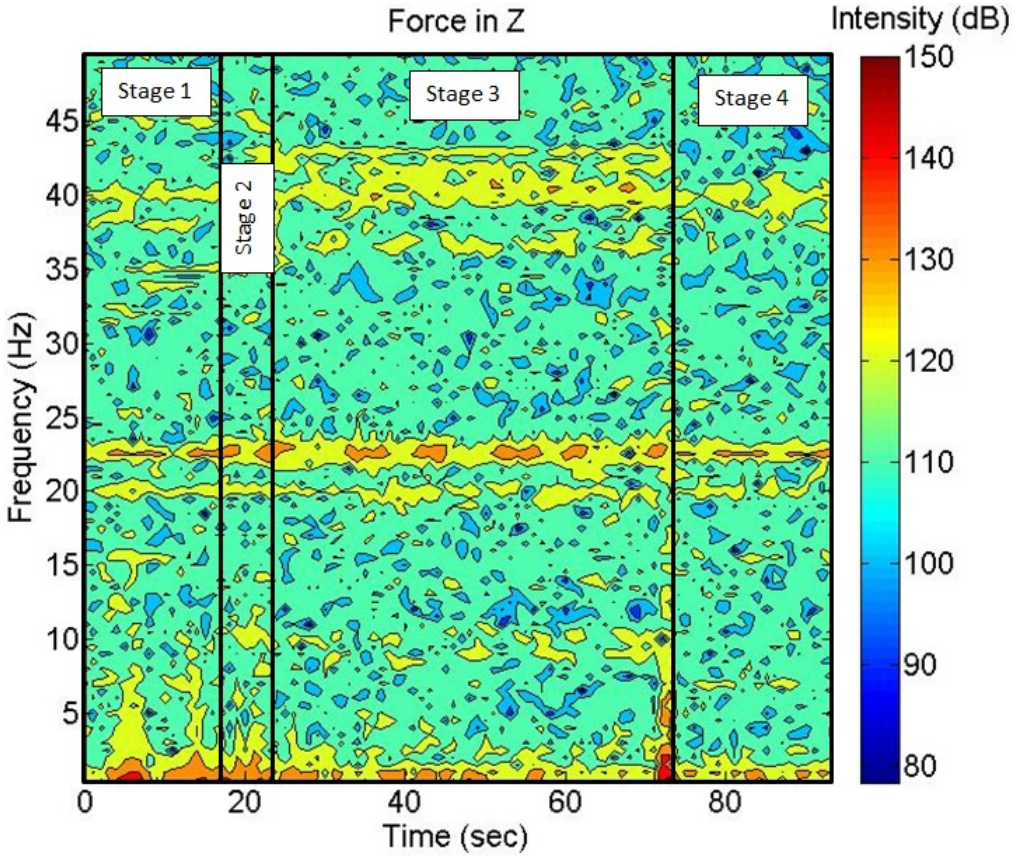

Figure 5.41: Force F_z spectrogram of Case 5.

The response was similar for the spindle torque response. The low-frequency components showed some peaks in the middle of the joint. The spectrogram of the torque is shown in the Figure 5.42.

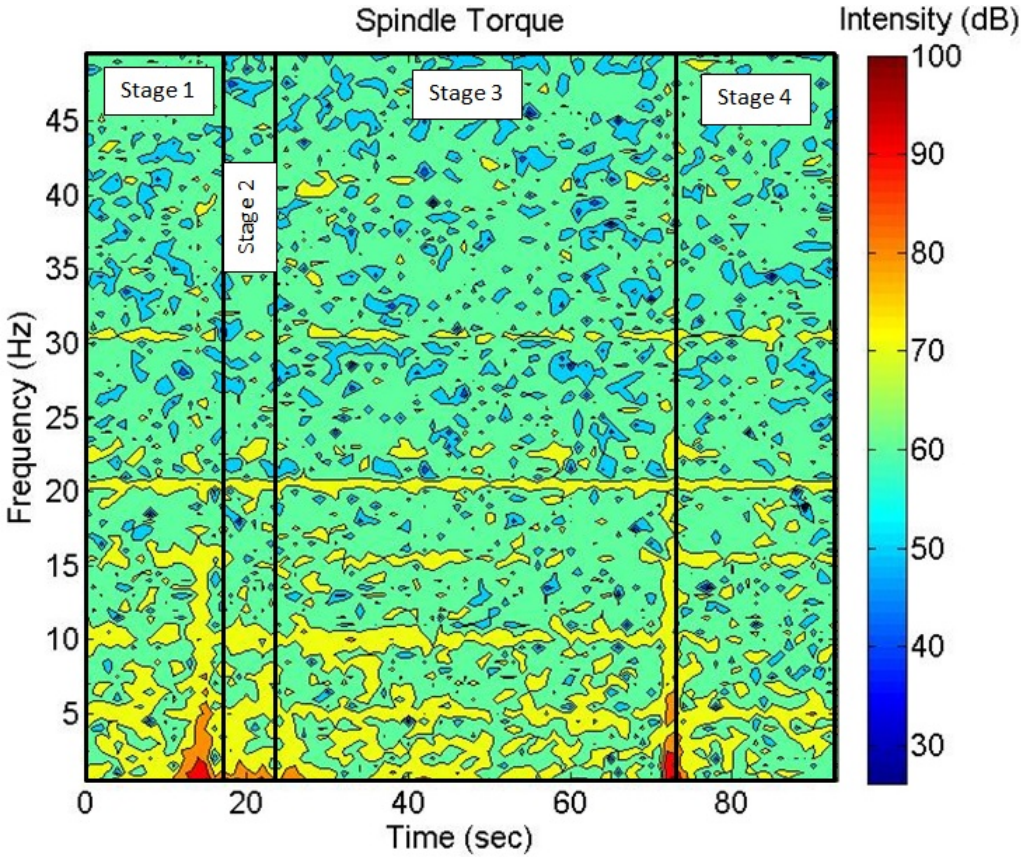

Figure 5.42: Spindle torque spectrogram of Case 5.

The low-frequency peaks in forces F_y and F_z, and for the spindle torque, may indicate the formation of an imperfection in the joint in the middle part of the process. The plates were analyzed, in the middle of it under the microscope to see if any imperfection occurred in this section. The Figure 5.43 shows the traversing zone of the joint in the zone of the low-frequency components. The result of the Figure 5.43 presents a little cavity that corresponds to a discontinuity, probably caused by the irregularities in the backing support especially in the middle of the process where the imperfection occurred. Even though, the rest of the weld has good characteristics. The middle part of the process looks like the only zone affected. The components of the low frequency only appear in the F_y, F_z and spindle torque spectrogram. The F_x spectrogram doesn't have these peaks in the low-frequency components.

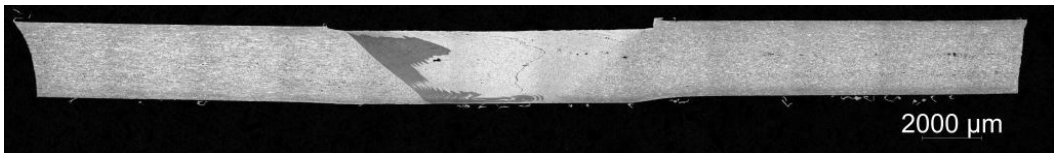

Figure 5.43: Microscope picture welding of Case 5.

5.4.6 Case 6: ω = 400 rpm, ν= 75 mm/min, d_p = 2.1 mm

For this case, the conditions are ω = 400 rpm, ν= 75 mm/min and d_p = 2.1 mm. The joint resulting of the weld is shown in the Figure 5.44. The welding surface has an irregular texture similar to the Case 4 and also has what appears to be a longitudinal cavity exit (wormhole) in the probe exit, as shown in Figure 5.45

Figure 5.44: Welding plates of Case 6.

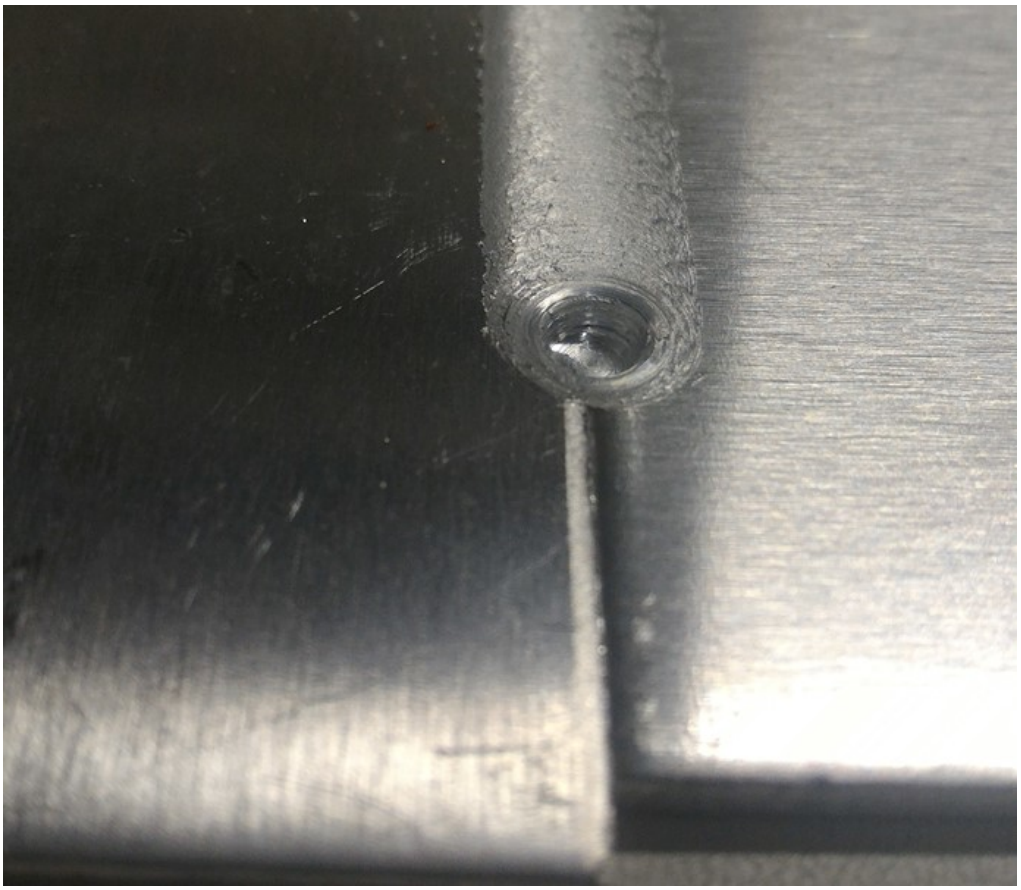

Figure 5.45: Probe exit of the welding of Case 6.

Thus, a spectral analysis was made for all forces and for the spindle torque. The Figure 5.46 illustrates the spectrogram of F_x, which represents the frequency response during the time and its intensity. For this welded joint, it is possible to see that the greater force intensity is in the spindle frequency, 6.33 Hz (400 rpm). Nevertheless, there are components in the low-frequency region, which may indicate an imperfection.

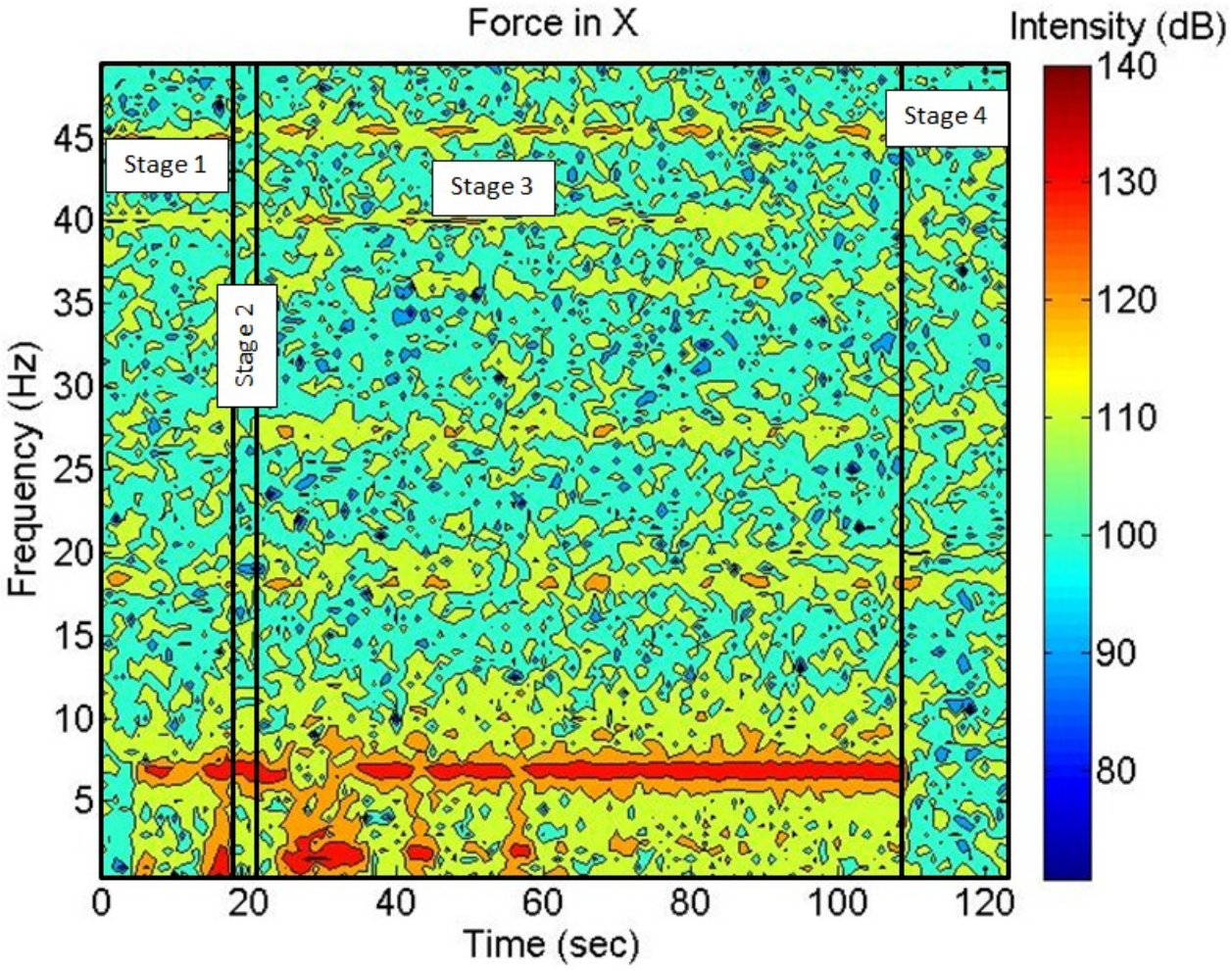

Figure 5.46: Force F_x spectrogram of Case 6.

Thus, the F_y shows a similar response spectrogram, as illustrated in the Figure 5.47. The intensity of F_y is lower than F_x. In this signal, the intensity is higher in the zone of low-frequency components.

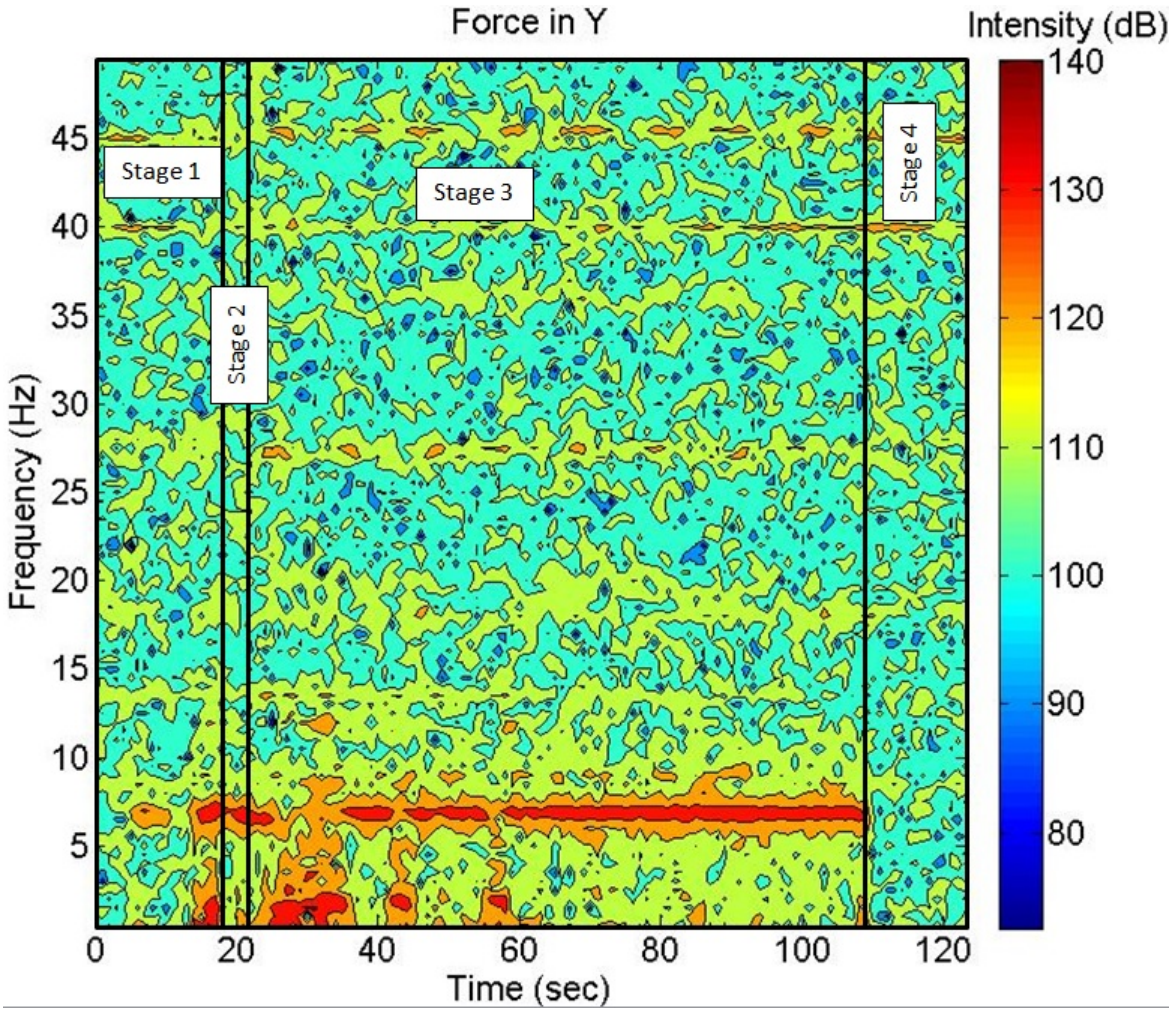

Figure 5.47: Force F_y spectrogram of Case 6.

In contrast, the down force F_z, illustrated in the Figure 5.48, has only a few peaks components in the low frequency in the same region.

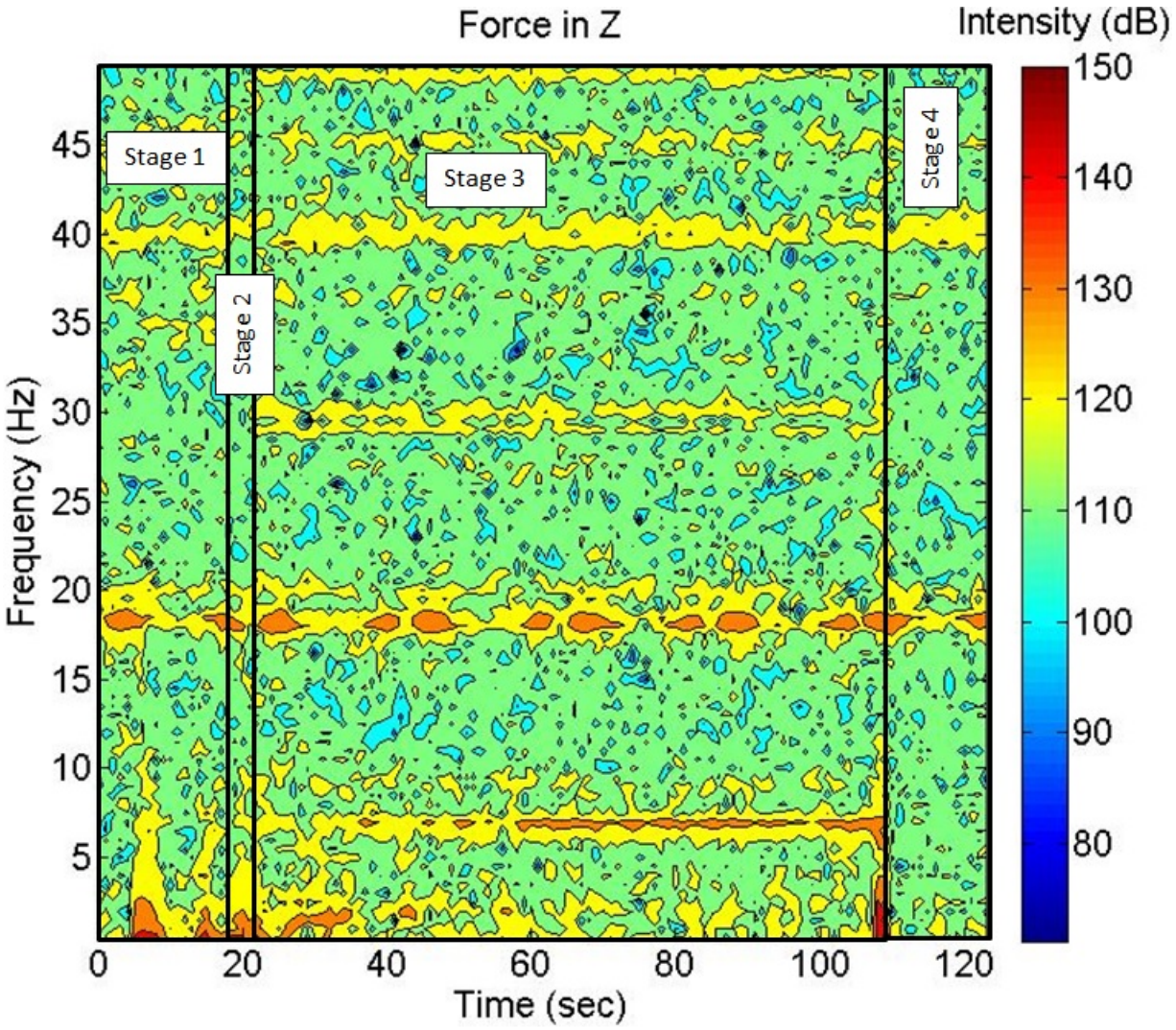

Figure 5.48: Force F_z spectrogram of Case 6.

For the torque, there are some components in the spindle frequency at the beginning of the welding process. The low-frequency big patterns didn't appear. These few peaks may suggest an imperfection in the process. The response is similar to those in the F_z response. The spectrogram of the torque is shown in Figure 5.49.

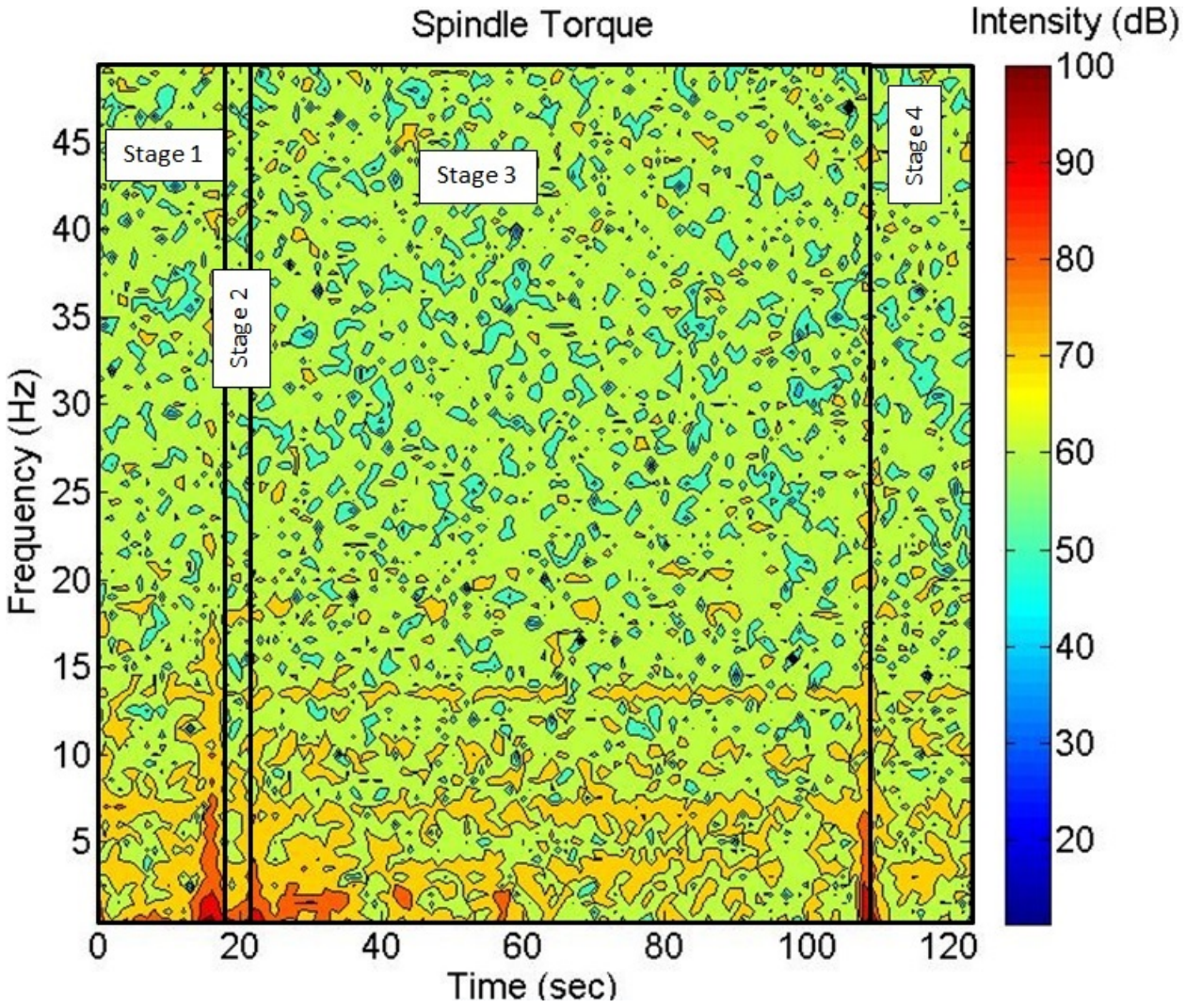

Figure 5.49: Spindle Torque spectrogram of Case 6.

These peaks in the low-frequency components of the F_x and F_y, and with less intensity for F_z and for the spindle torque, may correspond to the formation of an imperfection in the joint during the process in the middle of it. Therefore, the plates were analyzed by the microscope to see if any imperfection occurs in this section. The Figure 5.50 shows the traversing zone of the joint in the zone where the low-frequency components were higher. This picture presents some small cavities, probably caused by an insufficient penetration depth. The penetration depth of this weld was considerably low caused by a poor contact between the material and the tool shoulder. This is why in the F_z and torque spectrum only a few peaks in low-frequency are present.

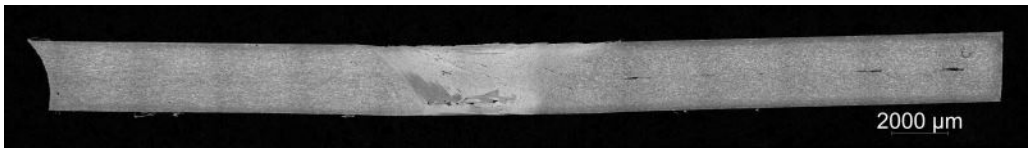

Figure 5.50: Microscope picture of the welding of Case 6.

5.5 Fuzzy detection system

Due to the previous results, the spectrum can be used as measure variable to detect the imperfections. However, the usage of the spectral response of each variable isolated can represent a difficulty because they have a different behavior and they may fail if only one signal is using in the analysis. For that reason a fuzzy logic system is suggested, taking into account the four outputs (tool forces and the spindle torque spectrogram). The fuzzy system was developed to define a void detection. First, using the results of the spectrograms, the amplitudes of spectrum were identified to define the membership function of the inputs. In this case, two trapezoidal membership functions (high and low) are used for every input. The Figure 5.51 presents the membership function used for every input. This figure shows also the interval of the amplitude spectrum used for every input. These intervals were defined using the measurement range with a good and bad welding (cases 1 and 2).

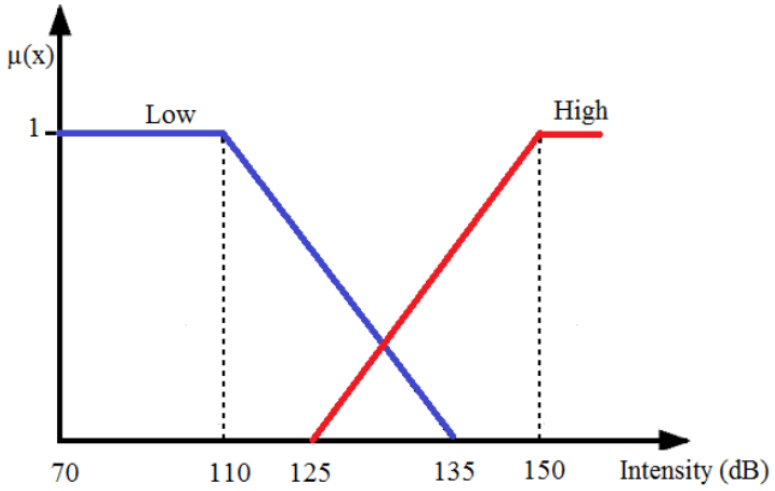

(a) Membership function for forces spectrum SF_x and SF_y.

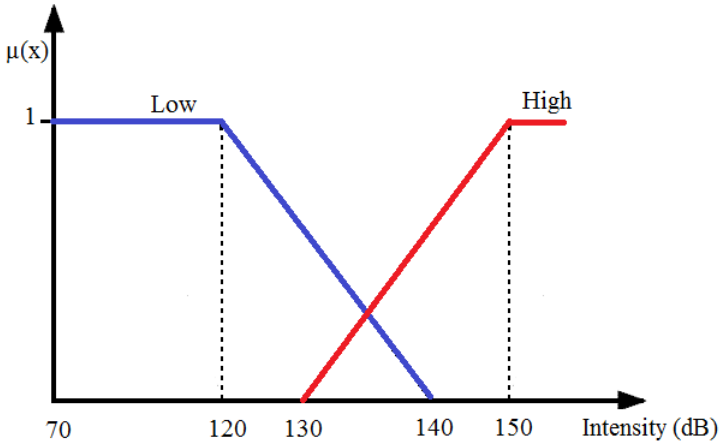

(b) Membership function for force spectrum SF_z.

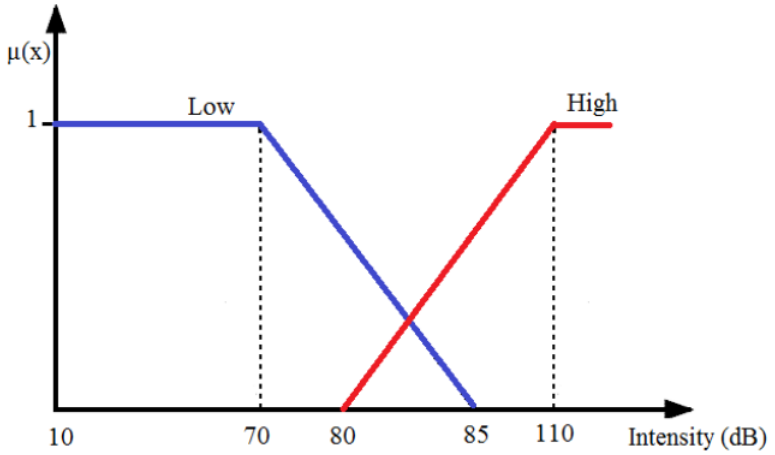

(c) Membership function for torque spectrum ST.

Figure 5.51: Membership functions and intensity interval used in for the fuzzy system.

The spectrogram shows that the low-frequency amplitude spectrum interval (below the spindle frequency) is the most important for the imperfection detection. So for every time window of the spectrogram, the algorithm takes the maximum amplitude spectrum value of the low-frequency interval. This value is selected for every variable measurement, to be compared with the other signals. If this amplitude spectrum value is high in the low-frequency interval, it will be an indicator of an imperfection. If this value is low, indicates no imperfection during the process. The algorithm takes the amplitude spectrum in the decibel scale, to simplify the calculations. The sensitivity of every input is different as was described earlier, so the scale of every measurement is different from the other, except for the side and traversing forces.

The interval shows that, for the side and traversing forces, the imperfection occurs when the amplitude spectrum is higher than 125 dB. The highest amplitude spectrum recorded was 150 dB, so the high membership function for the amplitude spectrum of the side and traversing forces was designed in that interval. The low interval was designed using the lowest value recorded 70 dB and 135 dB that is an amplitude spectrum value the imperfection is happening with certainty. Note that below 110 dB, the degree of membership 1, which means that values are too low and represent no chance of imperfection. This procedure was repeated for the down force and the torque amplitude spectrum, taking into account their particular intervals.

After the classification of the inputs, it is necessary to relate these with the probability of an imperfection in the welding process. So, as part of the knowledge base, the linguistic rules can be established with the information of previous results. These rules have an if-then logic, so every combination of variables will be covered. The rules are described as it follows:

- **rule 1**: If SF_x is High and SF_y is High and SF_z is High and ST is High then P is Bad.
- **rule 2**: If SF_x is Low and SF_y is Low and SF_z is Low and ST is Low then P is Good.
- **rule 3**: If SF_x is Low and SF_y is High and SF_z is High and ST is High then P is Bad.
- **rule 4**: If SF_x is High and SF_y is High and SF_z is High and ST is Low then P is Good.
- **rule 5**: If SF_x is Low and SF_y is High and SF_z is Low and ST is High then P is Bad.
- **rule 6**: If SF_x is High and SF_y is Low and SF_z is Low and ST is High then P is Bad.
- **rule 7**: If SF_x is High and SF_y is Low and SF_z is High and ST is Low then P is Good.

- **rule 8**: If SF_x is Low and SF_y is High and SF_z is High and ST is Low then P is Good.
- **rule 9**: If SF_x is Low and SF_y is High and SF_z is Low and ST is Low then P is Good.
- **rule 10**: If SF_x is Low and SF_y is Low and SF_z is High and ST is Low then P is Good.
- **rule 11**: If SF_x is High and SF_y is High and SF_z is Low and ST is High then P is Bad.
- **rule 12**: If SF_x is High and SF_y is Low and SF_z is High and ST is High then P is Bad.
- **rule 13**: If SF_x is High and SF_y is High and SF_z is Low and ST is Low then P is Bad.
- **rule 14**: If SF_x is Low and SF_y is Low and SF_z is High and ST is High then P is Bad.
- **rule 15**: If SF_x is High and SF_y is Low and SF_z is Low and ST is Low then P is Good.
- **rule 16**: If SF_x is Low and SF_y is Low and SF_z is Low and ST is High then P is Bad.

where SF_x is the traversing force amplitude spectrum, SF_y is the side force amplitude spectrum, SF_z is the down force amplitude spectrum, ST is the spindle torque amplitude spectrum and P is the imperfection probability. The SF_x, SF_y, SF_z and ST.

The output is also a linguistic variable and it can be **Bad** or **Good** determining if the process has a good or a bad performance. Figure 5.52 illustrates the membership function used for the output of the fuzzy linguistic model.

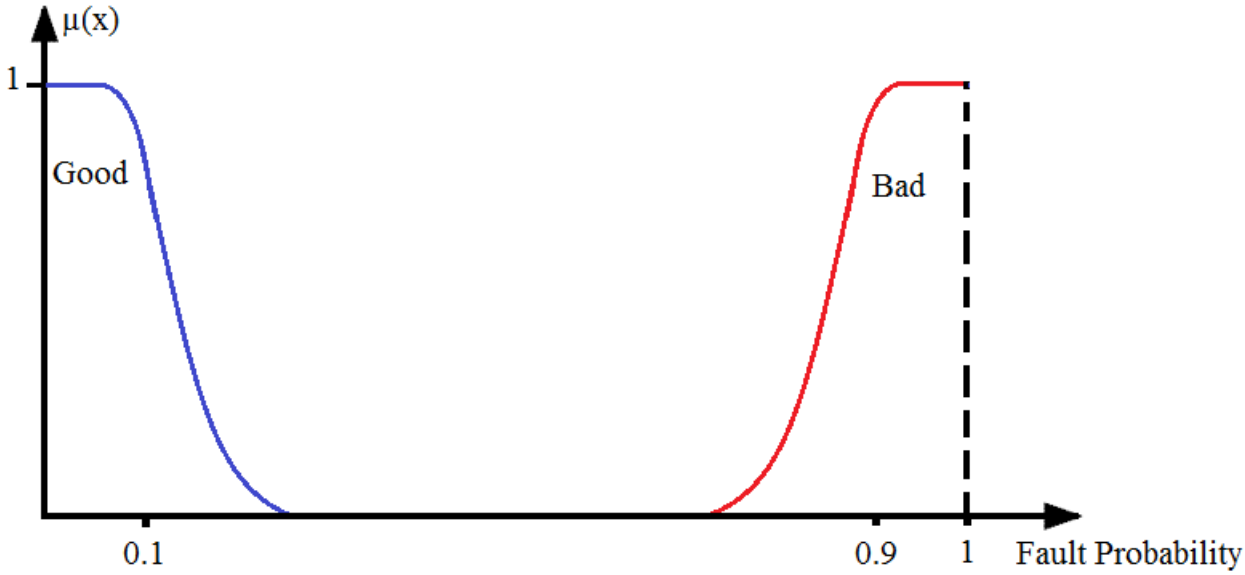

Figure 5.52: Membership function of the output of the fuzzy system (probability).

The two membership functions are generalized bell type and they were positioned near to 0 representing a good welding, and near to 1 representing a bad behavior. The system does not have a fuzzy set or of the other set in the middle of the interval, pushing the fuzzy logic system to decide between the two set bad or good. This avoids the problem of having a 50% of imperfection probability. Finally, the defuzzification transforms the linguistic output variable, into a numeric value. In this case, the Mean of Maximum (MoM) defuzzification method was used. This method uses the maximum degree of membership to all functions for determining the numeric value output. In this case, the MATLAB Fuzzy logic toolbox was used to elaborate the detection system (MATHWORKS, 2001).

5.6 Results for the cases

5.6.1 Detection Case 1: ω = 500 rpm, ν= 100 mm/min, d_p = 2.45 mm

For the Case 1, the spectrograms and the fuzzy logic system were used to obtain the probability of failure as a function of time. The value 1 indicates high probability and the value 0 indicates low probability. The stages 1, 2, and 4 were evaluated but not considered because the always represent a high value of the spectrum amplitude component and because the welding process take place only in the stage 3. During the stages 1, 2, and 4 the process has a transitory behavior, explaining these high components. In Figure 5.53 it is observed

that during stage 3, a probability is 0.97 at the beginning of the welding appears, but then it is 0.045 which confirms a good welding process. This clearly agrees with the previous analysis that there is no imperfection in this welding.

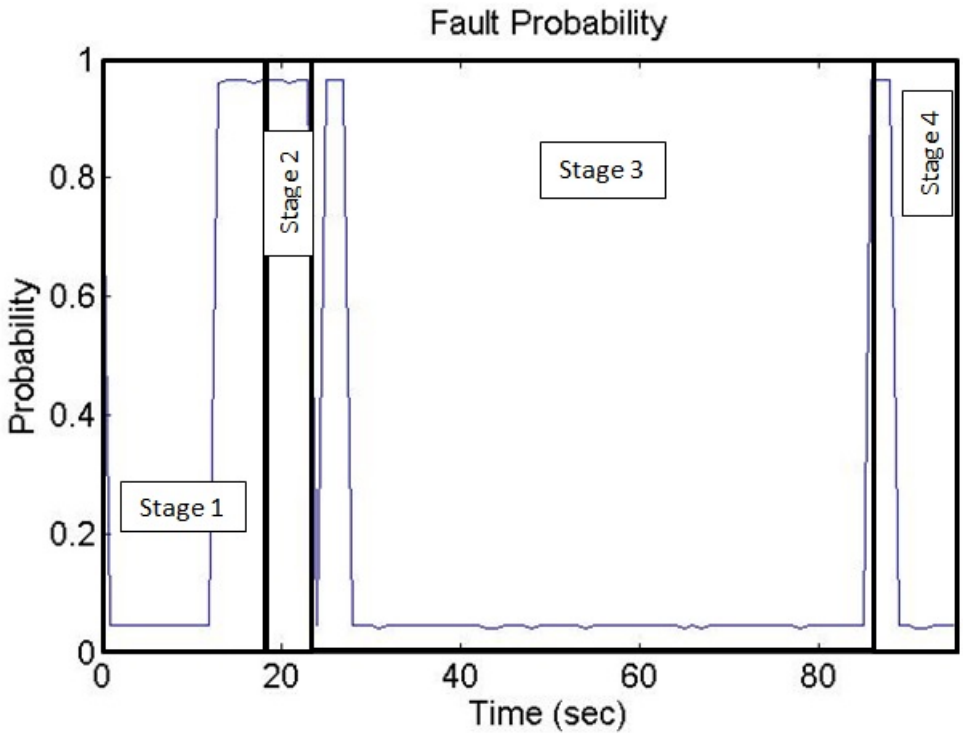

Figure 5.53: Probability of imperfection for every time for Case 1.

5.6.2 Detection Case 2: ω = 400 rpm, ν= 125 mm/min, d_p = 2.1 mm

For the Case 2, the analysis of the spectrum with fuzzy logic system computed the probability of failure as a function of time. Figure 5.54 illustrates that during stage 3, the probability is near to 0.97 which confirms the presence of failures along the welding. The joint presented visible imperfections in the surface of the weld, as shown in Figure 5.19.

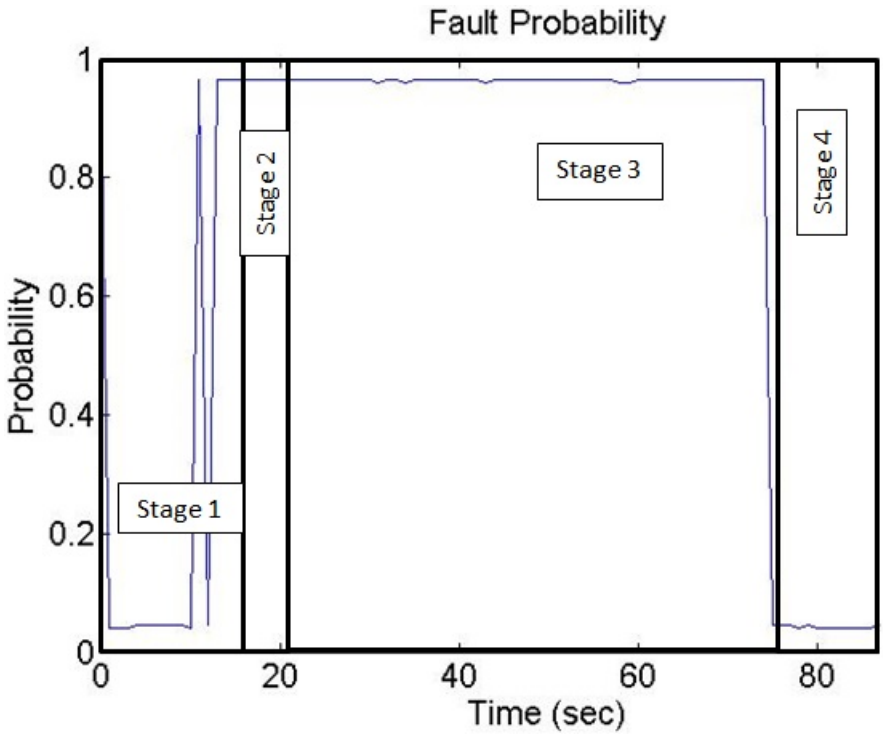

Figure 5.54: Probability of imperfection for every time for Case 2.

5.6.3 Detection Case 3: ω = 500 rpm, ν= 50 mm/min, d_p = 2.25 mm

For the Case 3, the analysis using a fuzzy logic obtained the probability of failure as a function of time. Figure 5.55 shows that during stage 3 a transitory behavior caused by the start of the movement. After this, from 25 seconds the process presented a good behavior with a probability less than 0.045, but at 75 seconds and then at 100 seconds, the system indicated an imperfection until the final part of the process.

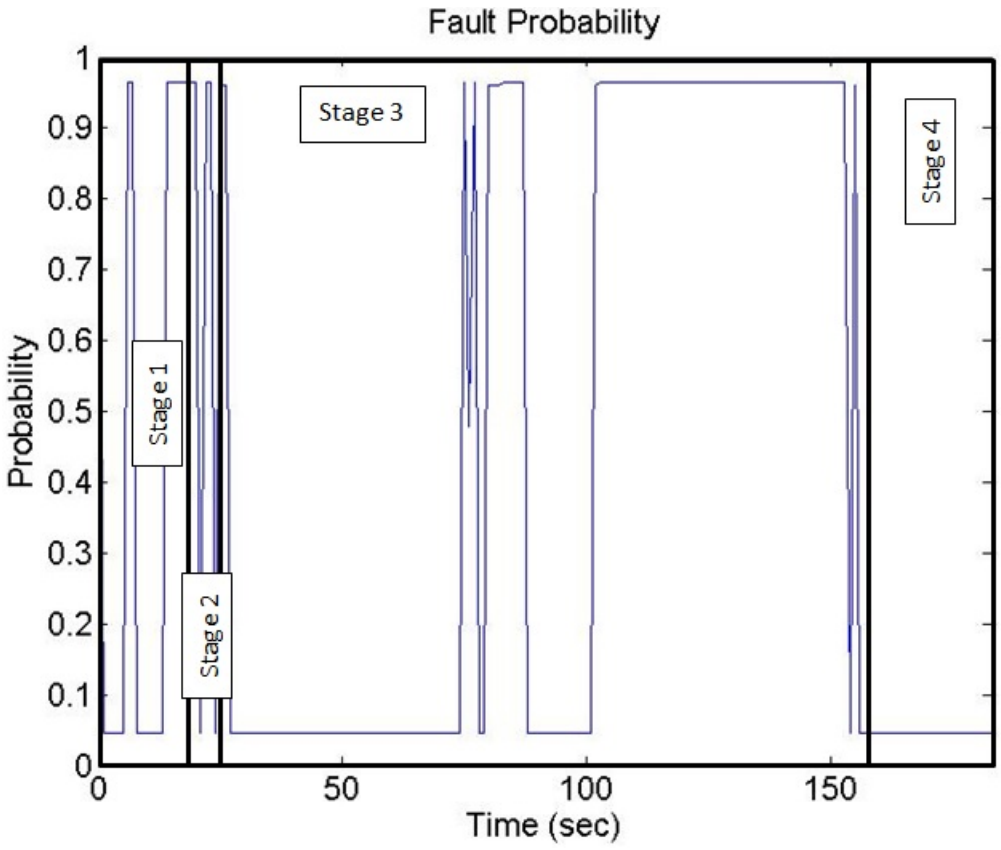

Figure 5.55: Probability of imperfection for every time for Case 3.

5.6.4 Detection Case 4: ω = 600 rpm, ν= 75 mm/min, d_p = 2.1 mm

For the Case 4, the analysis using a fuzzy logic determined the probability of imperfection. Figure 5.56 shows that during stage 3 the transitory behavior caused by the start of the movement. Then there is a good behavior with a probability less than 0.045 until the 35 seconds. After this, the system detects an imperfection until 50 seconds of the process, and after the 50 seconds of process the probability is low, indicating no failure.

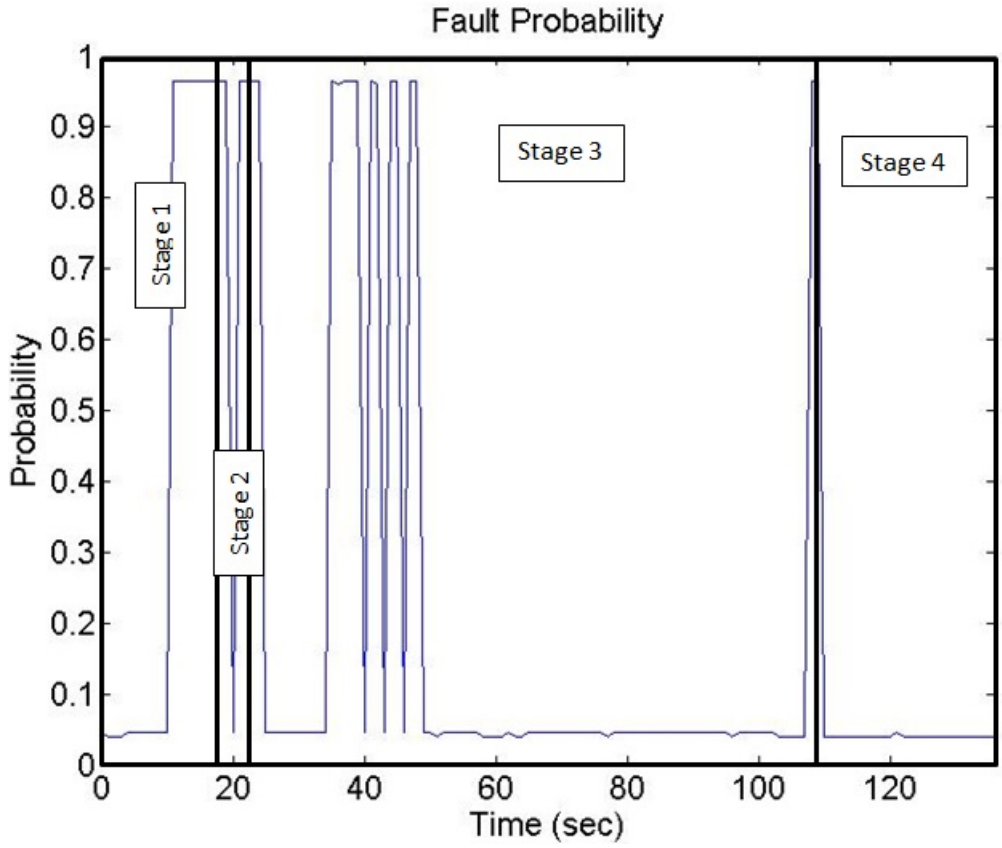

Figure 5.56: Probability of imperfection for every time for Case 4.

5.6.5 Detection Case 5: ω = 600 rpm, ν= 125 mm/min, d_p = 2.4 mm

For the Case 5, Figure 5.57 shows the probability using the fuzzy system. During the stage 3, a transitory behavior caused by the start of the movement is verified. Then there was a good behavior with a probability is 0.045 until 42 second of the process, when the system detects a single imperfection in the process by the high level of probability. After that, imperfections were not detected (low probability).

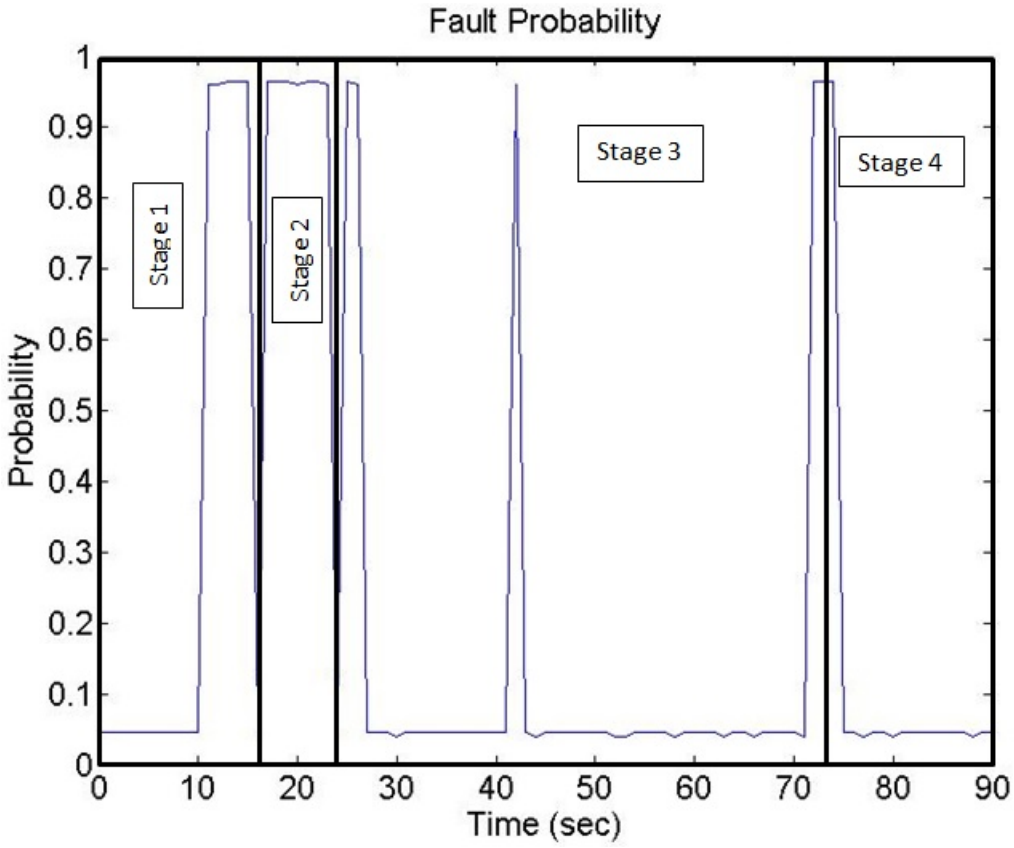

Figure 5.57: Probability of imperfection for every time for Case 5.

5.6.6 Detection Case 6: ω = 400 rpm, ν= 75 mm/min, d_p = 2.1 mm

For the Case 6, Figure 5.58 illustrates the fuzzy probability result. During stage 3, a transitory behavior caused by the start of the movement can be verified. Then there was a good behavior with a probability of 0.045 until 40 seconds, but after this time, the system detects imperfections at 42 and 58 seconds of the process. After this, no imperfection detection is verified.

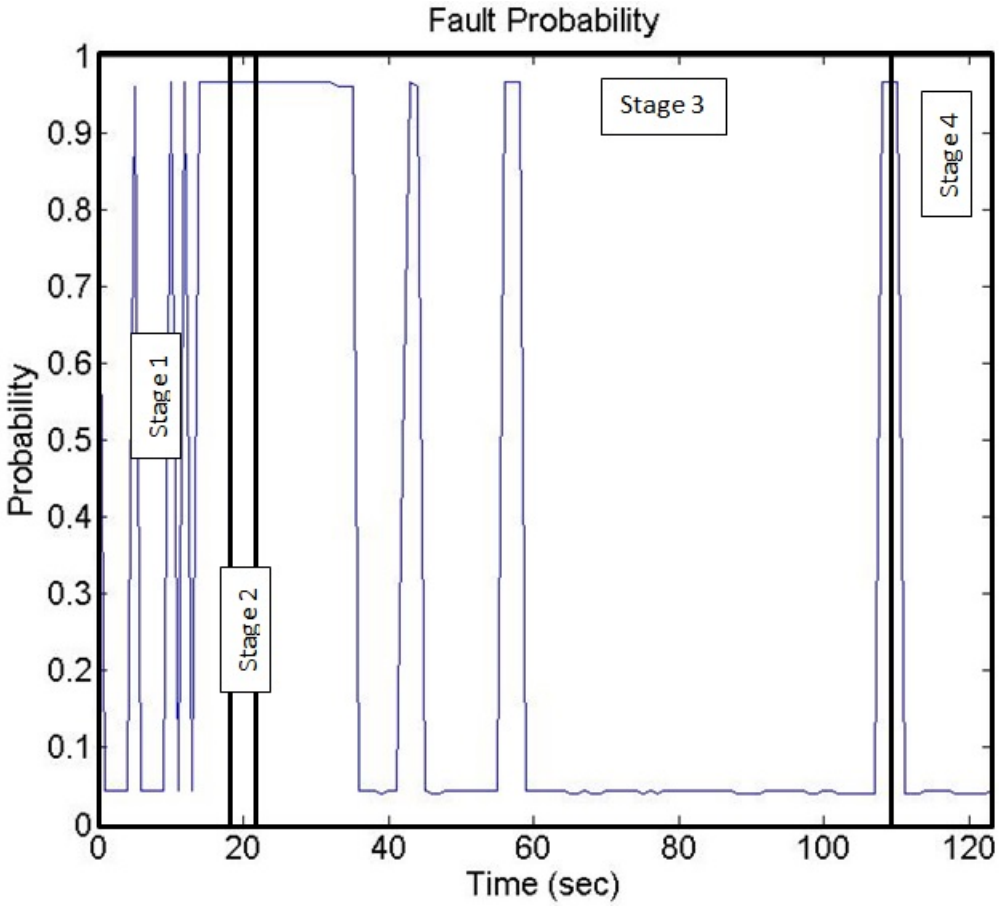

Figure 5.58: Probability of imperfection for every time for Case 6.

The detection system showed the imperfections approximately at the time when these occurred. Cases 3 to 6 were cut and analyzed under the microscope in the zone that corresponds to possible imperfection, as were showed earlier. All situations presented positive detection of imperfections in the welding.

5.7 Statistic Analysis of all cases

Due to the detection system behavior, the system was in all experiment cases of this work to know, the effect of the input parameters in the imperfections occurrence in the FSW process. As was mentioned in Chapter 4, the variance analysis (ANOVA) helps to identify the significant effects of a variable. Using the same design of experiment described in Chapter 4, the imperfection probability was analyzed. For this analysis, every operational point (the rotation speed, traversing speed, the tool penetration depth) that had an imperfection occur-

rence has the value of 1, and if there is not imperfection the value is 0. Table 5.1 present the ANOVA analysis for these cases.

Table 5.1: Imperfection probability ANOVA.

Source	Sq sum	d.f.	Mean Sq	F	p-value
d_p	0.93516	1	0.93516	7.5212	0.0122
ω	0.78125	1	0.78125	6.2833	0.02048
ν	0.78125	1	0.78125	6.2833	0.02048
$d_p\ \omega$	0.5625	1	0.5625	4.5239	0.0454
$d_p\ \nu$	0.0625	1	0.0625	0.5026	0.4861
$\omega\ \nu$	0.0625	1	0.0625	0.5026	0.4861
d_p^2	0.4617	1	0.4617	3.7139	0.0676
ω^2	0.2561	1	0.2561	2.0598	0.1659
ν^2	0.7116	1	0.7116	5.7239	0.0261
Error	2.611	21	0.1243		
Total	7.3548	30			

From the ANOVA results, it is possible to verify that the three inputs affect the imperfection probability. We found out that the penetration depth affects the imperfection probability significantly as shown by the p-value of 0.0122. The low level in the depth shows the worst behavior in the welding. The rotational speed and the traversing speed presented significant values, both with a p-value of 0.02048. The worst results using these variables were when the rotation speed has the lower level and the traversing speed has the higher level. Another interesting aspect is the significant level of nonlinear terms, i.e., the interaction between the rotational speed and depth, and the pure quadratic term of the traversing speed. Using ANOVA information, a surface contour was plotted. Figure 5.59 represents the variation of the probability of imperfection as the rotation speed and the traversing speed changes.

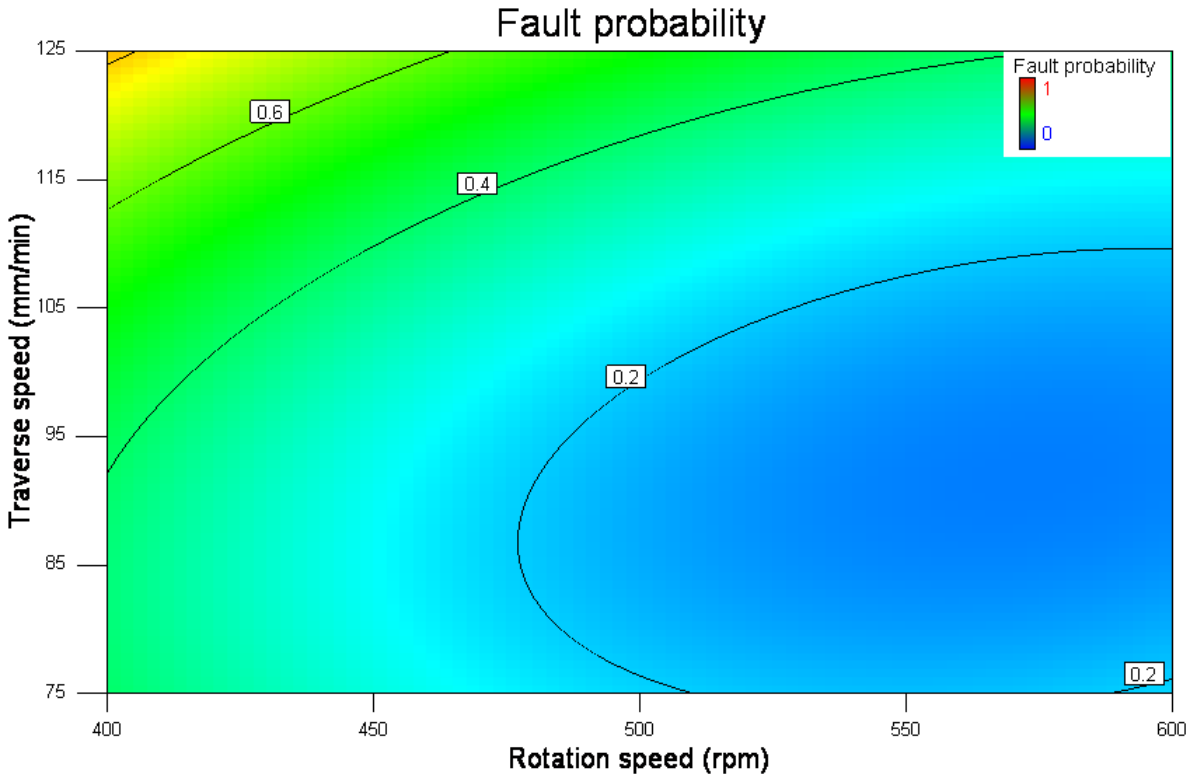

Figure 5.59: Probability of imperfection contour graphic.

The color in red indicates a probability near to 100% imperfections and blue indicates a probability near to 0%. The contour surface shows that when the rotation speed is high and the traversing speed is low, then the probability is near to 0%. In contrast, when there are low rotation speed and high traversing speed then the probability was near to 100%.

6 Conclusion

The principal idea of this research was the determination of an imperfection pattern by using computational intelligent tools, such as fuzzy logic and artificial neural networks, for the FSW process of the aluminum alloy 5052-H32. For that reason, the process was analyzed experimentally using the sensors signals of the welding machine to understand its dynamic and behavior.

When the signal is analyzed by the STFT using the standard sample rate (10 Hz) of the FSW machine, it is possible to identify some patterns for a good and a bad welding. The process was also monitoring using in the same operational parameters, with a DAQ system at a sample rate of 100 Hz to improve the resolution of frequency and time. The STFT was used for the signals of the tool forces and spindle torque spectrum variation (the forces and torque frequency analysis). Due to the resulting analysis of the experimental data of the tool forces and spindle torque spectrum variation, it is clear that is necessary to consider the four variables (down force, traversing force, side force and spindle torque).

The spectrogram of the traversing force, F_x, shows effectively the occurrence of imperfections during the welding. However, the imperfection detection by the amplitude spectrum of F_x is not accurate, as shown in the Case 3 where the spectrum didn't have components in the region of low frequency (0 to 2.5 Hz). As a consequence, a detection system that only considers these variables may neglect some imperfections.

This is also a problem if it is considered the down force, F_z, and the spindle torque. These variables present limitations in the detection because they have a dependency of the penetration depth. In cases where the penetration depth reaches 2.1 mm, these two variables did not exhibit high peaks (for the F_z, greater than 140 dB and for the torque, greater than 85 dB) of intensity in the low frequency, what may suggest that there is not an imperfection in the welding. In contrast, the F_x and F_y exhibited low-frequency components, suggesting an imperfection (greater than 135 dB). These differences may be given by a low contact with the tool shoulder, decreasing intensity of both variables.

Researchers like Boldsaikhan et al. (2011b) and Ferlin (2012) discussed the information that the spectrum of the vibrations and forces during the FSW process, and related this to the imperfection detection. During the current research another important variable, the spindle torque spectrum has shown that this could add relevant information for the imperfection detection. The study of the spindle torque spectrum for FSW process, in particular, is one of the main points of this research.

To the knowledge of this author, this is the first work to consider the torque spectrum

and its relevancy. During this research, it is seen that under the right conditions, the spindle torque offers valuable information when an imperfection occurs during the process. This research also intends to relate the input parameters (the tool rotation speed, traversing speed, the tool penetration depth) with the output (forces and torque spectrum) using a nonlinear model to determine if there are imperfections in the weld joint.

On the other hand, an ANN dynamic model was made to understand how the operational tool rotation speed, the traversing speed, the penetration depth, the tool forces, torque and temperature values interact dynamically. Based on this result, a nonlinear model was developed using an ANN with Bayesian modification of the Levenberger-Marquardt training algorithm. The model included all stages of the process and a good fitting to the real data was verified. This fact was corroborated by the correlation coefficients, which in this case were near to 99% for all data. The model presented a close response the real response and when the model was tested with non-training data, the response of the model was close to the real data. The error of the model was under the limits established in the experiment. To the author's knowledge, this is the first nonlinear dynamic model relating the tool rotation speed, traversing speed and penetration depth with the spindle torque, the tool down force and the temperature.

With the STFT (the spectrogram) data, a fuzzy logic system was implemented to identify the probability of defects occurrence. The fuzzy system used the bigger peaks on the lower frequency interval of every variable (forces and torque spectrum). Rules were created using the information of the experiments to identify properly where imperfections occur. The fuzzy system detected the occurrence of the imperfection successfully and was validated by a microscopy analysis. A statistical analysis (ANOVA) was made using operational points (the tool rotation speed, traversing speed, the tool penetration depth) where the imperfection occurs to establish the relationship between input parameters and the probability of imperfection.

The statistical analysis shows that all input parameters are significant and there were significant nonlinear terms related to the traverse speed. The plunge penetration depth is the most relevant input parameter. The lower levels of penetration depth (1.95 and 2.1 mm) produced the vast majority of the imperfections in the experiment. The relation between the tool rotation speed and traversing speed is another important parameter to take into account. The process shows a better behavior when the rotation speed was near to 600 rpm and the traverse speed was 75 mm/min. In contrast, the worst results were obtained at a tool rotation speed of 400 and traversing speed of 125 mm/min.

For future work, the comparison between this detection system and other flaw test meth-

ods, such as X-ray or ultrasonic test, will help to validated other results. The validation will focus on the sensibility of the fuzzy system to detect the defects in relation to other tests, that could help to adjust the fuzzy logic system to a better performance.

The ANN model can be used for the design of a control system and for numerical models verification, for example, using the finite element method.

One aspect that could also be a result of this research is the exploration of the operational parameters, especially the rotational speed and the traverse speed, in the high-speed region. The imperfection detection system will help to optimize the operational parameters in that region. This process can be initiated by using the response surface given in this research. Additional tests and experiments will be required for this analysis.

The FSW process for steel, that was not covered in this current research, could be also of interest because the detection defects system was previously tested to steel welding and show similar imperfection patterns. Another aspect that could be covered for a future research is to evaluate the detection system for other types of welding geometries like pipes and plates with a major thinness. Another field that could be considered for future research is to explore the imperfection patterns in dissimilar welding so that further information will be required.

References

M.J. Anderson and P.J. Whitcomb. *DOE Simplified: Practical Tools for Effective Experimentation, Third Edition*. CRC Press, 2015. ISBN 9781498760331. URL https://books.google.com.br/books?id=_5soCwAAQBAJ.

W.J. Arbegast. Modeling friction stir joining as a metalworking process. *Proceedings of Hot Deformation of Aluminum Alloys III*, pages 313–327, 2003.

D.R. Askeland, F. Haddleton, P. Green, and H. Robertson. *The Science and Engineering of Materials*. Springer US, 2013. ISBN 9781489928955. URL https://books.google.com.co/books?id=CIIiBAAAQBAJ.

ASTM. E2700-14 standard practice for contact ultrasonic testing of welds using phased arrays, 2014. URL http://www.astm.org.

A. Bachmann and M.F. Zaeh. Pyrometer-assisted temperature control in friction stir welding. In *11th International Symposium on Friction Stir Welding, Cambridge, UK, 17-19 May, 2016*, pages 21–39, 2016.

A. Baraka, G. Panoutsos, and S. Cater. A real-time quality monitoring framework for steel friction stir welding using computational intelligence. *Journal of Manufacturing Processes*, 20, Part 1:137 – 148, 2015. ISSN 1526-6125. doi: http://dx.doi.org/10.1016/j.jmapro.2015.09.001. URL http://www.sciencedirect.com/science/article/pii/S152661251500095X.

E. Boldsaikhan and M. McCoy. *Analysis of Tool Feedback Forces and Material Flow during Friction Stir Welding*, pages 311–320. John Wiley & Sons, Inc., 2013. ISBN 9781118658345. doi: 10.1002/9781118658345.ch32. URL http://dx.doi.org/10.1002/9781118658345.ch32.

E. Boldsaikhan, D.A. Burford, and P.J. Gimenez Britos. *Effect of Plasticized Material Flow on the Tool Feedback Forces during Friction Stir Welding*, pages 333–343. John Wiley & Sons, Inc., 2011a. ISBN 9781118062302. doi: 10.1002/9781118062302.ch39. URL http://dx.doi.org/10.1002/9781118062302.ch39.

E. Boldsaikhan, E.M. Corwin, A.M. Logar, and W.J. Arbegast. The use of neural network and discrete fourier transform for real-time evaluation of friction stir welding. *Applied Soft Computing*, 11(8):4839 – 4846, 2011b. ISSN 1568-4946. doi: http://dx.doi.org/10.1016/j.asoc.2011.06.017. URL http://www.sciencedirect.com/science/article/pii/S1568494611002559.

G. Buffa, L. Donati, L. Fratini, and L. Tomesani. Solid state bonding in extrusion and fsw: Process mechanics and analogies. *Journal of Materials Processing Technology*, 177(1-3):344 – 347, 2006. ISSN 0924-0136. doi: http://dx.doi.org/10.1016/j.jmatprotec.2006.04.042. URL http://www.sciencedirect.com/science/article/pii/S0924013606004171. Proceedings of the 11th International Conference on Metal Forming 2006.

D. Burford, E. Boldsaikhan, and A. Wiley. Early detection of volumetric defects using e-nde during friction stir welding. In *9th International Friction Stir Welding Symposium. The Von Braun Center, Huntsville, Alabama*, 2012.

Z.W. Chen, T. Pasang, Y. Qi, and R. Perris. Tool-workpiece interface and shear layer formed during friction stir welding. In *TWI Conference paper, Montreal, Canada*, 2006.

T.A. Davis, Shin Y.C., and B. Yao. Observer-based adaptive robust control of friction stir welding axial force. *Mechatronics, IEEE/ASME Transactions on*, 16(6):1032–1039, Dec 2011. ISSN 1083-4435. doi: 10.1109/TMECH.2010.2071417.

H. Demuth and M. Beale. Neural network toolbox for use with matlab, user's guide verion 3.0, 1993.

A.S. Ferlin. Monitoramento do processo de junção por friction stir welding para detecção de falhas. Master's thesis, Faculdade de Engenharia Mecânica, Universidade Estadual de Campinas, Campinas, 2012. URL http://www.bibliotecadigital.unicamp.br/document/?code=000914125&opt=4.

R. Fischman. The phase vocoder: Theory and practice. *Org. Sound*, 2(2):127–145, August 1997. ISSN 1355-7718. doi: 10.1017/S1355771897009060. URL http://dx.doi.org/10.1017/S1355771897009060.

F. Dan Foresee and M. T. Hagan. Gauss-newton approximation to bayesian learning. In *International Conference on Neural Networks,1997.*, volume 3, pages 1930–1935 vol.3, Jun 1997. doi: 10.1109/ICNN.1997.614194.

J.C. GALVIS PEREZ. AvaliaÇ ao do processo de deposiÇ ao superficial por atrito em liga de aluminio aa6351-t6 sobre substrato de liga de aluminio aa5052-h32. Master's thesis, Programa de Engenharia Ciências de Materiais , Universidade Estadual de Ponta Grossa, Campinas, 2016.

B.T. Gibson, D.H. Lammlein, T.J. Prater, W.R. Longhurst, C.D. Cox, Ballun M.C., K.J. Dharmaraj, G.E. Cook, and A.M. Strauss. Friction stir welding: Process, automation, and control. *Journal of Manufacturing Processes*, 16(1):56 – 73, 2014. ISSN 1526-6125. doi: http://dx.doi.org/10.1016/j.jmapro.2013.04.002. URL http://www.sciencedirect.com/science/article/pii/S1526612513000601.

S.S. Haykin. *Neural Networks and Learning Machines*. Number v. 10 in Neural networks and learning machines. Prentice Hall, 2009. ISBN 9780131471399. URL https://books.google.com.br/books?id=K7P36lKzI_QC.

F. Hlawatsch and F. Auger. *Time-frequency Analysis: Concepts and Methods*. Digital signal and image processing series. ISTE, 2008. ISBN 9781905209149. URL https://books.google.co.ve/books?id=W0DpAAAACAAJ.

Hwei P. Hsu. *Schaum's Outline of Theory and Problems of Signals and Systems*. McGraw-Hill, New York, NY, 1995. ISBN 0585267316 9780585267319.

Paul Kah, Richard Rajan, Jukka Martikainen, and Raimo Suoranta. Investigation of weld defects in friction-stir welding and fusion welding of aluminium alloys. *International Journal of Mechanical and Materials Engineering*, 10(1):26, Dec 2015. ISSN 2198-2791. doi: 10.1186/s40712-015-0053-8. URL https://doi.org/10.1186/s40712-015-0053-8.

S.W. Kallee, E.D. Nicholas, and W.M. Thomas. Friction stir welding: invention, innovations and industrialization. In *Reibrührschweißen, 2. GKSS Workshop*, pages 22–23, 2002.

T. Khaled. An Outsider Looks at Friction Stir Welding. Technical report, 2005. URL http://faa.gov/aircraft/air_cert/design_approvals/csta/publications/media/friction_stir_welding.pdf.

C. C. Lee. Fuzzy logic in control systems: fuzzy logic controller. I. *IEEE Transactions on Systems, Man, and Cybernetics*, 20(2):404–418, Mar 1990. ISSN 0018-9472. doi: 10.1109/21.52551.

D. Lohwasser and Z. Chen. *Friction Stir Welding: From Basics to Applications*. Woodhead Publishing Series in Welding and Other Joining Technologies. Elsevier Science, 2009. ISBN 9781845697716. URL https://books.google.com.br/books?id=FKmjAgAAQBAJ.

D.J.C. MacKay. Bayesian interpolation. *Journal of Neural Computation*, 4:415–447, 1991.

P.L. Mangonon. *The Principles of Materials Selection for Engineering Design*. Prentice Hall, 1999. ISBN 9780132425957. URL https://books.google.com.co/books?id=caoeAQAAIAAJ.

MathWorks. *Fuzzy Logic Toolbox for Use with MATLAB*. Computation, visualization, programming. MathWorks, 2001. URL https://books.google.com.br/books?id=

soMZAQAAIAAJ.

R.S. Mishra and Z.Y. Ma. Friction stir welding and processing. *Materials Science and Engineering: R: Reports*, 50(1):1 – 78, 2005. ISSN 0927-796X. doi: http://dx.doi.org/10.1016/j.mser.2005.07.001. URL http://www.sciencedirect.com/science/article/pii/S0927796X05000768.

R.S. Mishra and H. Sidhar. *Friction Stir Welding of 2XXX Aluminum Alloys including Al-Li Alloys*. Friction Stir Welding and Processing. Elsevier Science, 2016. ISBN 9780128092927. URL https://books.google.com.br/books?id=kcjPCwAAQBAJ.

D.C. Montgomery. *Design and Analysis of Experiments*. John Wiley & Sons, 2008. ISBN 9780470128664. URL https://books.google.com.br/books?id=kMMJAm5bD34C.

R. Nandan, T. DebRoy, and H.K.D.H. Bhadeshia. Recent advances in friction stir welding process weldment structure and properties. *Progress in Materials Science*, 53(6):980 – 1023, 2008. ISSN 0079-6425. doi: http://dx.doi.org/10.1016/j.pmatsci.2008.05.001. URL http://www.sciencedirect.com/science/article/pii/S007964250800039X.

M. Natrella. *NIST/SEMATECH e-Handbook of Statistical Methods*. NIST/SEMATECH, July 2010. URL http://www.itl.nist.gov/div898/handbook/.

O. Nelles. *Nonlinear System Identification: From Classical Approaches to Neural Networks and Fuzzy Models*. Engineering online library. Springer Science & Business Media, 2001. ISBN 9783540673699. doi: 10.1007/978-3-662-04323-3. URL http://dx.doi.org/10.1007/978-3-662-04323-3.

T. Nelson, C. Sorensen, and B. Stringhan. Essential variables for controlling post-weld microstructure and properties in friction stir welding. In *11th International Symposium on Friction Stir Welding, Cambridge, UK, 17-19 May, 2016*, pages 40–46, 2016.

D. Nguyen and B. Widrow. Improving the learning speed of 2-layer neural networks by choosing initial values of the adaptive weights. In *Neural Networks, 1990., 1990 IJCNN International Joint Conference on*, pages 21–26 vol.3, June 1990. doi: 10.1109/IJCNN.1990.137819.

P. M. Nørgård, O. Ravn, N.K. Poulsen, and L.K. Hansen. *Neural Networks for Modelling and Control of Dynamic Systems-A Practitioner's Handbook*. Springer-London, 1st edition, 2000. ISBN 1852332271.

T. Oakes and R.G. Landers. Design and implementation of a general tracking controller for friction stir welding processes. In *American Control Conference, 2009. ACC '09.*, pages 5576–5581, June 2009. doi: 10.1109/ACC.2009.5160405.

A.V. Oppenheim and R.W. Schafer. *Discrete-time Signal Processing*. Prentice-Hall signal processing series. Pearson, 2010. ISBN 9780132067096. URL https://books.google.com.br/books?id=5vajQAAACAAJ.

P. Podrzaj, B. Jerman, and D. Klobcar. Welding defects at friction stir welding. *Metalurgija*, 54(2):387 – 389, 2015. ISSN 0543-5846. URL http://hrcak.srce.hr/128969.

T.F. Quatieri. *Discrete-time Speech Signal Processing: Principles and Practice*. Prentice-Hall signal processing series. Prentice Hall PTR, 2002. ISBN 9780132429429. URL https://books.google.com.br/books?id=5KYeAQAAIAAJ.

R. Rai, A. De, H. K. D. H. Bhadeshia, and T DebRoy. Review: friction stir welding tools. *Science and Technology of Welding and Joining*, 16(4):325–342, 2011. doi: 10.1179/1362171811Y.0000000023. URL http://dx.doi.org/10.1179/1362171811Y.0000000023.

K. Ross and C. Sorensen. *Paradigm Shift in Control of the Spindle Axis*, pages 321–328. Springer International Publishing, Cham, 2016a. ISBN 978-3-319-48108-1. doi: 10.1007/978-3-319-48108-1_33. URL http://dx.doi.org/10.1007/

978-3-319-48108-1_33.

K. Ross and C. Sorensen. *Advances in Temperature Control for friction stir processing (FSP)*, pages 301–310. Springer International Publishing, Cham, 2016b. ISBN 978-3-319-48108-1. doi: 10.1007/978-3-319-48108-1_31. URL http://dx.doi.org/10.1007/978-3-319-48108-1_31.

Kenneth Ross and Carl Sorensen. *Paradigm Shift in Control of the Spindle Axis*, pages 321–328. John Wiley & Sons, Inc., 2013. ISBN 9781118658345. doi: 10.1002/9781118658345.ch33. URL http://dx.doi.org/10.1002/9781118658345.ch33.

H.N. Schmidt and J. Hattel. CFD modelling of the shear layer around the tool probe in friction stir welding. *Friction Stir Welding and Processing*, 2005.

J.A. Schneider and A.C. Nunes. Characterization of plastic flow and resulting microtextures in a friction stir weld. *Metallurgical and materials transactions B*, 35(4):777–783, 2004.

A. Shrivastava, M. Krones, and F.E. Pfefferkorn. Comparison of energy consumption and environmental impact of friction stir welding and gas metal arc welding for aluminum. *CIRP Journal of Manufacturing Science and Technology*, 9:159 – 168, 2015a. ISSN 1755-5817. doi: http://dx.doi.org/10.1016/j.cirpj.2014.10.001. URL http://www.sciencedirect.com/science/article/pii/S1755581714000467.

A. Shrivastava, M. Overcash, and F.E. Pfefferkorn. Prediction of unit process life cycle inventory (UPLCI) energy consumption in a friction stir weld. *Journal of Manufacturing Processes*, 18:46 – 54, 2015b. ISSN 1526-6125. doi: http://dx.doi.org/10.1016/j.jmapro.2014.10.006. URL http://www.sciencedirect.com/science/article/pii/S1526612514000929.

A. Silva, J. De Backer, and G. Bolmsjö. Analysis of plunge and dwell parameters of robotic fsw using twt temperature feedback control. In *11th International Symposium on Friction Stir Welding, Cambridge, UK, 17-19 May, 2016*, pages 1–11, 2016.

J.A.K. Suykens, J.P.L. Vandewalle, and B.L. de Moor. *Artificial Neural Networks for Modelling and Control of Non-Linear Systems*. Springer Science & Business Media, 2012. ISBN 9781475724936. doi: 10.1007/978-1-4757-2493-6. URL http://dx.doi.org/10.1007/978-1-4757-2493-6.

W.M. Thomas, M.G. Murch, E.D. Nicholas, P. Temple-Smith, J.C. Needham, and C.J. Dawes. Improvements relating to friction welding, May 17 1995. URL http://www.google.com/patents/EP0653265A2?cl=en. EP Patent App. EP19,940,120,385.

W.M. Thomas, P.L. Threadgill, and E.D. Nicholas. Feasibility of friction stir welding steel. *Science and Technology of Welding and Joining*, 4(6):365–372, 1999. doi: 10.1179/136217199101538012. URL https://doi.org/10.1179/136217199101538012.

P. L. Threadgill. Terminology in friction stir welding. *Science and Technology of Welding and Joining*, 12(4):357–360, 2007. doi: 10.1179/174329307X197629. URL https://doi.org/10.1179/174329307X197629.

Z. Xin, P. Kalya, R.G. Landers, and K. Krishnamurthy. Design and implementation of a nonlinear axial force controller for friction stir welding processes. In *American Control Conference, 2007. ACC '07*, pages 5553–5558, July 2007. doi: 10.1109/ACC.2007.4282731.

L.A. Zadeh. Fuzzy sets. *Information and Control*, 8(3):338 – 353, 1965. ISSN 0019-9958. doi: http://dx.doi.org/10.1016/S0019-9958(65)90241-X. URL http://www.sciencedirect.com/science/article/pii/S001999586590241X.

M.F. Zaeh and P. Gebhard. Dynamical behaviour of machine tools during friction stir welding. *Production Engineering*, 4(6):615–624, 2010. ISSN 0944-6524. doi: 10.1007/s11740-010-0273-y. URL http://dx.doi.org/10.1007/s11740-010-0273-y.

Fu Zhi-hong, He Di-qiu, and Wang Hong. Friction stir welding of aluminum alloys. *Journal of Wuhan University of Technology-Mater. Sci. Ed.*, 19(1):61–64, Mar 2004. ISSN 1993-

0437. doi: 10.1007/BF02838366. URL https://doi.org/10.1007/BF02838366.

ANNEX A Matlab Codes

A.1 Code ANN training algorithm

This is the algorithm used in Matlab for training and verifying the NARX model.

```
clc
clear
load inout9
in=[in(:,1) in(:,2) in(:,3) in(:,5)];
%out=[out(:,3) out(:,4) out(:,5)];
[A N]=size(in);
M=size(out);
M=M(2);
inmod=in;
outmod=out;
B=size(inmod);
in2=in;
out2=out;
%% treino da rede
in3=tonndata(in2,false,false);
out3=tonndata(out2,false,false);
net1=narxnet(1:5,1:5,10,'open','trainbr');
net1.layers{2}.transferFcn = 'tansig';
net1.divideFcn= 'divideint';
net1.performParam.normalization= 'standard';
net1=closeloop(net1);
[Xs,Xi,Ai,Ts] = preparets(net1,in3,{},out3);
net1.trainParam.epochs=100;
net1=initnw(net1,1);
net1=initnw(net1,2);
[net1,tr]=train(net1,Xs,Ts,Xi,Ai,'useParallel','yes');
out4=net1(in3,Xi,Ai);
trout=out4(tr.trainInd);
trtarg=out3(tr.trainInd);
vout=out4(tr.valInd);
```

```
vtarg=out3(tr.valInd);
tsout=out4(tr.testInd);
tstarg=out3(tr.testInd);
Y=net1(Xs,Xi,Ai);
out5=fromnndata(out4,true,false,false);
out6=out5;
time=[0:0.1:(B(1)-1)*0.1];
E=gsubtract(out4,out3);
figure (1)
plot(time,[out6(:,1) outmod(:,1)])
figure (2)
plot(time,[out6(:,2) outmod(:,2)])
figure (3)
plot(time,[out6(:,3) outmod(:,3)])
figure (4)
plotperf(tr)
figure (5)
plotregression(trtarg,trout,'Train',tstarg,tsout,'Testing')
figure (6)
plotresponse(Ts,Y)
figure (7)
plotinerrcorr(in3,E)
```

A.2 Code used to evaluated the NARX model

This algorithm compares the real signals of the process and the NARX model.

```
clear all
%load newmodel10
load modelo10_10_27;
load val10;
in3=[in3(:,2) in3(:,3) in3(:,5)];
%out3=[out3(:,1) out3(:,2)];
%load inoutnew1;
[out7 outmod1 time] = pruebanet1(in3,out3,in,out,net1,Xi,Ai);
figure (1)
```

```
subplot(3,1,3),plot(time,[out7(:,3) outmod1(:,3)])
subplot(3,1,2),plot(time,[out7(:,2) outmod1(:,2)])
subplot(3,1,1),plot(time,[out7(:,1) outmod1(:,1)])
clear all
load modelo10_10_27;
load val11;
in3=[in3(:,2) in3(:,3) in3(:,5)];
%out3=[out3(:,1) out3(:,2)];
[out9 outmod2 time] = pruebanet1(in3,out3,in,out,net1,Xi,Ai);
figure (2)
subplot(3,1,3),plot(time,[out9(:,3) outmod2(:,3)])
subplot(3,1,2),plot(time,[out9(:,2) outmod2(:,2)])
subplot(3,1,1),plot(time,[out9(:,1) outmod2(:,1)])
clear all
load modelo10_10_27;
load val12;
in3=[in3(:,2) in3(:,3) in3(:,5)];
%out3=[out3(:,1) out3(:,2)];
[out8 outmod3 time] = pruebanet1(in3,out3,in,out,net1,Xi,Ai);
figure (3)
subplot(3,1,3),plot(time,[out8(:,3) outmod3(:,3)])
subplot(3,1,2),plot(time,[out8(:,2) outmod3(:,2)])
subplot(3,1,1),plot(time,[out8(:,1) outmod3(:,1)])
```

A.3 Code used in the machine data recording

This code records the data of the lateral and traverse forces to calculate the spectrogram of these two variables.The sample rate of (10 samples per seconds) and a window of 5 seconds were used in this code.

```
clear all
clc
load sample14
z1=0;
F=A(:,1);%Fx(790:5629);
```

```
Fy=A(:,2);%Fy(790:5629);
Fz=A(:,3);%Fz(790:5629);
Ts=0.1;
Fs=1/Ts;
T=50;
freq=Fs*(0:((T+z1)/2)-1)/(T+z1);
index=200/(60*Fs/T);
L=size(F);
L=L(1)+0;
w=kaiser(T,0);
k=1;
z=0;
u=0;
v=0;
B=F(1:T);
TRF=fft(B.*w,T);
TRF=TRF/index;
TRF=fftshift(TRF);
M(k,:)=abs(TRF);
P1(k,:)=M(k,(T+z1)/2+1:end);
for  j=T/2:T/2:L
     if  j+T<L
     k=k+1;
     B=F(j:T+j-1);
     TRF=fft(B.*w,T+z1);
     TRF=TRF/index;
     TRF=fftshift(TRF);
     M(k,:)=abs(TRF);
     P1(k,:)=M(k,(T+z1)/2+1:end);
     else
          break
     end
end
z=z+1;
```

```
B1=Fy(1:T);
TRF1=fft(B1.*w,T);
TRF1=TRF1/index;
TRF1=fftshift(TRF1);
M1(z,:)=abs(TRF1);
P2(z,:)=M1(z,(T+z1)/2+1:end);
for j=T/2:T/2:L
    if j+T<L
    z=z+1;
    B1=Fy(j:T+j-1);
    TRF1=fft(B1.*w,T+z1);
    TRF1=TRF1/index;
    TRF1=fftshift(TRF1);
    M1(z,:)=abs(TRF1);
    P2(z,:)=M1(z,(T+z1)/2+1:end);
    else
        break
    end
end
u=u+1;
B2=Fz(1:T);
TRF2=fft(B2.*w,T);
TRF2=TRF2/index;
TRF2=fftshift(TRF2);
M2(u,:)=abs(TRF2);
P3(u,:)=M2(u,(T+z1)/2+1:end);
for j=T/2:T/2:L
    if j+T<L
    u=u+1;
    B2=Fz(j:T+j-1);
    TRF2=fft(B2.*w,T+z1);
    TRF2=TRF2/index;
    TRF2=fftshift(TRF2);
    M2(u,:)=abs(TRF2);
```

```
    P3(u,:)=M2(u,(T+z1)/2+1:end);
    else
        break
    end
end


time=[0:(T/2)/10:(k-1)*(T/2)/10];
SFx=figure (1)
contourf(time,freq(2:end),P1(:,2:end)');
colorbar
title('Force in X')
ylabel('Frequency (Hz)')
xlabel('Time (sec)')
saveas(SFx,'SFx.png')
SFy=figure (2)
time0=[0:(T/2)/10:(z-1)*(T/2)/10];
contourf(time0,freq(2:end),P2(:,2:end)')
colorbar
title('Force in Y')
ylabel('Frequency (Hz)')
xlabel('Time (sec)')
saveas(SFy,'SFy.png')
SFz=figure (3)
time1=[0:(T/2)/10:(u-1)*(T/2)/10];
contourf(time1,freq(2:end),P3(:,2:end)')
colorbar
title('Force in Z')
ylabel('Frequency (Hz)')
xlabel('Time (sec)')
times=[0:(T/2)/10:(z-1)*(T/2)/10];
saveas(SFz,'SFz.png')
```

A.4 Algorithm using the DAQ data

This algorithm uses the tool forces and torque signals to make the spectrogram and the fuzzy logic system detection. In this case the window is 2 seconds and the sample rate is 100 sample per second.

```
clear all
clc
%load Falu
%F=Fxal;
load run3
load fuz
SpindleLoadCellDist=114;
LoadCellRadius=210;
ToolLength=200;
m=size(A);
m=m(1);
z1=0;
AZForce=A(:,1)*((32767+32768)/20)*(-1.94)+29.1;
BZForce=A(:,2)*((32767+32768)/20)*(-2.04)+42.84;
CZForce=A(:,3)*((32767+32768)/20)*(-2.19)+65.7;
Fx=(-1)*(LoadCellRadius/(ToolLength+SpindleLoadCellDist))*(
    AZForce-(BZForce/2)-(CZForce/2));
Fy=(LoadCellRadius/(ToolLength+SpindleLoadCellDist))*((
    BZForce-CZForce)*0.866025);
Fz=AZForce+BZForce+CZForce;
Tor=A(:,4)/0.009057;
F=Fx;
Ts=0.01;
Fs=1/Ts;
T=200;
t=50;
freq=Fs*(0:((T)/2)-1)/(T);
L=size(F);
L=L(1)+0;
index=1/200; %300/(60*Fs/T);
```

```
w=kaiser(200,0);
k=0;
z=0;
u=0;
v=0;
k=k+1;
B=F(1:T);
TRF=fft(B.*w,T);
TRF=TRF/index;
TRF=fftshift(TRF);
M(k,:)=mag2db(abs(TRF));
P1(k,:)=M(k,(T+z1)/2+1:end);
for  j=T/2:T/2:L
     if  j+T<L
     k=k+1;
     B=F(j:T+j-1);
     TRF=fft(B.*w,T+z1);
     TRF=TRF/index;
     TRF=fftshift(TRF);
     M(k,:)=mag2db(abs(TRF));
     P1(k,:)=M(k,(T+z1)/2+1:end);
     else
     break
     end
end
z=z+1;
B1=Fy(1:T);
TRF1=fft(B1.*w,T);
TRF1=TRF1/index;
TRF1=fftshift(TRF1);
M1(z,:)=mag2db(abs(TRF1));
P2(z,:)=M1(z,(T)/2+1:end);
for  j=T/2:T/2:L
     if  j+T<L
```

```
        z=z+1;
        B1=Fy(j:T+j-1);
        %TRF1=fft(B1,T+z1);
        TRF1=fft(B1.*w,T);
        TRF1=TRF1/index;
        TRF1=fftshift(TRF1);
        M1(z,:)=mag2db(abs(TRF1));
        P2(z,:)=M1(z,(T)/2+1:end);
        else
            break
        end
end
u=u+1;
B2=Fz(1:T);
TRF2=fft(B2.*w,T);
TRF2=TRF2/index;
TRF2=fftshift(TRF2);
M2(u,:)=mag2db(abs(TRF2));
P3(u,:)=M2(u,(T)/2+1:end);
for  j=T/2:T/2:L
        if  j+T<L
        u=u+1;
        B2=Fz(j:T+j-1);
        %TRF2=fft(B2,T+z1);
        TRF2=fft(B2.*w,T+z1);
        TRF2=TRF2/index;
        TRF2=fftshift(TRF2);
        M2(u,:)=mag2db(abs(TRF2));
        P3(u,:)=M2(u,(T+z1)/2+1:end);
        else
            break
        end
end
v=v+1;
```

```
B3=Tor(1:T);
TRF3=fft(B3.*w,T);
TRF3=TRF3/index;
TRF3=fftshift(TRF3);
M3(v,:)=mag2db(abs(TRF3));
P4(v,:)=M3(v,(T)/2+1:end);
for j=T/2:T/2:L
    if j+T<L
    v=v+1;
    B3=Tor(j:T+j-1);
    %TRF3=fft(B3,T+z1);
    TRF3=fft(B3.*w,T);
    TRF3=TRF3/index;
    TRF3=fftshift(TRF3);
    M3(v,:)=mag2db(abs(TRF3));
    P4(v,:)=M3(v,(T)/2+1:end);
    else
        break
    end
end
Dout = evalfis([max(P1(:,2:9)');max(P2(:,2:9)');max(P3(:,2:9)
    )');max(P4(:,2:9)');],detect);
time=[0:(T/2)/100:(k-1)*(T/2)/100];
%surf(freq(2:end),time,P1(:,2:end))
SFx=figure(1)
contourf(time,freq(2:end),P1(:,2:end)');
colorbar
title('Force in X')
ylabel('Frequency (Hz)')
xlabel('Time (sec)')
saveas(SFx,'SFx.fig')
SFy=figure(2)
contourf(time,freq(2:end),P2(:,2:end)')
colorbar
```

```
title('Force in Y')
ylabel('Frequency (Hz)')
xlabel('Time (sec)')
saveas(SFy,'SFy.fig')
SFz=figure (3)
time1=[0:(T/2)/100:(u-1)*(T/2)/100];
contourf(time1,freq(2:end),P3(:,2:end)')
colorbar
title('Force in Z')
ylabel('Frequency (Hz)')
xlabel('Time (sec)')
times=[0:(T/2)/100:(z-1)*(T/2)/100];
saveas(SFz,'SFz.fig')
ST=figure (4)
contourf(time,freq(2:end),P4(:,2:end)')
colorbar
title('Spindle Torque')
ylabel('Frequency (Hz)')
xlabel('Time (sec)')
saveas(ST,'ST.fig')
SR=figure (5)
plot(time,Dout)
title('Fault Probability')
ylabel('Probability')
xlabel('Time (sec)')
```

ANNEX B Aluminum Alloys

Aluminum is considered the most abundant metal in the earth's crust, is part of 8% of it and is found in nature forming aluminum compounds. Its main source of extraction is bauxite, a mineral composed mostly of hydrated aluminum oxides and to a lesser extent by iron oxide and silica. A certain amount of bauxite is used for metallurgical processes (aluminum production) and another part for non-metallurgical processes (production of refractories, among other products) (ASKELAND ET AL., 2013). The aluminum production process consists of extraction of the bauxite, the transformation of the bauxite into alumina, the transformation or refining of the aluminum alumina and the processing of the aluminum (rolling, extrusion, casting, etc.) according to the final use of the product (ASKELAND ET AL., 2013). The mechanical, physical and chemical properties of this element are presented in Table B.1.

Table B.1: Properties of Pure aluminum

<table>
<tr><th colspan="2">Physical Properties</th><th colspan="2">Chemical Properties</th><th>Mechanical Properties</th></tr>
<tr><td>Appearance</td><td>White-silver</td><td>Symbol</td><td>Al</td><td rowspan="2">Tensile strength
60-70 MPa</td></tr>
<tr><td>Crystallographic structure</td><td>FCC</td><td>Atomic number</td><td>13</td></tr>
<tr><td>Melting point</td><td>660.2 ° C</td><td>Valence Electron</td><td>3</td><td>Hardness
20 - 44 HV</td></tr>
<tr><td>Density</td><td>2,699 g /cm ^3</td><td rowspan="2">Corrosion resistance</td><td rowspan="2">High</td><td rowspan="3">Poisson module

0.3</td></tr>
<tr><td>Thermal conductivity</td><td>High</td></tr>
<tr><td>Electric conductivity</td><td>High</td><td>Atomic mass</td><td>26.98 g / mol</td></tr>
</table>

This metal is widely used in the manufacture of airplanes, railroads, ships, among others, due to the improvement of its properties when alloying it with certain elements such as magnesium, copper, silicon, manganese, among others (MANGONON, 1999).

B.1 Classification of aluminum alloys

Aluminum alloys are those that arise from the need to improve the properties of pure aluminum to expand its field of application. Generally, these alloys are composed of a main alloying element and several secondary alloying elements, responsible for generating their own characteristics in each alloy.

Like all alloys, aluminum alloys must have a classification that allows their identification. In this way, we find that they can be classified as follows (MANGONON, 1999):

- According to your process.
- According to the main alloy element.
- According to your state.

The classification of aluminum alloys according to their process, are determined by the manufacturing mode with which it is generated. Thus, we can find alloys for forging and casting alloys (ASKELAND ET AL., 2013).

The aluminum alloys for forging are those that obtain their properties by plastic deformation and are characterized by having a microstructure significantly different from those obtained by casting. Aluminum alloys for foundry are those that show good fluidity and are formed mainly in processes of sand casting, in permanent mold or mold casting (MANGONON, 1999).

Each of the groups mentioned are divided into two subgroups that are:

- Heat-treatable aluminum alloys: These alloys are generally hardened by an aging heat treatment, which can be artificial or natural.
- Non-heat-treatable aluminum alloys: These are alloys that can not be hardened by precipitation and are only cold worked to increase their strength.

Table B.2 and Table B.3 show the classification of aluminum alloys according to their process, the main alloy type and the applied hardening method.

Table B.2: Classification of aluminum alloys for forging according to their main alloy and hardening method (MANGONON, 1999).

Forging Alloys	**Principal Alloy**	**Hardening method**
1xxx	99% Al	Non-Precipitation hardening
2xxx	Al-Cu and Al-Cu-Li	Precipitation hardening
3xxx	Al-Mn	Non-Precipitation hardening
4xxx	Al-Si or Al-Mg-Si	Precipitation hardening, if the Mg is present
5xxx	Al-Mg	Non-Precipitation hardening
6xxx	Al-Mg-Si	Precipitation hardening
7xxx	Al-Mg-Zn	Precipitation hardening
8xxx	Al-Li, Sn, Zr or B	Precipitation hardening

Table B.3: Classification of aluminum alloys for cast iron according to its main alloy and hardening method (MANGONON, 1999).

Casting Alloys	**Principal Alloy**	**Hardening method**
1xxx	Pure Aluminium	Non-Precipitation hardening
2xxx	Al-Cu	Precipitation hardening
3xxx	Al-Si-Cu o Al-Mg-Si	Some are hardening by precipitation
4xxx	Al-Si	Non-Precipitation hardening
5xxx	Al-Mg	Non-Precipitation hardening
7xxx	Al-Mg-Zn	Precipitation hardening
8xxx	Al-Sn	Precipitation hardening

The aluminum alloys are divided according to a numbering system determined by the alloying element, so that observing the first digit of the nomenclature, the main alloy can be identified and the alloy related to the series to which it belongs. For aluminum alloys for forging, the first number indicates the alloying element of greater proportion, the second number indicates whether the alloy is a modification of another and the last two digits are identifiers of the alloy (MANGONON, 1999). For foundry alloys, the first digit indicates the highest proportion alloying element, the next two digits are numerical identifiers of the alloy and the number after the decimal point indicates the shape of the molten product (0 = cast, 1 = ingot). Table B.4 shows the classification and nomenclature of aluminum alloys for forging.

Table B.4: Classification and nomenclature of forging aluminum alloys (MANGONON, 1999).

<table>
<tr><th colspan="3">Nomenclature of aluminum alloys according to the alloying element.</th></tr>
<tr><th colspan="3">4 digits are used xxxx</th></tr>
<tr><th colspan="2">First digit indicates predominant element</th><th>Second digit x''x''xx</th></tr>
<tr><td>1xxx</td><td>Al>99%</td><td rowspan="6">In group 1: indicates control of impurities.
In series 1: zero (0) indicates that there is no control.
The other numbers indicate special control.
In the series 2xxx to 9xxx:
0 indicates original alloy</td></tr>
<tr><td>2xxx</td><td>Cu</td></tr>
<tr><td>3xxx</td><td>Mn</td></tr>
<tr><td>4xxx</td><td>Si</td></tr>
<tr><td>5xxx</td><td>Mg</td></tr>
<tr><td>6xxx</td><td>Mg y Si</td></tr>
<tr><td>7xxx</td><td>Zn</td><td>Third and fourth digit xx''xx''</td></tr>
<tr><td>8xxx</td><td>Otros elementos</td><td>In series 1: indicates the minimum
percentage of aluminum, over 99%.
In groups 2 to 8 it serves only to identify the alloy.</td></tr>
</table>

Sequential, to the nomenclatures of the aluminum alloys, several digits are presented that specify the state of transformation of the material, relating the letters O, H, T, F and W with the type of transformation applied (ASKELAND ET AL., 2013). In Table B.5 shows the commonly used digits and their meaning.

Table B.5: Tempered grades for aluminum alloys (MANGONON, 1999).

Letter	Meaning
F	Material as manufactured
O	Annealing in the softest state possible
H	Worked in cold.
H1x	Cold worked (the x only refers to the amount of work in cold and hardening)
H12	Cold working that provides a resistance to the intermediate tension between O and H14.
H14	Cold working that provides a resistance to the intermediate tension between O and H18.
H16	Cold working that provides a resistance to the intermediate tension between H14 and H18.
H18	Cold work resulting in a reduction of approximately 75%.
H19	Cold working that provides a tensile strength higher than 2000 psi from that obtained by H18.
H2x	Work in cold and partially annealed.
H3x	Work in cold and stabilized at a low temperature, to avoid hardening due to aging of the structure.
W	Treated by solution
T	Precipitation hardening
T1	Cooled from the manufacturing temperature and naturally precipitation hardening
T2	Cooled from the manufacturing temperature, worked cold and naturally precipitation hardening
T3	Treated by solution, worked cold and natural precipitation hardening
T4	Treated by solution and natural precipitation hardening
T5	Cooled from the manufacturing temperature and artificial precipitation hardening.
T6	Treated by solution and artificial precipitation hardening
T7	Treated by solution, stabilized by over-precipitation hardening
T8	Treated by solution, cold work and artificial precipitation hardening
T9	Treated by solution, artificial precipitation hardening and cold work